INTERACTION NOTES

Note 238

THEORETICAL AND EXPERIMENTAL INVESTIGATIONS OF THIN-WIRE STRUCTURES: JUNCTION CONDITIONS, CURRENTS, AND CHARGES

February 1975

Chalmers M. Butler
Bob M. Duff
University of Mississippi
University, Mississippi 38677

Ronold W.P. King
Harvard University
Cambridge, Massachusetts 02138

Edward Yung
Santiago Singarayar
University of Mississippi
University, Mississippi 38677

ABSTRACT

In this report, the electromagnetic boundary conditions applicable at the confluence or junction of two or more thin wires are investigated theoretically, numerically, and experimentally. Current and charge distributions determined from iterative and numerical solutions, as well as from measurements, are provided for fundamental thin-wire structures: stepped-radius wire, bent wire, and V-cross wire. Comparison of theoretical and experimental results are presented.

This study was performed under subcontract to

The Dikewood Corporation
1009 Bradbury Drive, S.E.
University Research Park
Albuquerque, New Mexico 87106

CONTENTS

ILLUSTRATIONS

SECTION I

INTRODUCTION

At present there is an intense interest among many research groups in learning more about charges and currents induced on metallic surfaces of objects by incident electromagnetic waves. One object of major interest is the aircraft. Of course, even the simplest aircraft is an extremely complex body when viewed in the context of a scatterer in an electromagnetic boundary value problem. In an effort to obtain at least a cursory understanding of the behavior of charge and current induced on an aircraft surface, several research workers have replaced the actual aircraft by a wire model configured after the general shape of an aircraft. Then the current on the model is calculated by means of presently available techniques, with the hope that the current and charge on the model bear a global semblance of those on the actual aircraft.

Numerous methods [1-8] for calculating currents and charges induced on thin-wire structures by incident electromagnetic waves have been developed in recent years. These methods are all, of course, based upon Maxwell's equations but they incorporate a variety of approximations to achieve results. Of course, the exact boundary conditions of

electromagnetic theory are well known but, in dealing with complex thin-wire structures, one employs appropriate simplifications to reduce his problem to one which is practically tractable. For a wire ensemble with no intersecting wires (no junctions), the traditional assumptions of thin-wire theory suffice and lead to accurate solutions. But the question of what boundary conditions to impose to account for the confluence of two or more wires remains partially unanswered. The conditions which are imposed by present researchers are not mutually consistent.

Since all junction conditions suggested to date are more or less approximate, the goals that one seeks to achieve by the application of a given junction condition should be delineated. Aside from ease of implementation and incorporation into the solution method, the conditions should at least ensure accurate axial linear charge and current densities on all parts of a given structure which are remote, in terms of numbers of wire radii, from junctions of wires. With this met, possibly the next most important objective is to satisfy the electromagnetic boundary conditions in some sense in the junction region. At the present time it is not known to what extent these two goals can be achieved simultaneously nor is it known whether or not exact conditions can be found.

This report describes a research project which is an initial investigation of the junction conditions. Within thin-wire limitation, the correct approximate boundary

conditions are developed and are subjected to various theoretical and experimental test, but this work should not be looked upon as final. More experimental verification is highly desirous.

The purpose of the study described in this report has been to investigate the thin-wire junction conditions and the distributions of current and charge on wire structures. Included in the report are analytical, numerical, and experimental investigations of the behavior of current and charge on a wire with a discontinuous radius--the so-called stepped-radius problem. Measured currents and charges on wire structures with bends and junctions are given, and an iterative analysis of the bent-wire scatterer is included.

In Section II is described an analytical investigation of the fundamental junction created by the confluence of two coaxial wires of different radii. Based on theoretical considerations of this model, the two correct conditions which must obtain at such a junction are developed. In Section III, a numerical procedure is presented for analysis of the stepped-radius wire both as a scatterer and as an antenna. Experimental results of Section VI serve to support, in a preliminary fashion, both the junction conditions set forth in Section II and the numerical results of Section III.

Section V is devoted to a complete description of the measurement facility and apparatus as well as to pertinent construction details of experimental models. As a vehicle

in which to apply the junction conditions proffered in II, an iterative solution procedure is developed in Section IV for the bent-wire scatterer. With the above-mentioned conditions incorporated in the analysis, the calculated zero-order current distributions on the bent wire are shown to be almost identical in shape with measured currents. Not only does the iterative solution provide a means for lending additional credence to the boundary conditions but, also, of importance as well, it is an analytical technique from which one can determine the correct current distributions on the bent-wire in a direct and simple manner.

Section VII is a thorough report of first measurements of current and charge on a bent wire illuminated by a plane electromagnetic field. Also in this section are found first measurements on a rather complex structure having a junction formed by the joining of four non-perpendicular wires. This latter structure, dubbed the V-cross scatterer by the investigators, is intended to be a crude but useful model of a swept-wing aircraft.

Lastly, to assess the influence of junction geometry on currents and charges remote from the junction, measurements are given for the case of a bent wire with a small sphere at the bend. These data show the effect which a protuberance, e.g., engine pod, tank, on an object might cause. Also, they are somewhat indicative of what factors one must consider in a complete electromagnetic representation of a prescribed junction geometry.

SECTION II

JUNCTION CONDITIONS FOR ELECTRICALLY THIN CONDUCTORS

1. INTRODUCTION

An important step in the determination of the distribution of current at all points on the surfaces of metal radiating structures that include confluent or intersecting wires is the correct specification of the currents and their derivatives at the junctions. Examples of such junctions are (a) the point of confluence of two straight conductors at an arbitrary angle including the straight angle when the conductors have different radii; (b) the junction of a vertical antenna with the radial wires of a top load; (c) the point of intersection of two crossed antennas that make an arbitrary angle; (d) the junctions in a fish-bone-like configuration of conductors; (e) the apex of an umbrella antenna. The antennas that include junctions may be driven elements or parasitic antennas that act as receivers or scatterers. Of particular interest are the parasitic crossed conductors that have been used to simulate an aircraft exposed to a periodic or transient electromagnetic field of high intensity. An accurate knowledge of the surface densities of current and charge on the conductors permits the specification of the tangential magnetic and the normal electric fields. These are needed in the evaluation of the fields that penetrate into the

interior of an aircraft through an imperfectly conducting metal skin or through cracks and apertures.

The conditions imposed in the literature on the currents at the junctions of electrically thin conductors are numerous and varied. There is a general agreement that Kirchhoff's current law on the sum of the inwardly directed currents must be enforced, that is

$$\sum_{k=1}^{n} I_{ink} = 0 \qquad (1)$$

This follows from the fact that for electrically thin conductors (with $ka_i \ll 1$ for all radii a_i of the confluent wires) the chargeable surfaces belonging specifically to the junction--as a region distinct from the wires--are negligibly small since they are of the order of $(ka)^2$. As a consequence, the conservation of electric charge requires the total current into the junction to be zero. But (1) provides only one of the n conditions required if there are n conductors that meet at a junction. The n-1 additional conditions that are needed to specify the n currents are given by Miller et al. [1] and Tesche [2] to be:

$$\frac{I_1'}{a_1} = \frac{I_2'}{a_2} = \frac{I_3'}{a_3} = \cdots\cdots = \frac{I_n'}{a_n} \qquad (2)$$

where the prime denotes differentiation in the direction of the wire and a_i is the radius of wire i. These conditions are justified by their proponents with the statement that the "surface densities of charge must approach the same value as an

observer moves along a wire towards the junction regardless of which wire he is on." Note that the equation of continuity for conductor i is,

$$I_i' = -j\omega q_i = -j\omega 2\pi a_i \eta_1 \tag{3}$$

where q_i is the charge per unit length, η_i the charge per unit surface area. It follows that (2) is equivalent to:

$$\eta_1 = \eta_2 = \eta_3 = ... = \eta_n \tag{4}$$

where η_i is the surface density of charge on conductor i at the junction. Note also that approximate rotational symmetry about each conductor has been assumed. Other writers [3-6] impose no condition on the derivatives of the currents at the junction but state that continuity of scalar potential along the surfaces of all conductors at the junction is to be used instead of (1). This is carried out explicitly in the work of Butler [5], whereas, as pointed out by Logan [7], continuity of scalar potential is "inherent in the integral formulation of Chao and Strait"[6]. King and Wu [8]note that the scalar potential is in any case continuous everywhere except across a double layer as in a delta-function generator. They impose the conditions:

$$I_1' = I_2' = I_3' = ... = I_n' \tag{5}$$

which differ from (2) whenever the a_i's are not all the same. Specifically, (5) is equivalent to:

$$q_1 = q_2 = q_3 = ... = q_n \tag{6}$$

and not (4). In (6) q_i is the charge per unit length on conductor i at the junction. Actual computations by Tesche [2] and King and Wu [8] have been limited to the junction of conductors with equal radii, in which case (5) is equivalent to (2). The conditions (5) have been verified experimentally by Burton and King [9] but only for conductors with equal radii.

In a completely analytical approach such as that of King and Wu [8] a solution cannot be obtained without the explicit application of n conditions at the junction of n conductors, viz., (1) and (5). When numerical techniques such as the method of moments are used, a rigorous treatment of a junction is not possible and various artifices are employed. Some of these enforce Kirchhoff's law (1) explicitly, others do not. In general, the current entering the junction from each conductor is obtained by extrapolation and the extrapolated currents then satisfy (1) more or less accurately. Most of the numerical procedures actually impose no explicit condition on the derivatives of the currents as the junction is approached so that it is not surprising that condition (5) is usually violated. That this is the case is evident from many of the graphs of current distribution given by Logan [7], in which the slopes of both the real and imaginary parts of the currents in the confluent conductors differ greatly at the junction. Since discontinuities in the slopes of the components of current can occur only across a delta-function generator, and since such generators are not assumed to be present, the local distributions of charge per unit length and the associated radial electric fields cannot be correct near the junction.

The explicit application of (1) and n-1 additional conditions at the junction of n electrically thin conductors is required in order to obtain correct solutions for the currents and the associated charges. Evidence will be presented in the following sections to show that conditions (5) or (6) but not (2) or (3) should be applied at the confluence of conductors with unequal radii. Conditions of continuity imposed on the scalar potential or components of the vector potential are obviously redundant and no substitute for (5),

2. CHANGE IN THE RADIUS OF A COAXIAL LINE

The distributions of current and charge per unit length on the inner conductor of a coaxial line resemble those along a dipole or monopole antenna in the sense that both are approximately sinusoidal in their leading terms. This suggests that the local properties of the current and charge per unit length at and near a discontinuity in radius should be comparable at least so long as the cross-sectional dimensions are electrically small. Such a discontinuity is shown in Fig. 1. Specifically, line 1 consists of an inner conductor with radius a_1 and shield with inner radius b in the range of negative values of the coordinate z; line 2 extends from z=0 to positive values of z with an inner conductor with radius $a_2 > a_1$ and the same shield. Thus, there is an annular step in the inner conductor at z=0 from radius a_1 to radius a_2 while the shield continues smoothly.

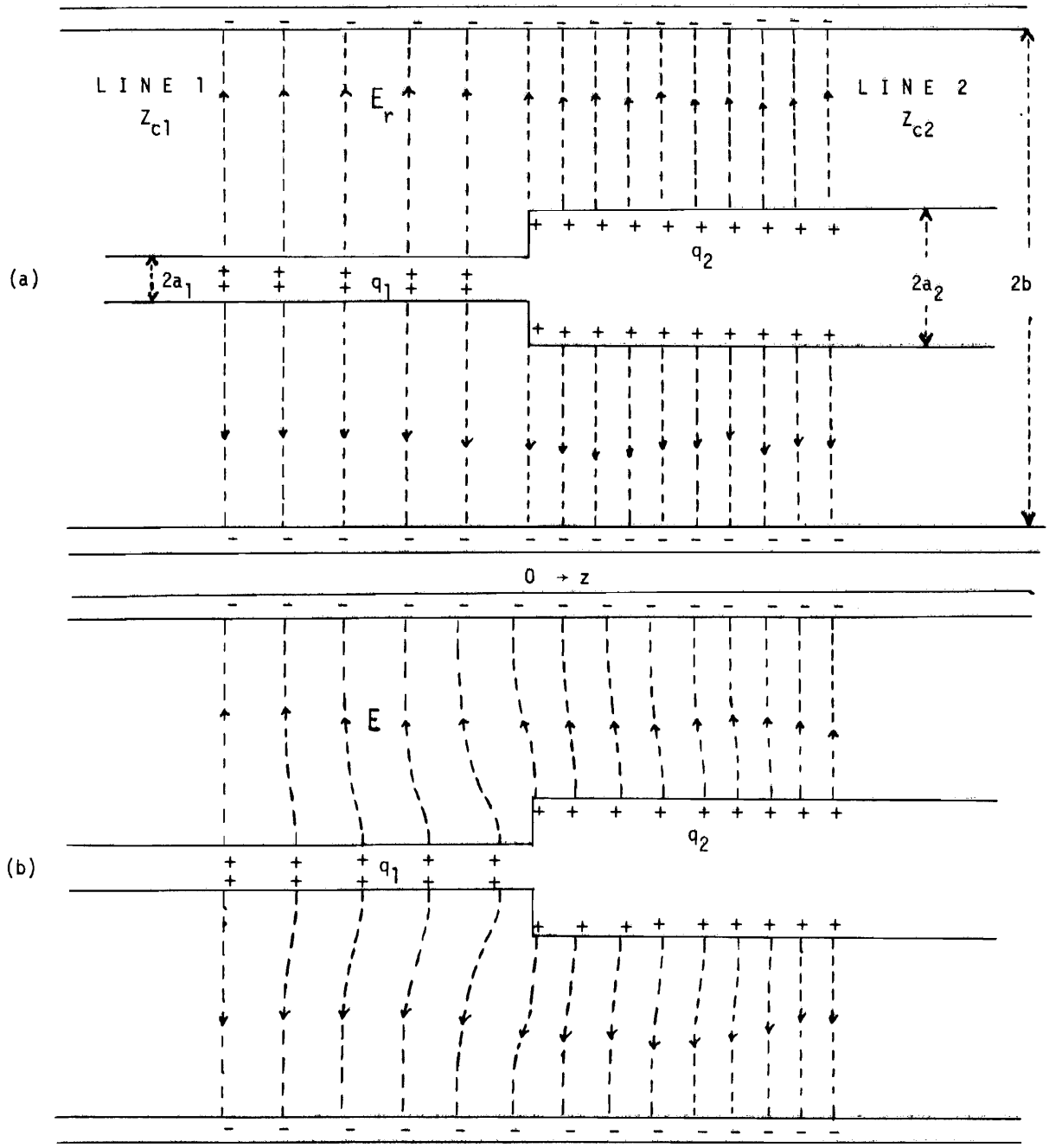

Figure 1. (a) Zero-Order, (b) Approximate Actual Distributions of Charge per Unit Length and Radial Electric Field in a Coaxial Line.

The properties of the line with this change in radius of the inner conductor have been determined by variational methods [10]. Each line is characterized by the conventional parameters and a corrective lumped susceptance B connected across the line at the junction, z=0. The parameters of the line are:

$$c_i = \frac{2\pi\varepsilon_0}{\ell n(b/a_i)} \tag{7a}$$

$$\ell_i = \frac{\mu_0 \ell n(b/a_i)}{2\pi} \tag{7b}$$

$$Z_{ci} = \sqrt{\ell_i/c_i} = (\zeta_0/2\pi)\ \ell n(b/a_i) \tag{7c}$$

$$k_i = \omega\sqrt{\ell_i c_i} = \omega\sqrt{\mu_0\varepsilon_0} = k_0 \tag{7d}$$

where i=1,2. For a line with a_1=0.5 cm, a_2=1.5 cm and b=5.5 cm, $c_1=23.2\times10^{-12}$ farad/m, $c_2=15.2\times10^{-12}$ farad/m, $\ell_1=4.8\times10^{-7}$ henry/m, $\ell_2=2.6\times10^{-7}$ henry/m, Z_{c1}=143.9 ohms, and Z_{c2}=78.0 ohms.

The general formula for the shunt susceptance B is given by Marcuvitz [10]. When $(a_2-a_1)<<(b-a_1)$, which is of interest here, it has the form:

$$B = \frac{2A_1(a_2-a_1)^2}{Z_{c1}\lambda(b-a_1)}\left\{\frac{(b-a_1)}{(b-a_2)}\ \ell n\left(\frac{2(b-a_1)}{a_2-a_1}\right)\right.$$

$$\left. + \frac{1}{2} + \frac{17}{8}\left(\frac{b-a_1}{\lambda}\right)^2 + \frac{A_2}{A_1}\right\} \tag{8a}$$

With $B=\omega C$ and the use of (7a) and (7c), the shunt capacitance C at z=0 is:

$$C = c_1 \frac{A_1(a_2-a_1)^2}{\pi(b-a_1)} \left\{ \frac{(b-a_1)}{(b-a_2)} \ln\left(\frac{2(b-a_1)}{a_2-a_1}\right) + \frac{1}{2} + \frac{17}{8}\left(\frac{b-a_1}{\lambda}\right)^2 + \frac{A_2}{8} \right\} \tag{8b}$$

where c_1 is the capacitance per unit length of line 1. In (8a,b)

$$A_1 = \frac{(b-a_2)^2}{a_2(b-a_1)} \frac{\ln(b/a_1)}{[\ln(b/a_2)]^2} \tag{9}$$

A_2 is defined in general on page 230 of Marcuvitz [10]. For present purposes the range of interest is given by:

$$(b/a_1) > (b/a_2) >> 1 \tag{10}$$

In this range,

$$A_2 << 1; \quad A_1 = \frac{b\ln(b/a_1)}{a_2[\ln(b/a_2)]^2} \tag{11}$$

With these values and the use of (10), (8b) becomes:

$$C = c_1 \frac{a_2}{\pi}\left(1-\frac{a_1}{a_2}\right)^2 \frac{\ln(b/a_1)}{a_2[\ln(b/a_2)]^2} \left\{ \ln(b/a_2) + \ln\left(\frac{2a_2}{a_2-a_1}\right) + \frac{1}{2} + \frac{17}{8}\left(\frac{b}{\lambda}\right)^2 \right\} \tag{12a}$$

When b/a_1 and b/a_2 are sufficiently large, the leading term is:

$$C = c_1 \frac{a_2}{\pi} \left(1 - \frac{a_1}{a_2}\right)^2 \tag{12b}$$

In general this is a very small capacitance that can be neglected in a zero-order approximation. For example, with a_1=0.5 cm and a_2=1.5 cm, C/c_1 as given by (12b) has the value,

$$C/c_1 = 2.1 \times 10^{-3} \text{ m} \tag{12c}$$

where c_1 is the capacitance per meter of line 1.

If a standing wave is maintained on the line with a maximum voltage at z=0,

$$V_1(z) = V_1(0)\cos kz \ , \quad z<0 \tag{13a}$$

$$V_2(z) = V_2(0)\cos kz \ , \quad z>0 \tag{13b}$$

With the condition,

$$V_1(0) = V_2(0) \tag{14}$$

and the basic transmission-line equation,

$$q_i(z) = c_i V_i(z), \quad i = 1,2 \tag{15}$$

the following relations are found to obtain:

$$\frac{q_2(0)}{q_1(0)} = \frac{c_2}{c_1} = \frac{\ell n(b/a_1)}{\ell n(b/a_2)} = \frac{\ell n\ 11}{\ell n\ 3.67} = 1.84 \tag{16}$$

where the numerical values apply to the case of a_1=0.5 cm, a_2=1.5 cm, b=5.5 cm. Thus, in zero-order approximation, the

charge per unit length is discontinuous across the junction. This condition is illustrated schematically in Figs. 1a and 2a where the charges and the associated radial electric fields change their values abruptly at z=0. Actually, of course, the change from $q_1(z)$ to $q_2(z)$ is not discontinuous but occurs over very short distances on each side of the junction with magnitudes of the order of b. In this range the capacitance per unit length is not constant, i.e. $c_1(z) \neq c_1$ and $c_2(z) \neq c_2$. Also, the charges per unit length vary rapidly but continuously from the value $q_1(z) \doteq q_1(0)$ at $z \doteq -5b$ to the value $q_2(z) \doteq q_2(0)$ at $z \doteq 5b$. Since $kb \ll 1$, it is evident that

$$\frac{q_2(5b)}{q_1(-5b)} \doteq \frac{c_2}{c_1} = \frac{\ell n(b/a_1)}{\ell n(b/a_2)} \tag{17}$$

The continuous distributions $q_1(z)$ and $q_2(z)$ and the associated electric fields are shown schematically in Figs. 1b,2b. Note that outside a narrow range on each side of z=0, the distributions of $q_1(z)$ and $q_2(z)$ are the same as in Fig. 1a. Inside this range they differ.

In both Figs. 1a and 1b the small corrective capacitance C has been neglected. If it were included in Fig. 1b, a small additional charge would be located on the flat annular surface at z=0 with a consequent very small shift in the entire standing-wave pattern toward z=0. The actual distributions of current and charge on the inner and outer conductors of the coaxial line are shown schematically in Fig. 2b. Note that q(z) varies continuously along the inner surface of the shield, changing

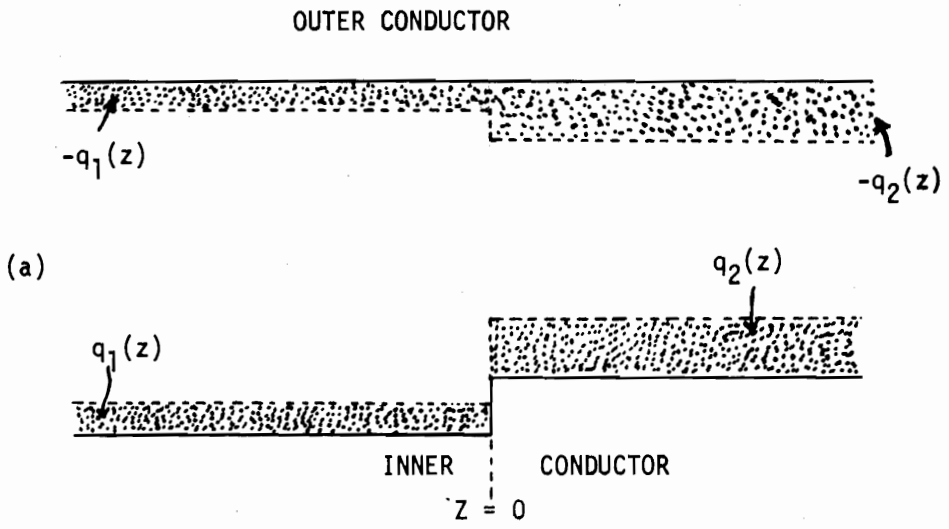

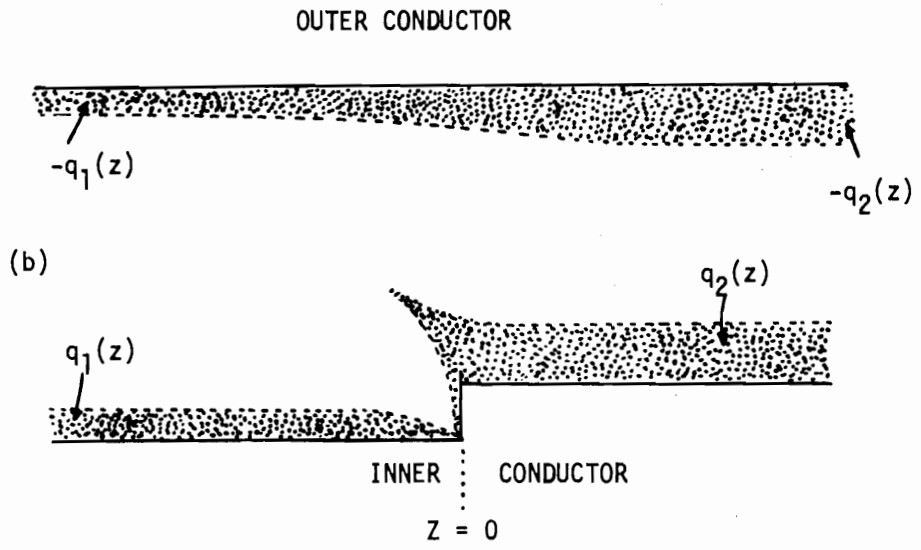

Figure 2. (a) Zero-Order, (b) Approximate Actual Charge per Unit Length on Inner and Outer Conductors of Coaxial Line Near Change in Radius.

from $q_1(z)=c_1V_1(z)$ to $q_2(z)=c_2V_2(z)$ in a very short distance on each side of the junction plane. On the inner conductor $q(z)$ drops to zero at the sharp inside corner, builds up along the annular surface to reach a sharp and high peak at the outside corner, and then tapers off rapidly to reach the value $q_2(z)=c_2V_2(z)$. On the inside surface of the shield the change from $q_1(z)$ to $q_2(z)$ is also rapid but smooth. The magnitude of the total positive charge in the range $-5b \leq z \leq 5b$ on the inner conductor equals that of the negative charge on the outer conductor.

The significant consequence of this investigation is the condition:

$$\frac{q_2(0)}{q_1(0)} = \frac{\ln b - \ln a_1}{\ln b + \ln a_2} \to 1; \quad \ln b \gg \ln a_2 \tag{18}$$

As the outer conductor recedes from the inner one with increasing b, the charges per unit length on each side of the junction become equal. Although this relation has been obtained with a TEM mode, the distributions of current and charge per unit length along an antenna are sufficiently similar to those along the inner conductor of a coaxial line, that it seems reasonable to conclude that

$$q_1(0) = q_2(0) \tag{19}$$

for the antenna with a discontinuous radius. This is, of course, a zero-order representation for electrically thin conductors.

3. CHANGE IN THE CROSS SECTION OF A SPHEROIDAL ANTENNA

Consider a line source of length 2h that extends from z=-h to z=h along which a suitable distribution of generators maintains a sinusoidal current of the form:

$$I(z,t) = I_m \cos\beta z \cos\omega t \tag{20a}$$

when the electrical half lengths are $\beta h = n\pi/2$ with n odd and

$$I(z,t) = I_m \sin\beta z \cos\omega t \tag{20b}$$

when n is even. The associated distributions of charges per unit length are obtained with the equation of continuity

$$\frac{\partial I(z,t)}{\partial z} + \frac{\partial q(z,t)}{\partial t} = 0 \tag{21}$$

They are:

$$q(z,t) = (I_m/c) \sin\beta z \sin\omega t \text{ , n odd} \tag{22a}$$

$$q(z,t) = (I_m/c) \cos\beta z \sin\omega t \text{, n even} \tag{22b}$$

where $c=\omega/\beta=3\times10^8$ m/sec is the velocity of electromagnetic waves in air.

The exact electromagnetic field at all points generated by these distributions of current and charge has the following components in the cylindrical coordinates r,ϕ,z for n odd with the upper sign, n even with the lower sign:

$$B_\phi(t) = -\frac{\mu_0 I_m}{4\pi r}[\sin(\omega t - \beta R_{1h}) \pm \sin(\omega t - \beta R_{2h})] \tag{23a}$$

$$E_r(t) = -\frac{\zeta_0 I_m}{4\pi r}\left[\frac{(z-h)}{R_{1h}}\sin(\omega t - \beta R_{1h}) \pm \frac{(z+h)}{R_{2h}}\sin(\omega t - \beta R_{2h})\right] \tag{23b}$$

$$E_z(t) = \frac{\zeta_0 I_m}{4\pi}\left[\frac{1}{R_{1h}}\sin(\omega t - \beta R_{1h}) \pm \frac{1}{R_{2h}}\sin(\omega t - \beta R_{2h})\right] \tag{23c}$$

In these formulas $\mu_0 = 4\pi \times 10^{-7}$ henry/m, $\zeta_0 = \sqrt{\mu_0/\epsilon_0} = 120\pi$ ohms,

$$R_{1h} = \sqrt{(z-h)^2 + r^2} \quad , \quad R_{2h} = \sqrt{(z+h)^2 + r^2} \tag{24}$$

This field can also be expressed in the spheroidal coordinates k_e, k_h and ϕ with the ends of the line source at $z=\pm h$ as the foci of a family of prolate spheroids with semi-major axes $a_e = hk_e$ and a family of orthogonal hyperboloids of two sheets with semi-conjugate axes $a_h = hk_h$. These are defined as follows in terms of the distances R_{1h} and R_{2h} from any point P to the foci:

$$R_{2h} + R_{1h} = 2a_e \tag{25a}$$

$$R_{2h} - R_{1h} = 2a_h \tag{25b}$$

The spheroidal coordinates

$$k_e = a_e/h = 1/e_e \quad ; \quad k_h = a_h/h = 1/e_h \tag{26}$$

are illustrated in Fig. 3. The eccentricities are e_e for the spheroids, e_h for the hyperboloids. The coordinates k_e and k_h have the following ranges:

$$1 \leq k_e \leq \infty \quad ; \quad -1 \leq k_h \leq 1 \tag{27}$$

The cylindrical radial coordinate r can be expressed in terms of the spheroidal coordinates k_e and k_h as follows:

$$r = h\sqrt{(k_e^2 - 1)(1 - k_h^2)} \tag{28}$$

With (25a,b) - (28), the cylindrical components in (23a-c) can be transformed into the following spheroidal components:

$$B_\phi(k_e,k_h,t) = - \frac{\mu_0 I_m}{2\pi h} \frac{\cos(n\pi k_h/2)}{\sqrt{(k_e^2-1)(1-k_h^2)}} \sin(\omega t - n\pi k_e/2) \tag{29a}$$

$$E_e(k_e,k_h,t) = - \frac{\zeta_0 I_m}{2\pi h} \frac{\cos(n\pi k_h/2)}{\sqrt{(k_e^2-k_h^2)(1-k_h^2)}} \sin(\omega t - n\pi k_e/2) \tag{29b}$$

$$E_\rho(k_e,k_h,t) = \frac{\zeta_0 I_m}{2\pi h} \frac{\sin(n\pi k_h/2)}{\sqrt{(k_e^2-k_h^2)(k_e^2-1)}} \cos(\omega t - n\pi k_e/2) \tag{29c}$$

for n odd. The corresponding expressions for n even are:

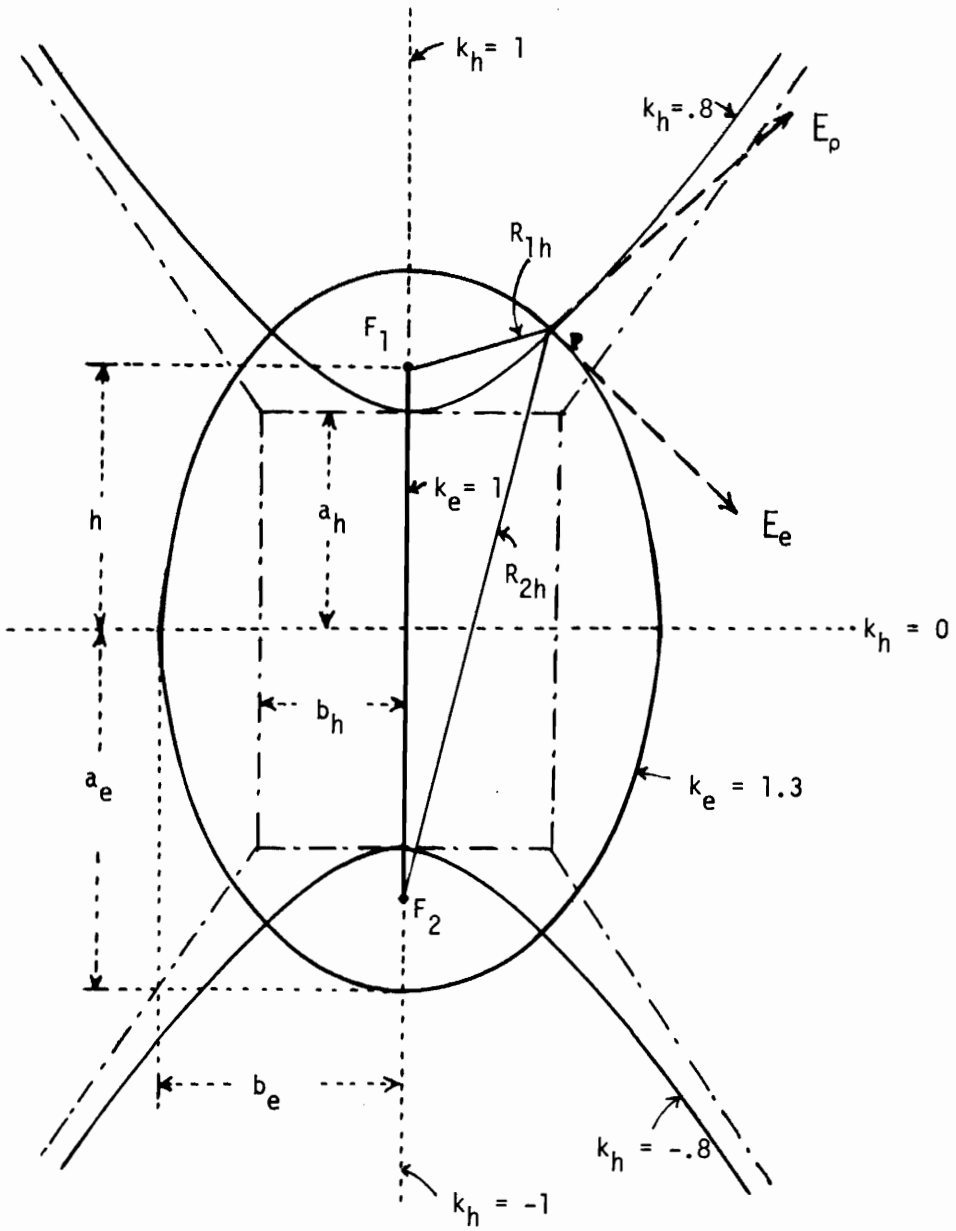

Figure 3. Confocal Coordinates k_e and k_h

$$B_\phi(k_e,k_h,t) = -\frac{\mu_0 I_m}{2\pi h}\frac{\sin(n\pi k_h/2)}{\sqrt{(k_e^2-1)(1-k_h^2)}}\cos(\omega t - n\pi k_e/2) \qquad (30a)$$

$$E_e(k_e,k_h,t) = -\frac{\zeta_0 I_m}{2\pi h}\frac{\sin(n\pi k_h/2)}{\sqrt{(k_e^2-k_h^2)(1-k_h^2)}}\cos(\omega t - n\pi k_e/2) \qquad (30b)$$

$$E_\rho(k_e,k_h,t) = \frac{\zeta_0 I_m}{2\pi h}\frac{\cos(n\pi k_h/2)}{\sqrt{(k_e^2-1)(k_e^2-k_h^2)}}\sin(\omega t - n\pi k_e/2) \qquad (30c)$$

In these formulas $E_e(k_e,k_h,t)$ is the component of the electric field tangent to the spheroid defined by k_e=constant; $E_\rho(k_e,k_h,t)$ is the component of the electric field perpendicular to the spheroid and, hence, tangent to the hyperboloid defined by k_h=constant. Graphs showing the elliptically polarized electric field for n=1,2, and 3 are in Figs. 8.4, 8.5, and 8.6 of Theory of Linear Antennas [11]. A detailed description of the field is on pages 540-546 of [11]. Of importance here are the facts that $B_\phi(k_e,k_h,t)$ and $E_e(k_e,k_h,t)$ are always and everywhere in phase with each other and in phase quadrature with $E_\rho(k_e,k_h,t)$. Each spheroid, k_e=constant, is a surface of constant phase or wave front that expands so that its intersection with the z axis travels with the velocity of light.

Exactly the same field (29a-c) or (30a-c) maintained by a line source, k_e=1, with the current (20a) or (20b) can be maintained by suitable currents on a spheroid $k_e=k_{e1}$

for all values of k_e greater than k_{e1}. The required currents and the associated charges can be obtained by requiring them to satisfy the boundary conditions:

$$\hat{n}\times\vec{B} = -\mu_0\vec{K} \tag{31a}$$

$$\hat{n}\cdot\vec{E} = -\eta/\varepsilon_0 \tag{31b}$$

where $\vec{K}$ and η are the surface densities of current and charge, respectively, on the surface of the highly conducting spheroid defined by $k_e=k_{e1}$, $\hat{n}$ is the externally directed normal to the spheroidal surface, and $\vec{B}$ and $\vec{E}$ are the fields with components given in (29a-c) or (30a-c). Specifically,

$$I_e(k_{e1},k_h,t) = 2\pi r_1 K_e(k_{e1},k_h,t) = 2\pi r_1 B_\phi(k_{e1},k_h,t)/\mu_0 \tag{32}$$

$$q_e(k_{e1},k_h,t) = 2\pi r_1 \eta_e(k_{e1},k_h,t) = 2\pi r_1 E_\rho(k_{e1},k_h,t)\varepsilon_0 \tag{33}$$

where

$$r_1 = h\sqrt{(k_{e1}^2-1)(1-k_h^2)} \tag{34}$$

is the radial distance from the axis to the surface of the spheroid $k_e=k_{e1}$ at each value of k_h. When (29a,c) and (30a,c) are substituted into (32) and (33), the required currents on the spheroidal surface are:

$$\text{n odd:}\quad I_e(k_{e1},k_h,t) = -I_m\cos(n\pi k_h/2)\sin(\omega t - n\pi k_{e1}/2) \tag{35a}$$

n even: $I_e(k_{e1},k_h,t) = -I_m \sin(n\pi k_h/2)\cos(\omega t - n\pi k_{e1}/2)$ (35b)

The associated charges per unit length along the spheroidal surface are:

n odd:

$$q_e(k_{e1},k_h,t) = \frac{I_m}{c}\sqrt{\frac{1-k_h^2}{k_{e1}^2-k_h^2}}\sin(n\pi k_h/2)\cos(\omega t - n\pi k_{e1}/2) \quad (36a)$$

n even:

$$q_e(k_{e1},k_h,t) = \frac{I_m}{c}\sqrt{\frac{1-k_h^2}{k_{e1}^2-k_h^2}}\cos(n\pi k_n/2)\sin(\omega t - n\pi k_{e1}/2) \quad (36b)$$

A spheroidal antenna is electrically thin when its semi-minor axis $b_e = h\sqrt{k_e^2-1}$ satisfies the same condition as the radius of a cylindrical antenna. That is, corresponding to the condition $\beta a << 1$ for the cylindrical antenna the spheroidal antenna must obey the following condition:

$$\beta b_e = \beta h\sqrt{k_e^2-1} = (n\pi/2)\sqrt{k_e^2-1} << 1 \quad (37a)$$

This is equivalent to:

$$\sqrt{k_e^2 - 1} \leq 0.1/n$$

or

$$k_e^2 \leq 1 + 0.01/n \; ; \; k_e \leq 1 + 0.005/n \quad (37b)$$

It is evident that for electrically thin spheroids the quantity k_{e1}^2 differs very little from 1 so that the factor in (36a,b)

$$\sqrt{\frac{1 - k_h^2}{k_{e1}^2 - k_h^2}} = 1 - \varepsilon(k_h) \tag{38}$$

is also near 1. The quantity $\varepsilon(h_k)$ is shown graphically in Fig. 4. It is seen to be very small except near the ends of the spheroid where $k_h = \pm 1$. The trigonometric functions $\sin(n\pi k_h/2)$ and $\cos(n\pi k_h/2)$ are not able to take full account of the distributions of charge as the ends of the antenna are approached. The quantity $\sqrt{(1-k_h^2)/(k_e^2-k_h^2)} = 1-\varepsilon(k_h)$ is a weighting factor that increases with decreasing radius of curvature of the spheroid. In combination with the trigonometric factors it provides an accurate representation of the charge density on the spheroidal antenna including the high concentrations at the ends.

The currents and charges per unit length on a confocal spheroid with surface defined by $k_e = k_{e2} > k_{e1}$ are given by (35a,b) and (36a,b) with k_{e1} replaced by k_{e2}. For all values of $k_e > k_{e2}$ the fields of the two spheroids with different k_e's are identical.

The amplitudes of the currents and charges on the two spheroidal antennas with different k_e's are:

$$I_e(k_{e1},k_h) = -I_m \begin{matrix}\cos \\ \sin\end{matrix}(n\pi k_h/2) \tag{39a}$$

$$I_e(k_{e2},k_h) = -I_m \begin{matrix}\cos \\ \sin\end{matrix}(n\pi k_h/2) \tag{39b}$$

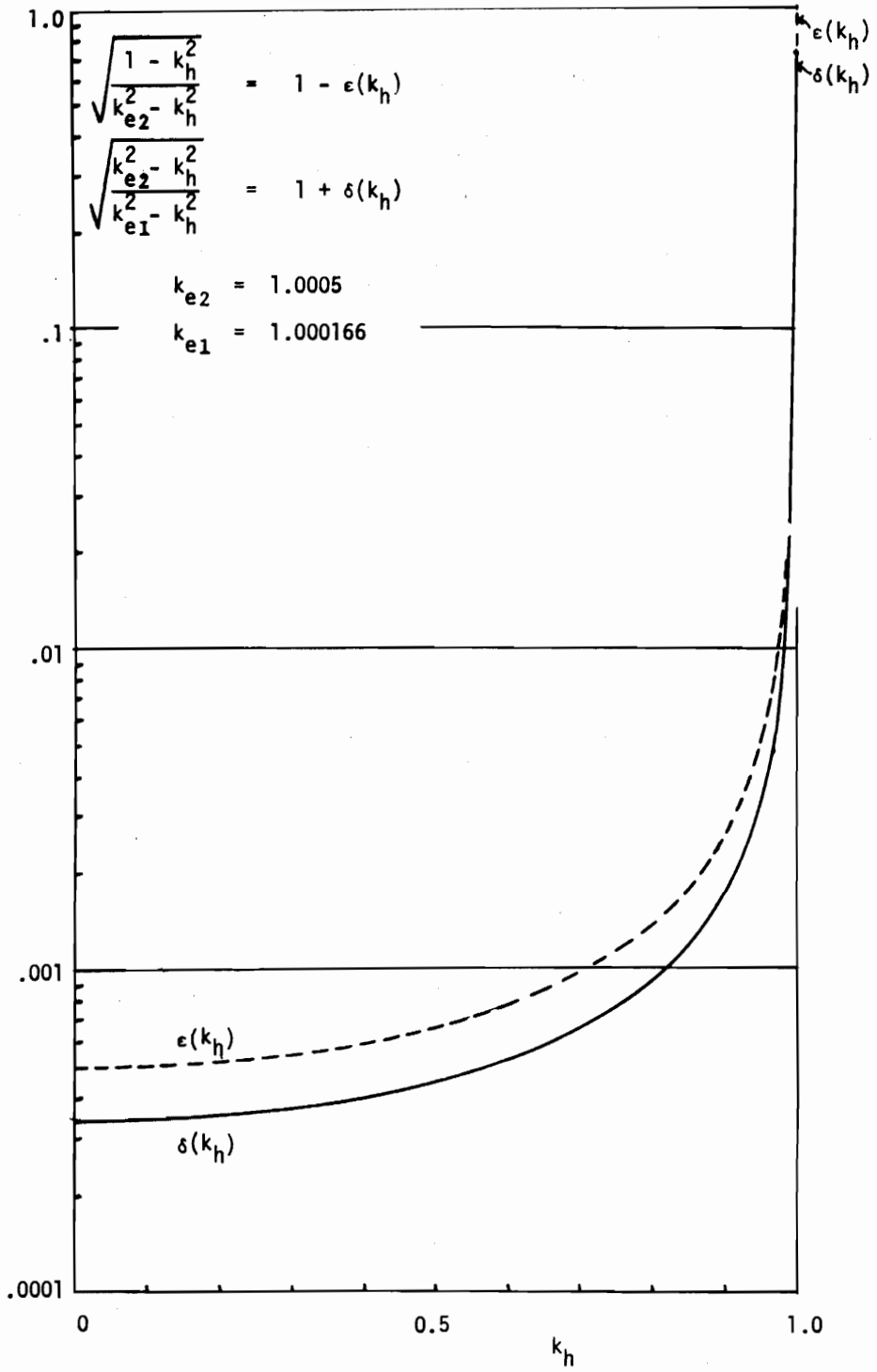

Figure 4. The Functions $\varepsilon(k_h)$ and $\delta(k_h)$

$$q_e(k_{e1},k_h) = \frac{I_m}{c}\sqrt{\frac{1 - k_h^2}{k_{e1}^2 - k_h^2}} \begin{matrix}\sin\\ \cos\end{matrix}(n\pi k_h/2) \qquad (40a)$$

$$q_e(k_{e2},k_h) = \frac{I_m}{c}\sqrt{\frac{1 - k_h^2}{k_{e2}^2 - k_h^2}} \begin{matrix}\sin\\ \cos\end{matrix}(n\pi k_h/2) \qquad (40b)$$

where the upper trigonometric function is for n odd, the lower for n even. At corresponding values of k_h on the two spheroidal antennas the ratio of the current amplitudes is

$$\frac{I_e(k_{e1},k_h)}{I_e(k_{e2},k_h)} = 1 \qquad (41)$$

On the other hand, the corresponding ratio of the charges per unit surface length is

$$\frac{q_e(k_{e1},k_h)}{q_e(k_{e2},k_h)} = \sqrt{\frac{k_{e2}^2 - k_h^2}{k_{e1}^2 - k_h^2}} = 1 + \delta(k_h) \qquad (42)$$

The function $\delta(k_h)$ is also shown in Fig. 4. It is very small except near the ends where it rises rapidly as k_h approaches ± 1. This is a consequence of the fact that the charge per unit surface length increases most quickly where the radius of curvature of the thinner spheroid decreases most rapidly. It follows that the ratio of charges per unit surface length on the thinner to the charges on the thicker antenna rises steeply near the ends. At the center of the antennas (k_h=0) the ratio of the charges per unit surface length is

$$\frac{q_e(k_{e1},0)}{q_e(k_{e2},0)} = \frac{k_{e2}}{k_{e1}} = \frac{a_{e2}}{a_{e1}} = 1.00033 \qquad (43)$$

where the numerical value applies to spheroids with $k_{e1}=1.000166$, $k_{e2}=1.0005$. At the ends ($k_h=\pm 1$),

$$\frac{q_e(k_{e1},\pm 1)}{q_e(k_{e2},\pm 1)} = \sqrt{\frac{1 - k_{e2}^2}{1 - k_{e1}^2}} = \frac{b_{e2}}{b_{e1}} = 1.732 \qquad (44)$$

which is significantly greater than one. The rapidity of the rise near the end can be seen from the fact that at $k_h=0.995$,

$$\frac{q_e(k_{e1},0.995)}{q_e(k_{e2},0.995)} = \sqrt{\frac{k_{e2}^2 - 0.990025}{k_{e1}^2 - 0.990025}} = 1.065 \qquad (45)$$

Evidently most of the increase occurs within 0.005 of the ends.

In order to study the behavior of the charge near a discontinuity in radius, it is convenient to select the spheroid with n=2, i.e., $\beta h=\pi$, for which the maximum of charge occurs at the center, $k_h=0$. The currents and charges are given by (39a,b) and (40a,b) with n=2 for two spheroids with different k_e's. The complete electromagnetic field is given by (30a-c) with n=2; it is shown graphically in Fig. 8.5 of [11]. The fields of the two antennas are identical when $k_e > k_{e2}$. The local amplitude of $E_\rho(k_e,k_h)$ near $k_h=0$ is shown in Fig. 5a where the upper half of the diagram applies to the thinner antenna with $k_e=k_{e1}$, the lower half to the thicker antenna

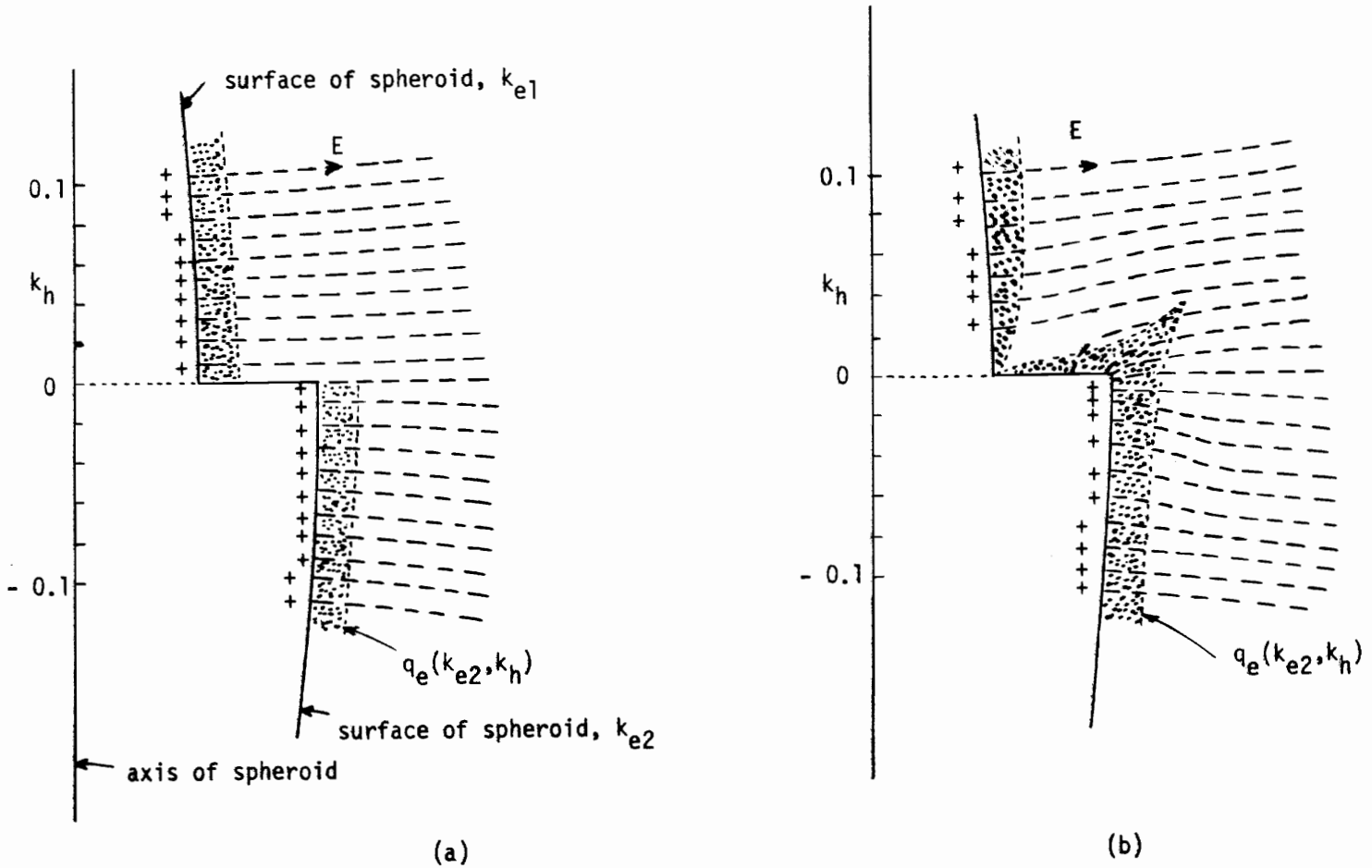

Figure 5. Charges and Electric Fields Near Junction of Spheroidal Antennas at $k_h = 0$ where $E_e = 0$, E_ρ is Maximum.

with $k_e=k_{e2}$. Note that $E_e(k_e,k_h)=0$ at $k_h=0$ and is very small near $k_h=0$. For clarity the values of k_{e1} and k_{e2} actually used in the diagram are much greater than permitted by the condition for electrical thinness. The electric field lines and the charges from which they emanate are shown schematically. The charge per unit surface length, $q_e(k_e,k_h)$, is also shown along each surface.

Although Fig. 5a was drawn to illustrate the electric field and the charges near the point of maximum for one spheroid with surface defined by k_{e1} in the upper half of the diagram, and for a second spheroid with surface defined by k_{e2} in the lower half, the representation is actually a zero-order approximation of the fields and charges of a single spheroidal antenna with surfaces defined by different values of k_e in the upper and lower half spaces and a step at the junction where $k_h=0$. The diagram in Fig. 5a for the spheroidal antenna with discontinuous cross section at its center corresponds to Fig. 1a for the coaxial line with a change in radius of the inner conductor at $z=0$. At short distances from the junction the electric fields are unaffected and have the form and magnitude characteristics of an unperturbed conductor. Near the junction the charges rearrange themselves near the step in the sense that their magnitudes are reduced at the inside corner, increased at the outside corner with appropriate gradual changes along the adjacent surfaces. These are indicated schematically for the spheroid in Fig. 5b in a manner that is analogous to that used for the coaxial

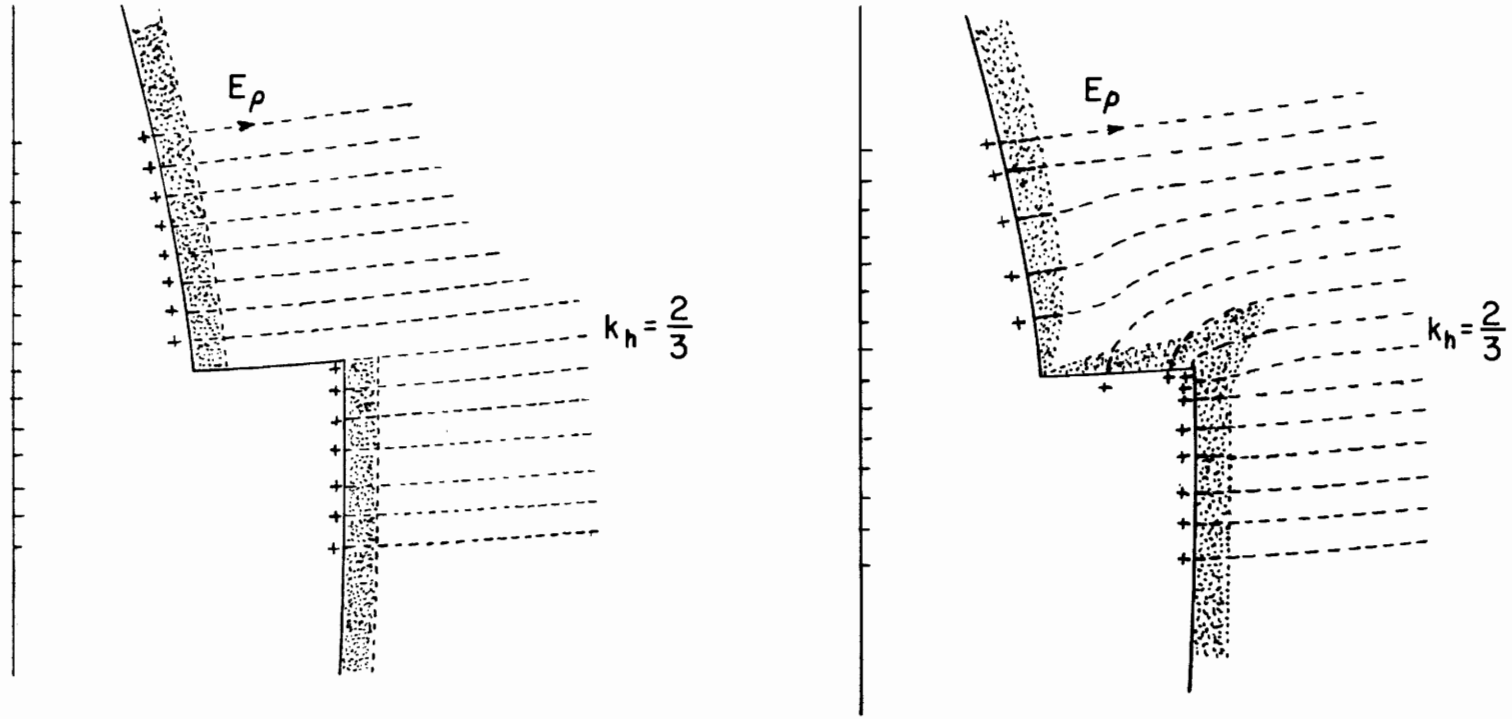

Figure 6. Charges and Electric Fields Near Junction of Spheroidal Antennas at $k_h = \frac{2}{3}$ where $E_e = 0$, E_ρ is Maximum.

line in Fig. 2b. Note that at short distances from the junction the fields in Figs. 5a and 5b are the same, just as are those in Figs. 1a and 1b. The magnitude of the charge per unit surface length is shown along the surfaces in Figs. 5a and 5b in a manner similar to that in Figs. 2a and 2b.

The important observation to be drawn from a study of Figs. 5a and 5b is that the ratio of the zero-order charges per unit surface length on the two sides of the junction between electrically thin half spheroids with different eccentricities is very nearly unity. This confirms the conclusions drawn in conjunction with (19) for a similar junction in a coaxial line.

4. REFINEMENT OF THE THEORY

The discussion of the junction in the coaxial line and the spheroid is highly simplified and somewhat unrealistic. In the coaxial line the conclusions depend on allowing the radius of the outer conductor to approach infinity while preserving the purely TEM character of the field. This implies that the cross section of the line remains electrically small, so that the limit is valid only at zero frequency. Clearly, while b should become large compared with a_1 and a_2, it should not exceed a wavelength. If it is noted that (18) is equivalent to:

$$\frac{q_2(0)}{q_1(0)} = \frac{Z_{c1}}{Z_{c2}} \tag{46}$$

and if it is recalled that in coaxial line theory the characteristic impedance Z_c plays the same role as the expansion parameter $\Psi=2[\ell n(2/\beta a)-0.5772]$ in antenna theory, the indication is that b should approach the large value $b=2/\beta$ instead of infinity. In this case (46) becomes:

$$\frac{q_2(0)}{q_1(0)} = \frac{\Psi_1}{\Psi_2} = \frac{\ell n(2/\beta a_1)}{\ell n(2/\beta a_2)} \tag{47}$$

If the radii of the coaxial lines at the junction are made equal to the semi-minor axes of the spheroids used in (43), i.e., $\beta a_2=\beta b_{e2}=0.099$, $\beta a_1=\beta b_{e1}=0.057$, (47) gives:

$$\frac{q_2(0)}{q_1(0)} = 1.18; \quad \frac{q_1(0)}{q_2(0)} = 0.85 \tag{48}$$

These are more realistic values than exactly one.

Throughout the discussion of the spheroidal antenna it has been assumed that a suitable excitation exists along the antenna to maintain currents of the form (39a,b) with the associated charges (40a,b). Actually, if two antennas with different semi-major axes $a_{e1}=hk_{e1}$ and $a_{e2}=hk_{e2}$ but the same distances between foci, viz., 2h, are excited by identically distributed fields of equal amplitude along their respective axes, the amplitudes of the currents will not be the same. Specifically, as shown by Ryder [12],

$$I_n(k_{e1},k_h) \sim[\beta h^2 k_{e1} Y_n(k_{e1})/Y_n'(k_{e1})]\ X_n(k_h) \tag{49}$$

for an excitation of the form

$$E_n(k_h) = \frac{X_n(k_h)}{1 - k_h^2} \tag{50}$$

In these formulas $X_n(k_h)$ is the distribution of current along the antenna and $Y_n(k_{e1})$ and its derivative $Y_n'(k_{e1})$ are functions of $X_n(k_h)$. $Y_n'(k_{e1})$ has the form

$$Y_n'(k_{e1}) = d \ \ell n \frac{k_{e1} + 1}{k_{e1} - 1} + c \tag{51}$$

In (51), d and c are comparable in magnitude in general whereas the logarithm is quite large when k_{e1} is near one. However, d is a function of frequency and goes to zero at the resonances defined by $\beta h = n\pi/2$ while c remains finite. At resonance, $Y_n(k_{e1}) = \exp(in\pi k_e/2)$, $X_n(k_h) = \pm\cos(n\pi k_h/2)$ when n is odd, $X_n(k_h) = \pm\sin(n\pi k_h/2)$ when n is even. It follows that at resonance and when exposed to identical fields of the form in (50) along their respective axes, the amplitudes I_m in (39a,b) and (40a,b) for the antennas must be replaced by $I_m(k_{e1})$ such that with I_{m0} a constant,

$$I_m(k_{e1}) = k_{e1} I_{m0} \ ; \ I_m(k_{e2}) = k_{e2} I_{m0} \tag{52}$$

It follows further that (41) and (42) must be replaced by:

$$\frac{I_e(k_{e1}, k_h)}{I_e(k_{e2}, k_h)} = \frac{k_{e1}}{k_{e2}} \tag{53}$$

$$\frac{q_e(k_{e1},k_h)}{q_e(k_{e2},k_h)} = \frac{k_{e1}}{k_{e2}} \sqrt{\frac{k_{e2}^2 - k_h^2}{k_{e1}^2 - k_h^2}} \tag{54}$$

In particular, the spheroid with n=2, $\beta h=\pi$, that is discontinuous at $k_h=0$ as shown in Fig. 5, will have zero-order currents given by

$$I_e(k_{e1},k_h) = -I_0 k_{e1} \sin\pi k_h \tag{55a}$$

$$I_e(k_{e2},k_h) = -I_0 k_{e2} \sin\pi k_n \tag{55b}$$

which vanish at the junction, $k_h=0$. The corresponding charges per unit length are:

$$q_e(k_{e1},k_h) = \frac{I_0}{c} k_{e1} \sqrt{\frac{1 - k_h^2}{k_{e1}^2 - k_h^2}} \cos\pi k_h \tag{56a}$$

$$q_e(k_{e2},k_h) = \frac{I_0}{c} k_{e2} \sqrt{\frac{1 - k_h^2}{k_{e2}^2 - k_h^2}} \cos\pi k_h \tag{56b}$$

where c is the velocity of light. At the junction, $k_h=0$ and

$$I_e(k_{e1},0) = I_e(k_{e2},0) = 0 \; ; \; q_e(k_{e1},0) = q_e(k_{e2},0) = I_0/c \tag{57}$$

Thus, in the resonant antenna with the junction at a charge maximum and current zero, with each half identically excited

in only the single resonant mode, the charges per unit length at the junction are equal.

With the same excitation but not at resonance the logarithmic term in (51) dominates so that (52) must be replaced by:

$$I_m(k_{e1}) = k_{e1} I / \ell n[k_{e1} + 1)/(k_{e1} - 1)] \tag{58a}$$

$$I_m(k_{e2}) = k_{e2} I / \ell n[(k_{e2} + 1)/(k_{e2} - 1)] \tag{58b}$$

where I is a constant and $\ell n[k_e+1)/(k_e-1)]$ corresponds to the expansion parameter Ψ of a cylindrical antenna. It follows that

$$\frac{I_e(k_{e1},k_h)}{I_e(k_{e2},k_h)} = \frac{k_{e1}}{k_{e2}} \frac{\ell n[(k_{e2}+ 1)/(k_{e2} - 1)]}{\ell n[(k_{e1}+ 1)/(k_{e1} - 1)]} \tag{59}$$

and

$$\frac{q_e(k_{e1},k_h)}{q_e(k_{e2},k_h)} = \frac{k_{e1}}{k_{e2}} \sqrt{\frac{k_{e2}^2 - k_h^2}{k_{e1}^2 - k_h^2}} \frac{\ell n[(k_{e2} + 1)/(k_{e2} - 1)]}{\ell n[(k_{e1} + 1)/(k_{e1} - 1)]} \tag{60}$$

In particular, at the junction,

$$\frac{q_e(k_{e1},0)}{q_e(k_{e2},0)} = \frac{\ell n[(k_{e2} + 1)/(k_{e2} - 1)]}{\ell n[(k_{e1} + 1)/(k_{e1} - 1)]} \tag{61}$$

With k_{e2}=1.0005, k_{e1}=1.000166, (61) gives:

$$\frac{q_e(k_{e1},0)}{q_e(k_{e2},0)} = 0.88 \qquad (62)$$

Note that this value is in good agreement with (48) for an approximately equivalent cylindrical conductor.

When the spheroidal antenna is not excited by the very specially distributed field (50) which excites only the n^{th} mode, but is immersed in an incident plane wave, the total induced current is the sum of the modes,

$$I_t(k_h) = \Sigma a_n I_n(k_h) \qquad (63)$$

where the a_n are amplitude coefficients. Even when the frequency is tuned to resonance with one of the modes, many higher modes will also be present but with much smaller amplitudes. It is to be expected, therefore, that the ideal conditions leading to (53) will not obtain and that (58a,b) will be good approximations. This means that the condition (61) on the charges per unit length at a junction should be generally useful.

5. CONCLUSION

A careful study of the properties of currents and charges in a coaxial line with a step in its inner conductor and of a spheroidal antenna with a similar step leads to the conclusion that the behavior of the charges per unit length near the junction of two cylindrical conductors with different radii

is not simple even for electrically thin conductors. However, a good approximation is given by the condition

$$q_1\Psi_1 = q_2\Psi_2 = \cdots\cdots = q_n\Psi_n \tag{64}$$

where Ψ_i is the expansion parameter for conductor i treated as an antenna. The definition of the expansion parameter is somewhat arbitrary, but is always a logarithmic function. Useful values for conductors that have lengths h that satisfy $\beta h \geq \pi/2$ are given by:

$$\Psi = 2[\ell n(2/\beta a) - 0.5772] \tag{65}$$

For shorter antennas the appropriate parameter is

$$\Psi = 2\ \ell n(2h/a) \tag{66}$$

where a is the radius of the conductor. The conditions (64) and the Kirchhoff condition (1) apply to junctions of electrically thin conductors. There is no justification for a condition of the form (2) or (4). The conditions (5) or (6) may be adequate approximations of (64) for junctions of conductors that are sufficiently thin and not too different in cross-sectional size.

Since in thin-wire theory the surface area of a junction is negligible, and each conductor is treated as if its charges were concentrated at an average position on the axis, the angle at which two conductors meet is irrelevant. This is true provided the diagonal distance across a junction is electrically small, and not only the diameter of the thicker

wire. With this sharpening of the condition for electrical smallness of the junction, the conditions (1) and (64) may be applied in general.

SECTION III

ANALYSIS OF STEPPED-RADIUS WIRE

1. INTRODUCTION

In this section is presented an analysis of the stepped-radius wire structure shown in Fig. 7. This structure, with its confluence of two coaxial wires of different radii, is perhaps representative of the simplest thin-wire configuration possessing a junction. For this reason, the behavior of the stepped-radius wire must be understood before more complicated junction problems are undertaken. A numerical procedure is developed for solving for the current on the stepped-radius wire. The procedure is applied to both a stepped-radius scatterer and an antenna, and representative results are provided.

In the present investigation of the stepped-radius structure of Fig. 7 , the wire radii, a and b, are looked upon as being very small relative to the wavelength λ as well as to the wire length L. These restrictions, common in thin-wire theory, assure one that the current on each cylindrical surface is circumferentially independent and that it may be accounted for by the total axial current, denoted I_a on the cylinder of radius a and I_b on that of radius b. These quantities are shown in Fig. 7 , which serves to define

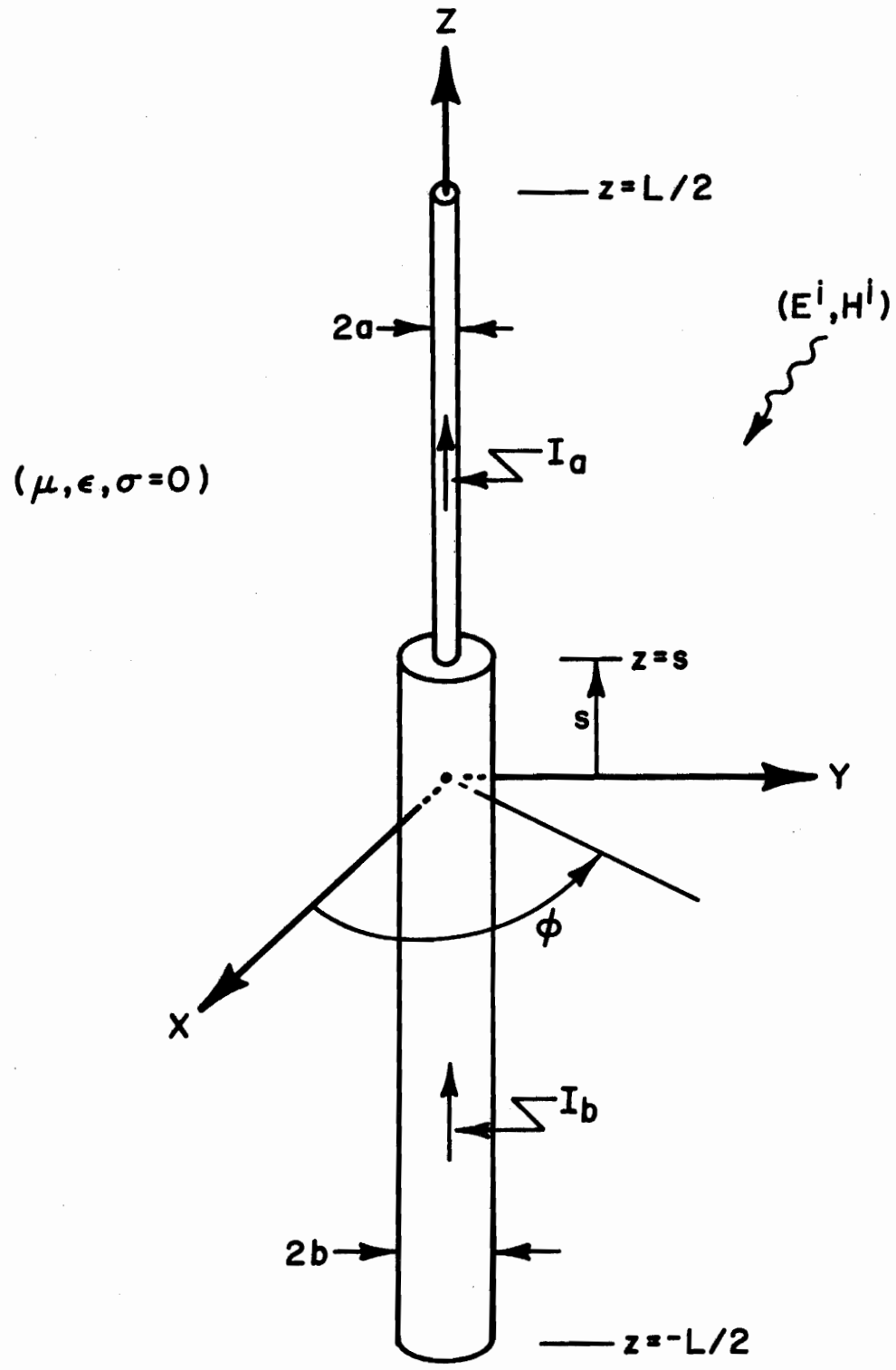

Figure 7. Stepped-Radius Wire

geometric quantities of interest.

In the analysis which follows, the boundary condition that total tangential electric field be zero on the conducting surface is enforced on cylindrical surfaces but not on the small annular surface located where the wire radius is discontinuous at z=s. This annulus is a very small portion of the total surface area of the stepped-radius wire structure and, therefore, when the wires satisfy thin-wire conditions, the accuracy of a solution for current should not suffer seriously from a failure to enforce the boundary condition on the annulus. Experience with thin-wire analyses supports this simplification, since excellent solution accuracy is obtainable for problems involving solid wires even though the boundary condition mentioned above is seldom enforced on the disks at the wire ends.

A further simplification employed here is that one assumes he may ignore the small fraction of total field due to the induced charge and current which reside on the annulus. The chargeable annular surface is, indeed, small compared with the cylinder surfaces, and only a relatively small fraction of the total charge on the structure could reside on the annulus. Ignoring the charge on the annulus or, equivalently, approximating its small value by zero, is tantamount to requiring the total axial current to be continuous at the point z=s (junction) where the two wires of different radii join. If the axial current were discontinuous at the step, charge would be deposited on the annulus in order that the

continuity equation be honored. Therefore, under the assumptions set forth, one considers only the induced charge and current on the cylindrical surfaces and enforces the boundary condition $\bar{E}_{tan}=0$ only on these two surfaces.

In a scattering problem, one requires the sum of the prescribed incident electric field $\bar{E}^i$ and the scattered electric field $\bar{E}^s$, due to induced sources, to have zero tangential component evaluated on the perfectly conducting cylindrical surfaces of the structure: $(\bar{E}^s+\bar{E}^i)\cdot\hat{u}_z=0$ on the surfaces. In an antenna problem, one may view the tangential incident field as being localized at the emf generator and, again, he requires this specified field and the tangential scattered field to add to zero on the structure: $\bar{E}^s\cdot\hat{u}_z+V\delta(z-z_g)=0$ on the surfaces, where $V\delta(z-z_g)$ is a delta function of strength V at $z=z_g$ due to a slice generator of V volts located at z_g. Due to the thin-wire assumption and the rotational symmetry in both the scattering and antenna problems, the scattered electric field $\bar{E}^s$ is independent of ϕ and has no component in the ϕ direction. Hence, to satisfy the boundary condition that the total tangential field be zero on the two cylindrical surfaces, one needs only to calculate $E_z^s(r,z)$, the axially directed scattered field, and to require $E_z^s+E_z^i=0$ on the surfaces.

From basic electromagnetic theory applied to the structure of Fig. 7, one may readily calculate $E_z^s(r,z)$ from

$$E_z^s = -j\omega A_z - \frac{\partial}{\partial z}\Phi \qquad (67)$$

where $A_z(r,z)$ is the z-component of the magnetic vector potential and $\Phi(r,z)$ is the electric scalar potential, both of which are readily determined from the induced current and charge on the structure. The harmonic time variation of angular frequency ω is suppressed in (67). In view of the assumptions and simplifications discussed above, A_z and Φ are calculated from the current and charge, respectively, which reside wholly on the cylindrical surfaces; the contributions to Φ from charge induced on other surfaces are ignored. The boundary condition discussed above now can be written

$$E_z^s(a,z) + E_z^i(a,z) = 0 \quad , \quad z\varepsilon(s,L/2) \tag{68a}$$

and

$$E_z^s(b,z) + E_z^i(b,z) = 0 \quad , \quad z\varepsilon(-L/2,s) \tag{68b}$$

for the scattering problem and

$$E_z^s(a,z) + V\delta(z-z_g) = 0 \quad z\varepsilon(s,L/2) \tag{69a}$$

and

$$E_z^s(b,z) + V\delta(z-z_g) = 0 \quad z\varepsilon(-L/2,s) \tag{69b}$$

for the antenna problem.

2. NUMERICAL SOLUTION PROCEDURE

From Eqs. (67) and (68) or (69), with A_z and Φ written as functions of current, one may readily obtain an integro-differential equation characterizing the current on the stepped-radius structure. Then, of course, this integro-differential equation may be solved for the unknown current. The solution procedure employed here is essentially the moment method [13] but with a change in the usual sequence of steps of this method which enables one to gain interesting insight into the nature of the numerical procedure. The alteration alluded to is that one performs the testing [13] of the equation to be solved before the unknown current is approximated as a linear combination of the basis set. The testing procedure leads to a system of linear equations which represents a discretized equivalent of the original integro-differential equation. The numerical solution procedure is described below, in general, for a representative segment of wire beginning at z_1 and extending to z_M, and, subsequently, the method is applied to the stepped-radius structure.

a. Testing

Pursuant to the establishment of a linear system of equations from which one may ultimately obtain a solution to Eq. (67), one equates the corresponding projections of the two sides of Eq. (67) onto the space spanned by the testing set. In other words, if T_m is an element of the testing set, one equates the scalar product of T_m and the left-hand side

of (67) to that of T_m and the right-hand side:

$$\left\langle -j\omega A_z - \frac{\partial}{\partial z}\Phi,\ T_m \right\rangle = \left\langle E_z^s,\ T_m \right\rangle \quad , \tag{70}$$

$$m = 1,2,\ldots,M$$

where the scalar product is defined

$$\left\langle f,\ g \right\rangle = \int_{z=-L/2}^{L/2} f g^* dz \tag{71}$$

Because they are particularly amenable to numerical solutions of (67) and lead to stable linear systems, the set of piecewise linear functions is selected for testing; the m^{th} element $\Lambda_m^{\ell}(z)$ of this testing set is defined

$$\Lambda_m^{\ell}(z) = \begin{cases} \frac{1}{\Delta}\ (\Delta - |z-z_m|)\ , & z\varepsilon(z_{m-1}, z_{m+1}) \\ \\ 0 \qquad\qquad , & z\notin(z_{m-1}, z_{m+1}) \end{cases} \tag{72}$$

where

$$\Delta = (z_m - z_{m-1}) \tag{73}$$

Implicit in the above, and depicted in Fig. 8 , is the partitioning of the segment of wire of length $z_M - z_1$ into M-1 subintervals, each of length $\Delta = (z_M - z_1)/(M-1)$.

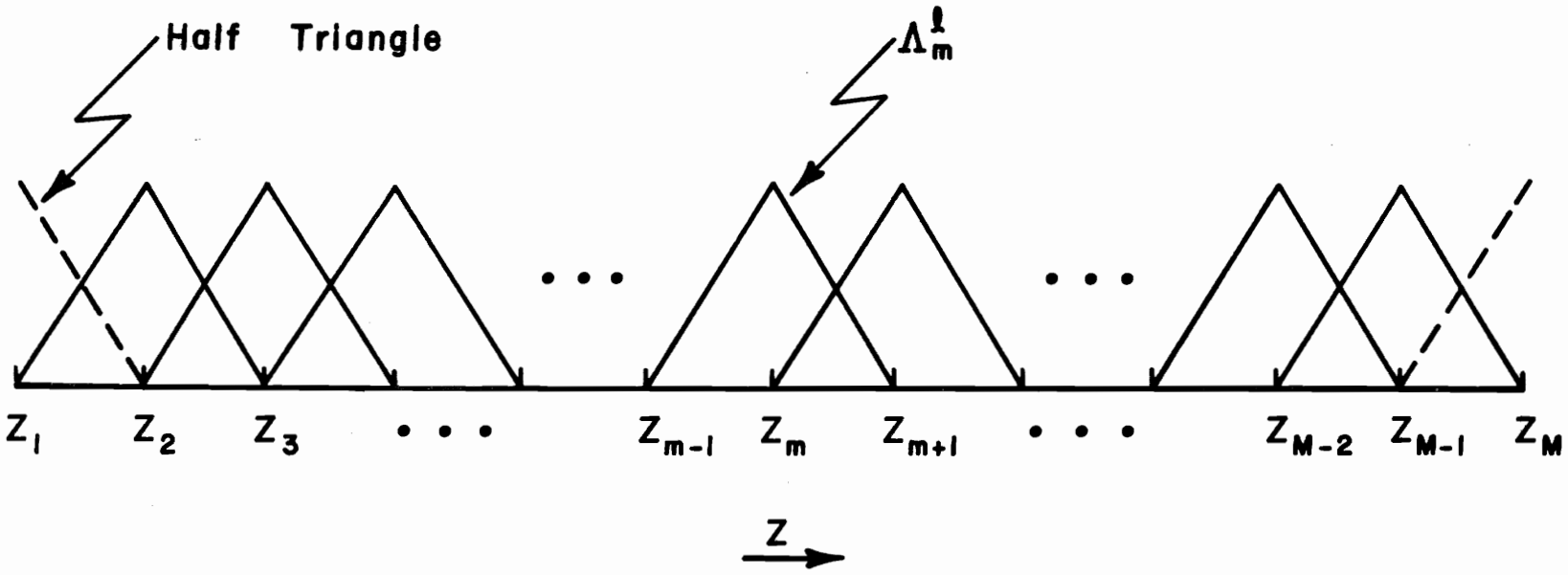

Figure 8. Testing Triangle Functions

Since the testing function Λ_m^{ℓ} is zero outside the sub-domain $z\varepsilon(z_{m-1},z_{m+1})$, one sees immediately that (70), subject to (71) and (72), reduces to ($T_m=\Lambda_m^{\ell}$)

$$-\int_{z=z_1}^{z_2}\left(\frac{\partial}{\partial z}\Phi(r,z) + j\omega A_z(r,z)\right)\Lambda_1^{\ell}(z)dz = \int_{z=z_1}^{z_2} E_z^s(r,z)\Lambda_1^{\ell}(z)dz \quad , \qquad (74a)$$

$$(m=1)$$

$$-\int_{z=z_{m-1}}^{z_{m+1}}\frac{\partial}{\partial z}\Phi(r,z) + j\omega A_z(r,z)\ \Lambda_m^{\ell}(z)dz = \int_{z=z_{m-1}}^{z_{m+1}} E_z^s(r,z)\Lambda_m^{\ell}(z)dz \quad , \qquad (74b)$$

$$m = 2,3,\ldots,M-1$$

and

$$-\int_{z=z_{M-1}}^{z_M}\left(\frac{\partial}{\partial z}\Phi(r,z) + j\omega A_z(r,z)\right)\Lambda_M^{\ell}(z)dz = \int_{z=z_{M-1}}^{z_M} E_z^s(r,z)\Lambda_M^{\ell}(z)dz \quad , \qquad (74c)$$

$$(m=M)$$

One integration by parts applied to the portion of each of the integrands in (74) involving Φ reduces the above to

$$\Phi(r,z_1) - \frac{1}{\Delta}\int_{z=z_1}^{z_2}\Phi(r,z)dz \quad -j\omega\int_{z=z_1}^{z_2}A_z(r,z)\Lambda_1^{\ell}(z)dz$$

$$= \int_{z=z_1}^{z_2}E_z^s(r,z)\Lambda_1^{\ell}(z)dz \ , \quad (75a)$$

$$(m=1)$$

$$\frac{1}{\Delta}\int_{z=z_{m-1}}^{z_m}\Phi(r,z)dz - \frac{1}{\Delta}\int_{z=z_m}^{z_{m+1}}\Phi(r,z)dz \ -j\omega\int_{z=z_{m-1}}^{z_{m+1}}A_z(r,z)\Lambda_m^{\ell}(z)dz$$

$$= \int_{z=z_{m-1}}^{z_{m+1}}E_z^s(r,z)\Lambda_m^{\ell}(z)dz \ , \quad (75b)$$

$$m = 2,3,4,\ldots,M-1$$

and

$$-\Phi(r,z_M) + \frac{1}{\Delta}\int_{z=z_{M-1}}^{z_M}\Phi(r,z)dz - j\omega\int_{z=z_{M-1}}^{z_M}A_z(r,z)\Lambda_M^{\ell}(z)dz$$

$$= \int_{z=z_{M-1}}^{z_M} E_z^s(r,z)\Lambda_M^{\ell}(z)dz \quad , \qquad (75c)$$

$$(m=M)$$

The testing functions, often called triangle functions, are illustrated in Fig. 8 . For m=2,3,...,M-1, the testing functions are interior full triangles and are associated with Eq. (75b). On the other hand, due to the integration limits on (71), testing with Λ_1^{ℓ} is equivalent to testing with a half-triangle on the lower end while use of Λ_M^{ℓ} yields the same results as would a half-triangle on the upper end (Fig. 8).

The vector potential A_z due to currents on a wire is reasonably slowly varying with z. Therefore, with Δ sufficiently small relative to wavelength, the approximations below are quite good, and they significantly lessen the computational complexity of the present analysis:

$$\int_{z=z_1}^{z_2} A_z(r,z)\Lambda_1^{\ell}(z)dz \doteq \frac{\Delta}{2}\,A_z(r,z_1) \quad , \quad \Delta<<\lambda \qquad (76a)$$

$$\int_{z=z_{m-1}}^{z_{m+1}} A_z(r,z)\Lambda_m^{\ell}(z)dz \doteq \Delta A_z(r,z_m) \quad , \quad \Delta<<\lambda \tag{76b}$$

$$\int_{z=z_{M-1}}^{z_M} A_z(r,z)\Lambda_M^{\ell}(z)dz \doteq \frac{\Delta}{2} A_z(r,z_M) \quad , \quad \Delta<<\lambda \tag{76c}$$

The same type approximation can be applied to the right-hand sides of (75), but is usually unnecessary because the indicated integration can almost always be performed analytically. However, in the interest of notational convenience, the following definitions are employed:

$$V^s(r,z_1) = \int_{z=z_1}^{z_2} E_z^s(r,z)\Lambda_1^{\ell}(z)dz \tag{77a}$$

$$V^s(r,z_m) = \int_{z=z_{m-1}}^{z_{m+1}} E_z^s(r,z)\Lambda_m^{\ell}(z)dz \quad , \quad m=2,3,\ldots,M-1 \tag{77b}$$

$$V^s(r,z_M) = \int_{z=z_{M-1}}^{z_M} E_z^s(r,z)\Lambda_M^{\ell}(z)dz \tag{77c}$$

With the approximations (76) and definitions (77), the three equations of (75) can be written in the form

$$\Phi(r,z_1) - \frac{1}{\Delta}\int_{z=z_1}^{z_2}\Phi(r,z)dz - j\omega\,\frac{\Delta}{2}\,A_z(r,z_1) = V^s(r,z_1) \qquad (78a)$$

$$(m=1)$$

$$\frac{1}{\Delta}\int_{z=z_{m-1}}^{z_m}\Phi(r,z)dz - \frac{1}{\Delta}\int_{z=z_m}^{z_{m+1}}\Phi(r,z)dz - j\omega\Delta A_z(r,z_m) = V^s(r,z_m)\ , \qquad (78b)$$

$$m=2,3,\ldots,M-1$$

$$-\Phi(r,z_M) + \frac{1}{\Delta}\int_{z=z_{M-1}}^{z_M}\Phi(r,z)dz - j\omega\,\frac{\Delta}{2}\,A_z(r,z_M) = V^s(r,z_M)\ , \qquad (78c)$$

$$(m=M)$$

b. Current Approximation

The next step in the numerical solution procedure is to approximate the unknown current I(z) in a series of the form

$$I(z) = \sum_{n=1}^{N} I_n i_n(z) \qquad (79)$$

where each $i_n(z)$ is a known element of a basis set selected for representing the current, and I_n is the unknown complex coefficient of the n^{th} term in the series (79). It is the set of coefficients $\{I_n\}$ that one seeks to determine in the numerical procedure. A_z and Φ are written as functions of the terms in (79) and then are substituted into (78), which leads to a system of linear equations that, subject to boundary conditions, can be solved for $\{I_n\}$.

A very useful basis set in terms of which to represent the current on the stepped-radius wire is that comprising the so-called pulse functions ($i_n = p_n$):

$$p_n(z) = \begin{cases} 1 & z\varepsilon(z_n - \Delta/2,\ z_n + \Delta/2) \\ 0 & z\notin(z_n - \Delta/2,\ z_n + \Delta/2) \end{cases} \tag{80}$$

where z_n locates the center of the n^{th} pulse. A representative pulse is shown in Fig. 9 together with half-pulses on the ends of the interval (z_1, z_M). The number of pulses, including the two half-pulses, is chosen to be equal to M, the number of testing triangles.

c. A_z and Φ in Terms of I_n

The vector potential A_z due to the approximation given in (79) is conveniently written

$$A_z(r,z) = \sum_{n=1}^{M} I_n A_n(r,z,R) \tag{81}$$

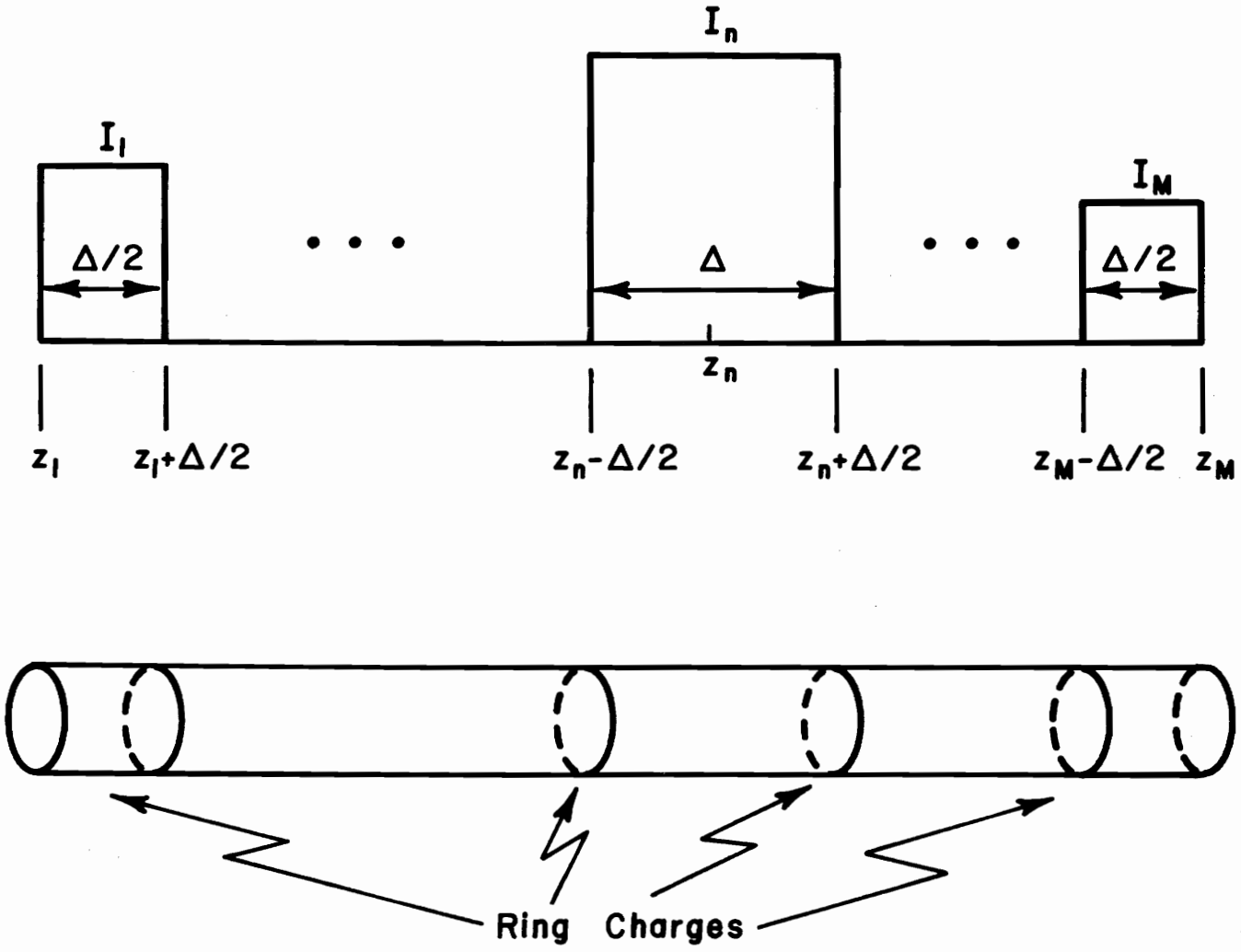

Figure 9. Pulse Currents and Ring Charges

In (81) A_n is the contribution to the total vector potential A_z from the n^{th} pulse:

$$A_1(r,z,R) = \frac{\mu}{4\pi} \int_{z'=z_1}^{z_1+\Delta/2} g(z-z',r,R)\,dz' \tag{82a}$$

$$A_n(r,z,R) = \frac{\mu}{4\pi} \int_{z'=z_n-\Delta/2}^{z_n+\Delta/2} g(z-z',r,R)\,dz' \ , \tag{82b}$$

$$n=2,3,\ldots,M-1$$

$$A_M(r,z,R) = \frac{\mu}{4\pi} \int_{z'=z_M-\Delta/2}^{z_M} g(z-z',r,R)\,dz' \tag{82c}$$

where R is the radius of the wire on which resides the current I being approximated by the given pulse and where μ is the permeability of the medium in which the wire resides. In (82) the kernel is given by

$$g(\xi,r,R) = \frac{1}{2\pi} \int_{\phi'=-\pi}^{\pi} \frac{e^{-jk[\xi^2+r^2+R^2-2rR\,\cos\phi']^{\frac{1}{2}}}}{[\xi^2+r^2+R^2-2rR\,\cos\phi']^{\frac{1}{2}}}\,d\phi' \tag{83}$$

where k is $2\pi/\lambda$. By a suitable change of variables in each expression of (82), these integrals can be converted to the following, which are far better suited for computation than are those of (82):

$$A_1(r,z,R) = \frac{\mu}{4\pi} \int_{z'=0}^{\Delta/2} g(z-z'-z_1,r,R)dz' \qquad (84a)$$

$$A_n(r,z,R) = \frac{\mu}{4\pi} \int_{z'=-\Delta/2}^{\Delta/2} g(z-z'-z_n,r,R)dz' \qquad (84b)$$

$$n=2,3,\ldots,M-1$$

$$A_M(r,z,R) = \frac{\mu}{4\pi} \int_{z'=-\Delta/2}^{0} g(z-z'-z_M,r,R)dz' \qquad (84c)$$

The scalar potential Φ due to the charge associated with the current approximation (79), with the pulses of (80), is to be calculated as a sum of partial potentials,

$$\Phi(r,z) = \sum_{n=1}^{M} I_n \Phi_n(r,z,R) \ , \qquad (85)$$

where, of course, Φ_n is that contribution to Φ due to the charge related to p_n. As suggested in Fig. 9 , current on a cylinder in the form of a pulse "deposits" a discrete ring of charge at the upper and lower ends of the pulse, where it is discontinuous. Since the derivative of the pulse is zero other than at the points of discontinuity, no other charge, e.g., linear charge density, is associated with the current

pulse. The total charge deposited at the n^{th} pulse's upper end-point, $z_M+\Delta/2$, is $-\frac{1}{j\omega}$ and that at its lower end-point, $z_M-\Delta/2$, is $+\frac{1}{j\omega}$. The current on the wire surface is assumed to be uniform around the wire circumference so each ring of charge is of constant linear density: $\mp\frac{1}{j\omega 2\pi R}$ at $z_n\pm\Delta/2$. Now, each partial potential Φ_n is seen to be

$$\Phi_1(r,z,R) = -\frac{1}{j4\pi\omega\varepsilon}\left[g(z-z_1-\Delta/2,r,R) - g(z-z_1,r,R)\right] \qquad (86a)$$

$$\Phi_n(r,z,R) = -\frac{1}{j4\pi\omega\varepsilon}\left[g(z-z_n-\Delta/2,r,R) - g(z-z_n+\Delta/2,r,R)\right], \qquad (86b)$$

$$n=2,3,\ldots,M-1$$

$$\Phi_M(r,z,R) = -\frac{1}{j4\pi\omega\varepsilon}\left[g(z-z_M,r,R) - g(z-z_M+\Delta/2,r,R)\right] \qquad (86c)$$

where ε is the permittivity of the medium surrounding the wire structure.

d. Linear System of Equations for Stepped-Radius Scatterer

If A_z of (81) and Φ of (85) subject, respectively, to (82) and (86), are substituted into (78), one obtains a system of linear algebraic equations having the current coefficients I_n's as unknowns. This system of equations comes from testing

(67) with the triangle testing functions, and it contains the same information as does (67).

At this point we adapt the system of equations to the stepped-radius wire scatterer. The scheme for applying the above to the stepped-radius problem is suggested graphically in Fig. 10. In this example, the portion of the stepped-radius wire between $z=-L/2$ and $z=s$ (step location) is divided into six subintervals of length $\Delta_b=[s+L/2]/6$, and the remaining portion is divided into three subintervals of length $\Delta_a=(L/2-s)/3$. Next (78) is applied individually to the interval $z\varepsilon(-L/2,s)$ and to $z\varepsilon(s,L/2)$, and the currents I_b and I_a are approximated by pulses in the respective intervals. The testing triangles and the pulses are observed in Fig. 10 where one sees that the coefficients I_1^b and I_{10}^a of the end half-pulses are made equal to zero so that $I_b(-L/2)=0$ and $I_a(L/2)=0$--current boundary conditions at free wire ends. With $I_1^b=I_{10}^a=0$, the number of unknowns is reduced by two, and, thus, (78a) applied in $(-L/2,s)$ and (78c) applied in $(s,L/2)$ are deleted to reduce correspondingly the number of equations in the linear system. Also, notice that the current is made continuous at the step by the composition of the 7^{th} pulse; this pulse occupies an interval of length $\frac{1}{2}(\Delta_a+\Delta_b)$ and is the combination of the upper half-pulse on the larger-radius wire and the lower half-pulse on the smaller-radius wire. Combining the two half-pulses at the step into a single pulse ($I_7^b=I_7^a=I$) reduces the number of unknowns by one, and a corre-

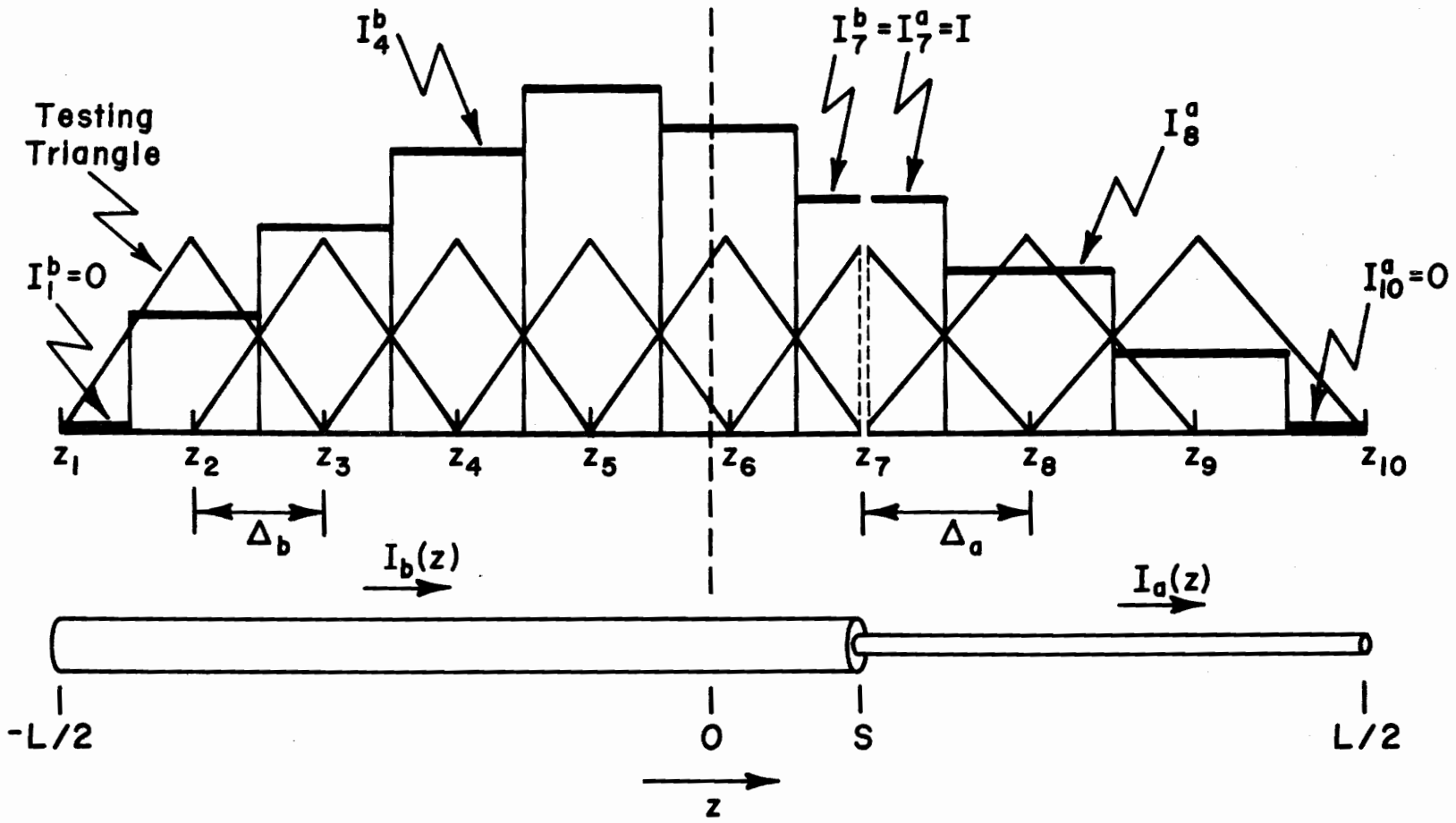

Figure 10. Stepped-Radius Wire, Testing Triangles, and Pulse Current

sponding reduction is achieved in the linear system by adding (78c), applied in (-L/2,s), to (78a), applied in (s,L/2).

With the current represented by pulses and with the testing of (67) (leading to (78)) suggested by the triangles in Fig. 10, one applies (68) to E_z^s in (77) and enforces (78) on the surface of the larger-radius wire and on the surface of the smaller-radius wire. The linear system resulting from the above applications of (78) to the two wires in the structure of Fig. 10 can be readily solved for the current coefficients I_n^a and I_n^b.

For a general stepped-radius scatterer, one would divide (s+L/2) into N_b segments of length $\Delta_b=(s+L/2)/N_b$ and (L/2-s) into N_a segments of length $\Delta_a=(L/2-s)/N_a$. Then, applying the scheme described above for the example of Fig.10, he would establish the following system of linear algebraic equations:

$$\sum_{n=2}^{N_b} I_n^b Z_{mn}^{bb} + IZ_m^b + \sum_{n=N_b+2}^{N_a+N_b} I_n^a Z_{mn}^{ba} = V_m^b \,, \qquad m=2,3,\ldots,N_b \tag{87a}$$

$$\sum_{n=2}^{N_b} I_n^b Z_n^{sb} + IZ^s + \sum_{n=N_b+2}^{N_a+N_b} I_n^a Z_n^{sa} = V^s \tag{87b}$$

$$\sum_{n=2}^{N_b} I_n^b Z_{mn}^{ab} + IZ_m^a + \sum_{n=N_b+2}^{N_a+N_b} I_n^a Z_{mn}^{aa} = V_m^a \,, \qquad (87c)$$

$$m=N_b+2,\ldots,N_a+N_b$$

where I_n^a and I_n^b are the weighting coefficients of the pulse approximations for I_a and I_b, respectively. The elements in the above linear system are defined in (88).

$$V_m^r = -\int_{z=z_{m-1}}^{z_{m+1}} E_z^i(r,z)\Lambda_m^\ell(z)dz \qquad (88a)$$

$$V^s = -\frac{1}{\Delta_b}\int_{z=s-\Delta_b}^{s} E_z^i(b,z)\left[\Delta_b - s + z\right] dz$$

$$-\frac{1}{\Delta_a}\int_{z=s}^{s+\Delta_a} E_z^i(a,z)\left[\Delta_a - z + s\right] dz \qquad (88b)$$

$$Z_{mn}^{rR} = \frac{1}{\Delta_r}\left(\int_{z=z_m-\Delta_r}^{z_m} - \int_{z=z_m}^{z_m+\Delta_r}\right)\left[\Phi_n(r,z,R)\right]\,dz - j\omega\Delta_r A_n(r,z_m,R) \tag{88c}$$

$$Z_n^{sR} = \frac{1}{\Delta_b}\int_{z=s-\Delta_b}^{s}\Phi_n(b,z,R)dz - \frac{1}{\Delta_a}\int_{z=s}^{s+\Delta_a}\Phi_n(a,z,R)dz - j\,\frac{\omega}{2}\left[\Delta_b A_n(b,s,R) + \Delta_a A_n(a,s,R)\right] \tag{88d}$$

$$Z_m^r = \frac{1}{j4\pi\omega\epsilon\Delta_r}\left(\int_{z=z_m-\Delta_r}^{z_m} - \int_{z=z_m}^{z_m+\Delta_r}\right)\left[g(z-s+\Delta_b/2,r,b) - g(z-s-\Delta_a/2,r,a)\right]\,dz$$

$$-j\,\frac{\omega\mu}{4\pi}\,\Delta_r\left[\int_{z'=s-\Delta_b/2}^{s} g(z_m-z',r,b)dz' + \int_{z'=s}^{s+\Delta_a/2} g(z_m-z',r,a)dz'\right] \tag{88e}$$

$$Z^s = \frac{1}{j4\pi\omega\epsilon}\left\{ \frac{1}{\Delta_b}\int_{z=s-\Delta_b}^{s}\left[g(z-s+\Delta_b/2,b,b) - g(z-s-\Delta_a/2,b,a)\right]\,dz \right.$$

$$\left. - \frac{1}{\Delta_a}\int_{z=s}^{s+\Delta_a}\left[\,g(z-s+\Delta_b/2,a,b) - g(z-s-\Delta_a/2,a,a)\right]\,dz \right\}$$

$$-j\,\frac{\omega\mu}{8\pi}\left\{\Delta_b\int_{z'=s-\Delta_b/2}^{s} g(z_m-z',b,b)dz' + \Delta_a\int_{z'=s}^{s+\Delta_a/2} g(z_m-z',a,a)dz'\right\} \qquad (88f)$$

For a specified incident field having a z component E_z^i, the system of equations (87), with the definitions of (88), can be solved for $\{I_n^a\}$ and $\{I_n^b\}$ from which a pulse approximation for current on the scatterer is readily available.

e. Reduced Kernel

Although the exact kernel of (83) can be calculated by means of elliptic integrals and can be employed in the computation of quantities above, an approximation of (83) lessens the computer time required in calculations.

The distance from a point (r,0) on the inner circle of Fig. 11 to (R,ϕ') on the outer circle is, from the law of cosines, $[r^2+R^2-2rR\cos\phi']^{\frac{1}{2}}$. The maximum value of this distance is $[r^2+R^2+2rR]^{\frac{1}{2}}$ and the minimum is $[r^2+R^2-2rR]^{\frac{1}{2}}$ from which one determines the median distance to be $\left[\frac{r^2+R^2}{2}\right]^{\frac{1}{2}}$. Hence, one replaces $(r^2+R^2-2rR\cos\phi')$ in (83) by $(r^2+R^2)/2$ and arrives at a reduced or average kernel for the stepped-radius wire:

$$K(\xi,r,R) \doteq \frac{e^{-jk[\xi^2+\frac{1}{2}(r^2+R^2)]^{\frac{1}{2}}}}{[\xi^2+\frac{1}{2}(r^2+R^2)]^{\frac{1}{2}}} \tag{89}$$

The viewpoint above leading to (89) is precisely that in thin-wire theory from which the usual approximate kernel stems, and, indeed, for a constant-radius wire, (89) reduces to the usual

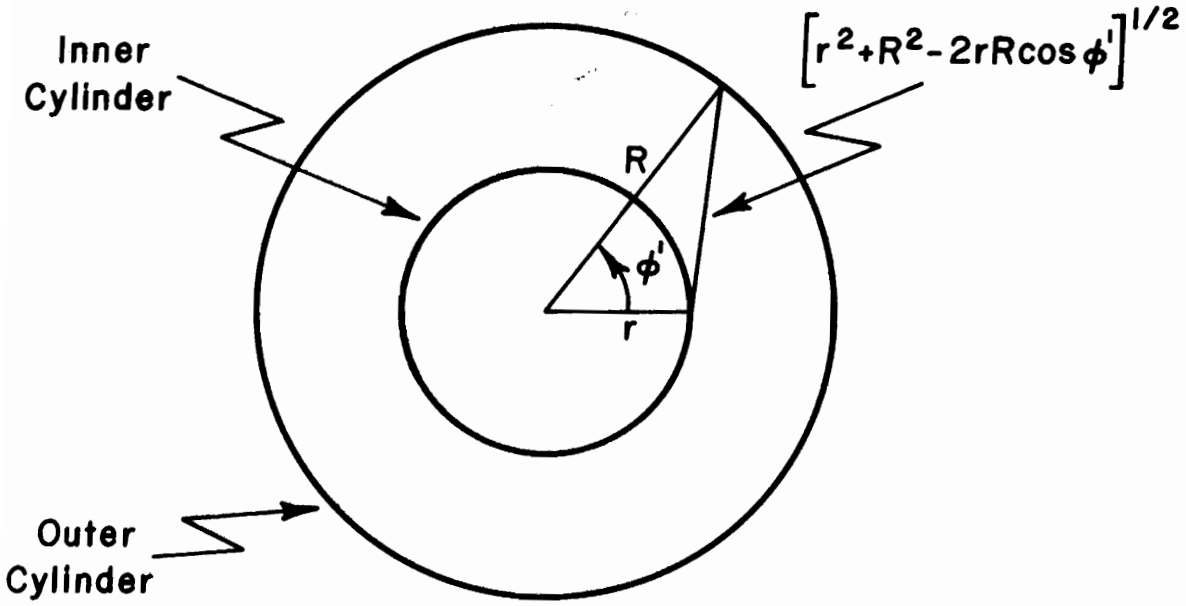

Figure 11. Distance in Transverse Plane between Points on Coaxial Cylinders

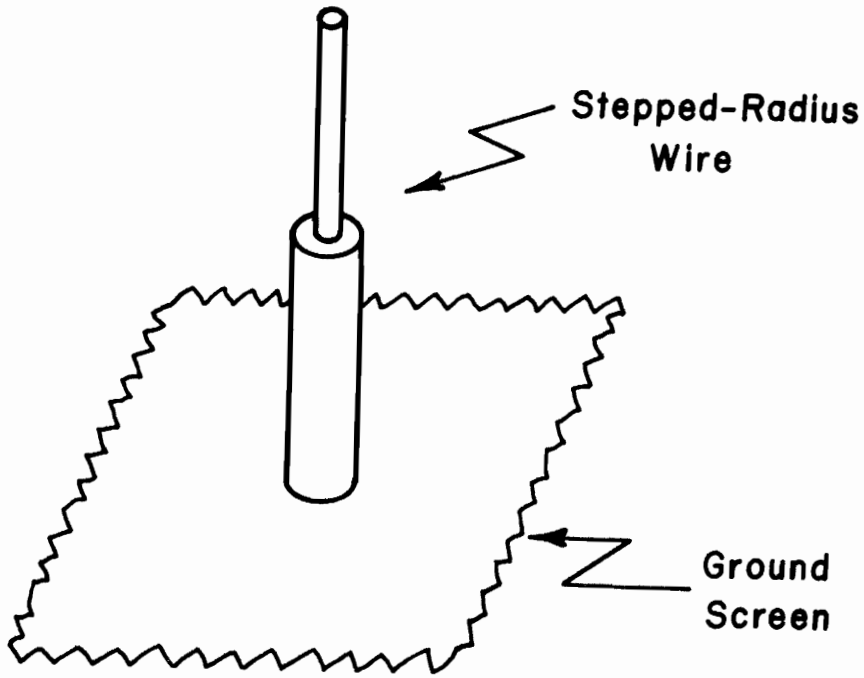

Figure 12. Stepped-Radius Wire Above Ground

kernel. Selected sample calculations employing (89) yield results which exhibit no significant error compared with results based upon the exact kernel (83), and, therefore, in the interest of efficiency, calculations reported here are based upon (89).

f. Stepped-Radius Antenna

If one wishes to determine the current on a stepped-radius antenna, driven at $z=z_g$ by an emf source of V volts, he simply replaces E_z^i of (88) by $V\delta(z-z_g)$ as suggested in (69). With this replacement, the linear system (87) can be solved for the antenna current.

g. Scatterer or Antenna above Ground

To analyze a stepped-radius structure above and perpendicular to a perfectly conducting ground screen as depicted in Fig. 12, one only has to appeal to symmetry and to modify the kernel, (83) or (89), in the usual way.

3. SAMPLE RESULTS

In Figs. 13-24 are presented selected results of currents on stepped-radius wires. In all cases the presence of the step influences the magnitude of current relative to what it would have been on a constant-radius wire, but the effect on the shape of the distribution depends upon length and certain features of the excitation.

Near resonance, where the forced response is dominated by the resonant response, the distribution is little affected

by the presence of the step or its position on the wire. This is supported by the data of Figs. 13-15 where are displayed currents on wires which have steps in various locations and which are illuminated by a normally incident plane wave.

Those knowledgeable in thin-wire theory are aware that the forced current is dominant on a 1λ wire which is symmetrically excited and they know that this response is essentially a shifted cosine function. Only, if the forcing function possesses an odd-function component, can the resonant current respond on a 1λ wire of constant radius. On the other hand, in the case of a 1λ stepped-radius wire having, of course, the odd symmetry within the structure itself, one does expect a component of resonant current. This is vividly exhibited by the data of Fig. 16 where one sees a significant change in the real current on a stepped-radius wire over that on a constant-radius wire.

Fig. 17 shows the current on a stepped-radius scatterer caused by plane wave illumination impinging upon the wire at angles θ (w.r.t. z axis). Figs. 18 and 19 provide information on the variation of peak current on stepped-radius scatterers of lengths below and above λ/2.

Figs. 20-23 give comparative data for 1λ antennas excited symmetrically and antisymmetrically. Again one observes little influence on current due to the presence of the step at s=0 when the excitation is an odd function, but a marked effect is seen in the case of even-function excitation.

Lastly, shown in Fig. 24 is the current on a stepped-radius monopole above a ground plane. The inherent symmetry of such an antenna suggests that no major change in shape of current is to be expected, and this is corroborated by the results of Fig. 24.

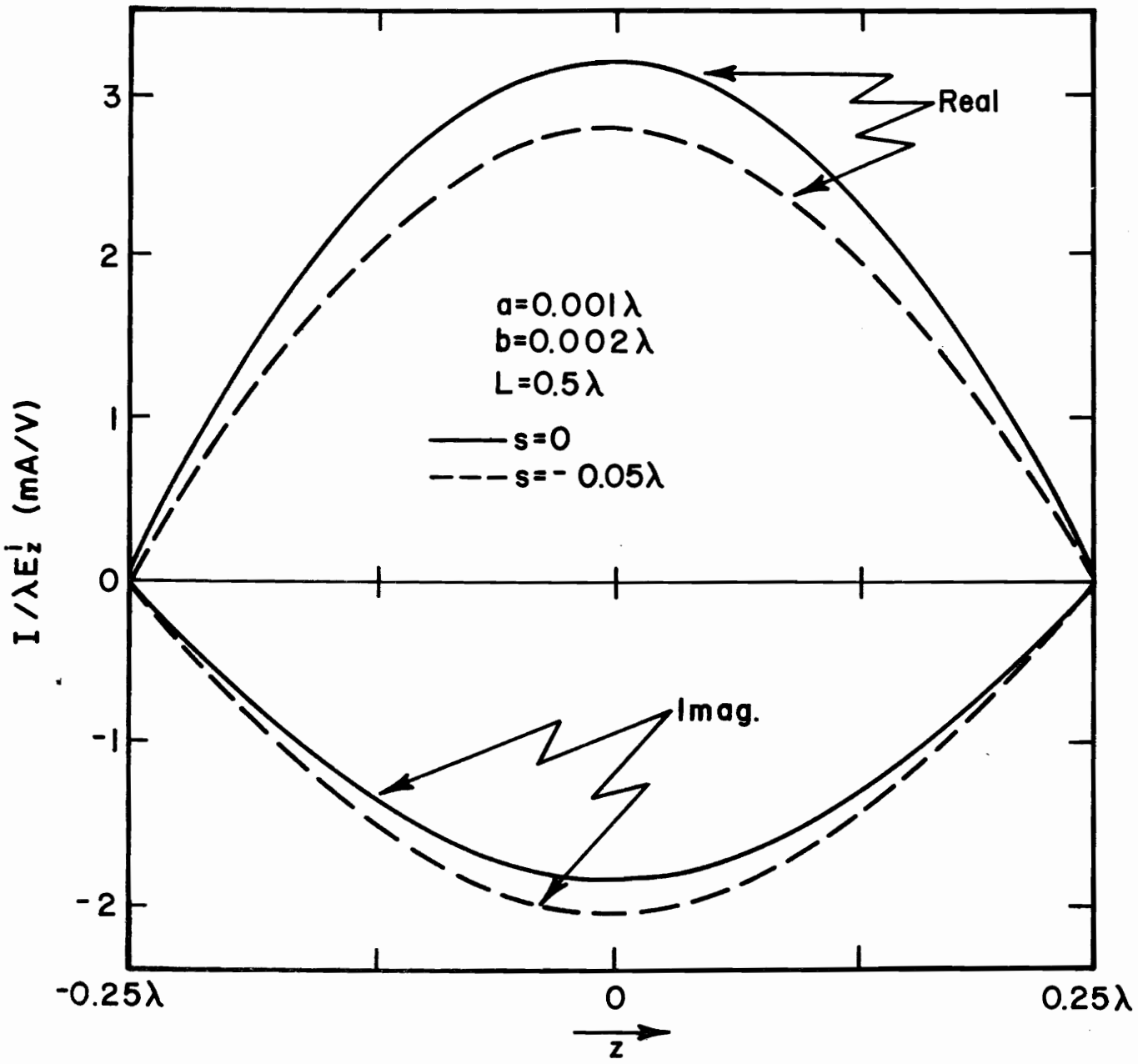

Figure 13. Current Induced on a Half-Wavelength, Stepped-Radius Scatterer by a Normally Incident Plane Wave

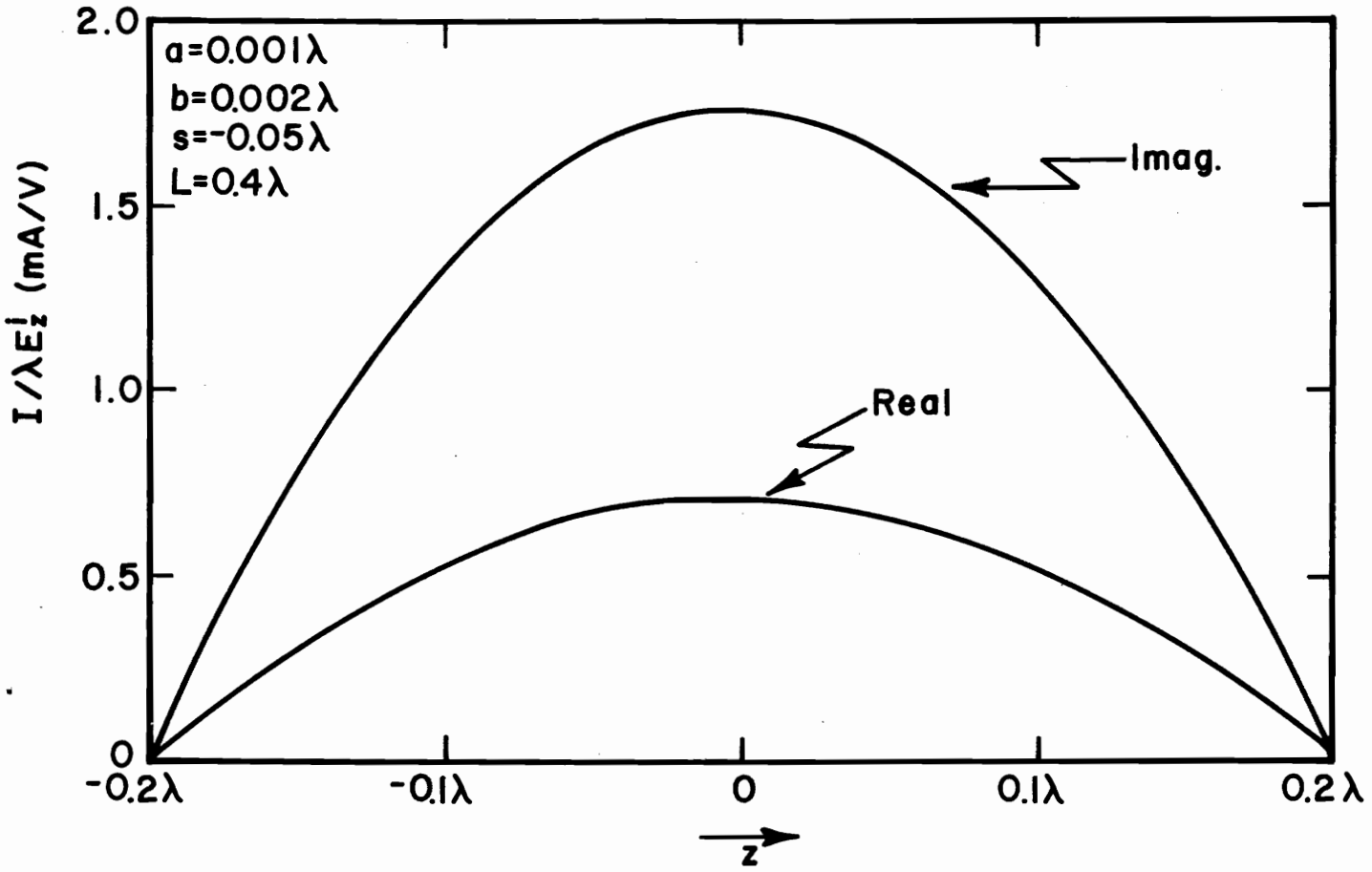

Figure 14. Current Induced on a 4λ/10 Stepped-Radius Scatterer by a Normally Incident Plane Wave

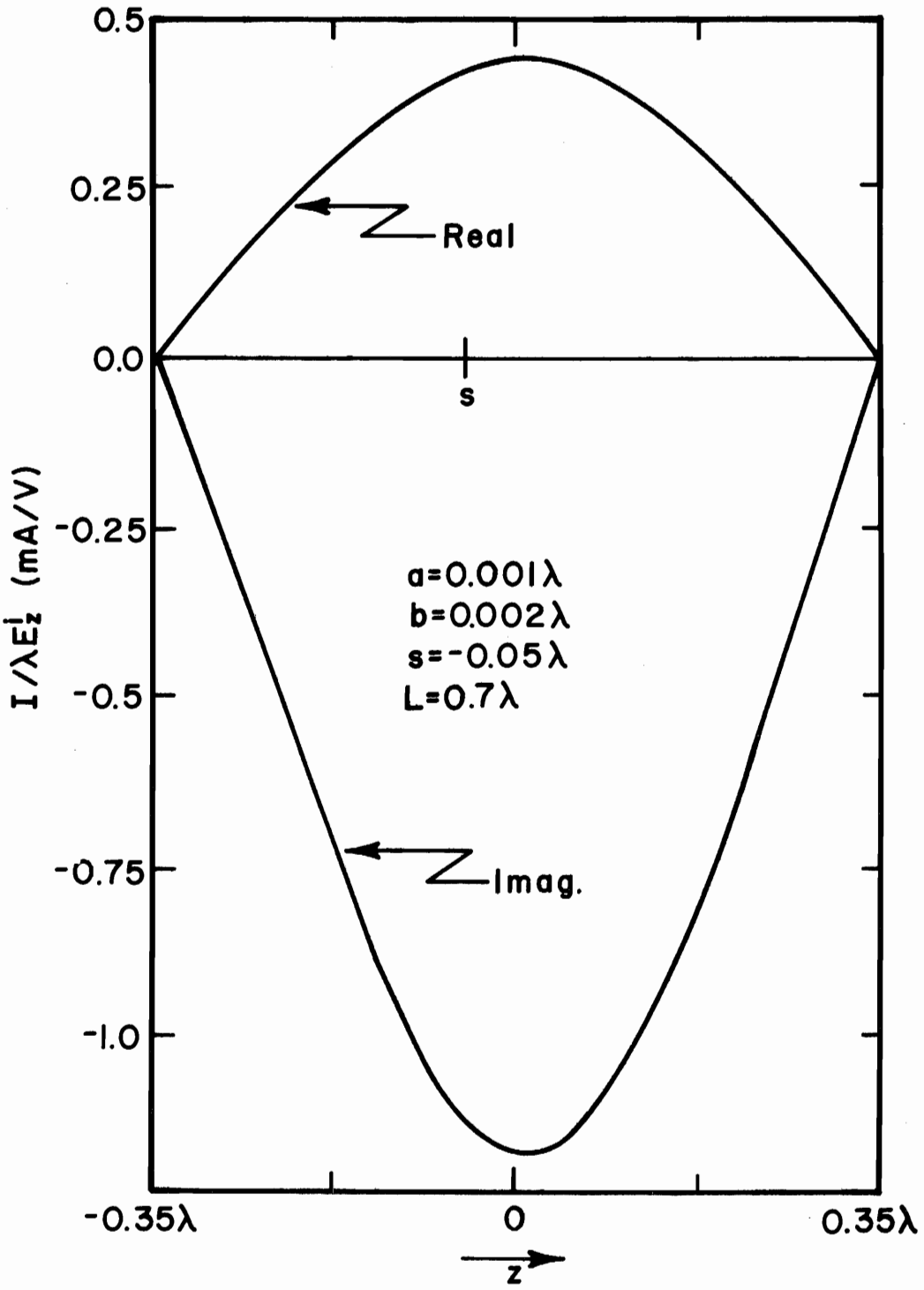

Figure 15. Current Induced on 7λ/10 Stepped-Radius Scatterer by a Normally Incident Plane Wave

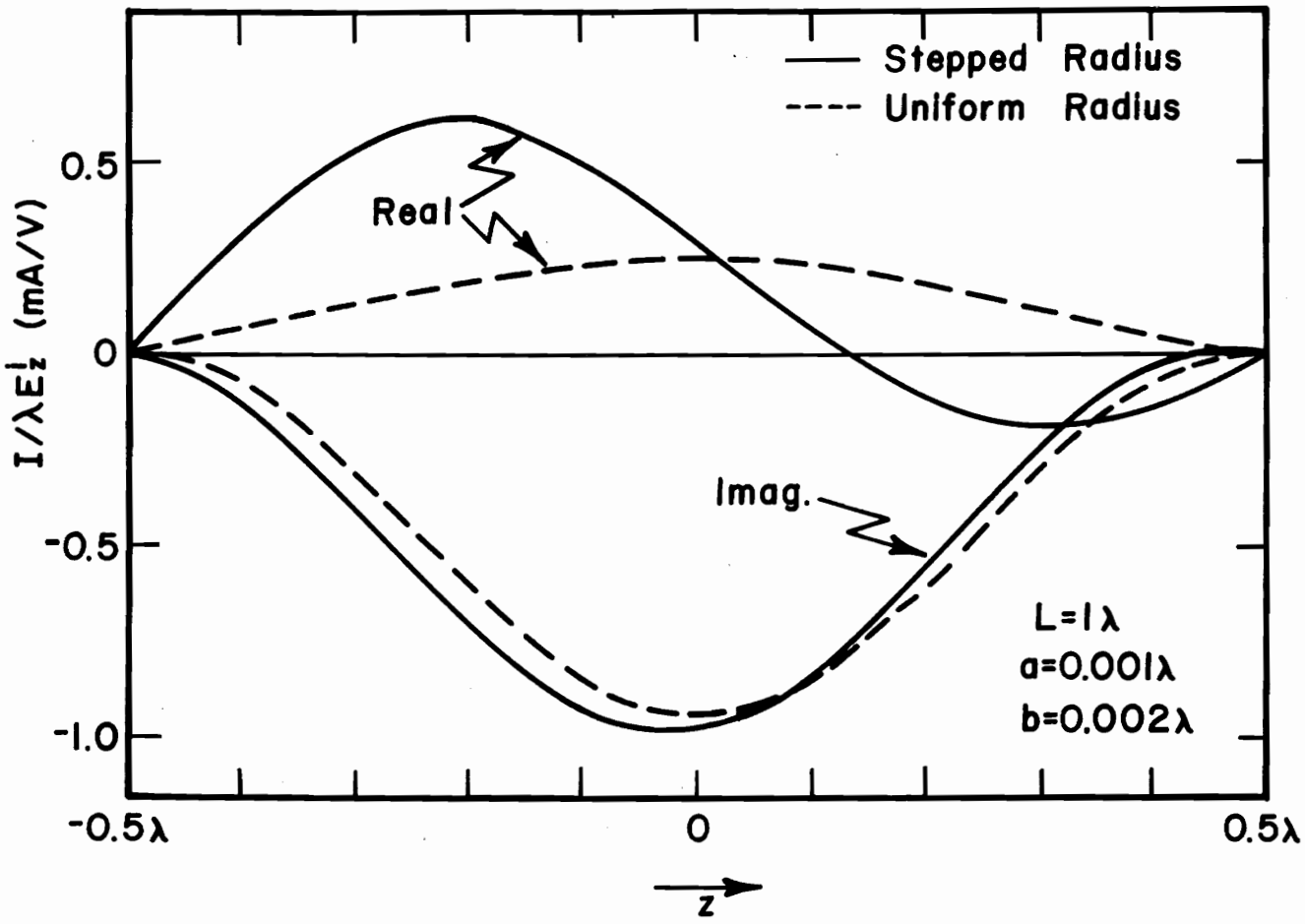

Figure 16. Current induced on a One-Wavelength Stepped-Radius and a Constant-Radius Scatterer by a Normally Incident Plane Wave

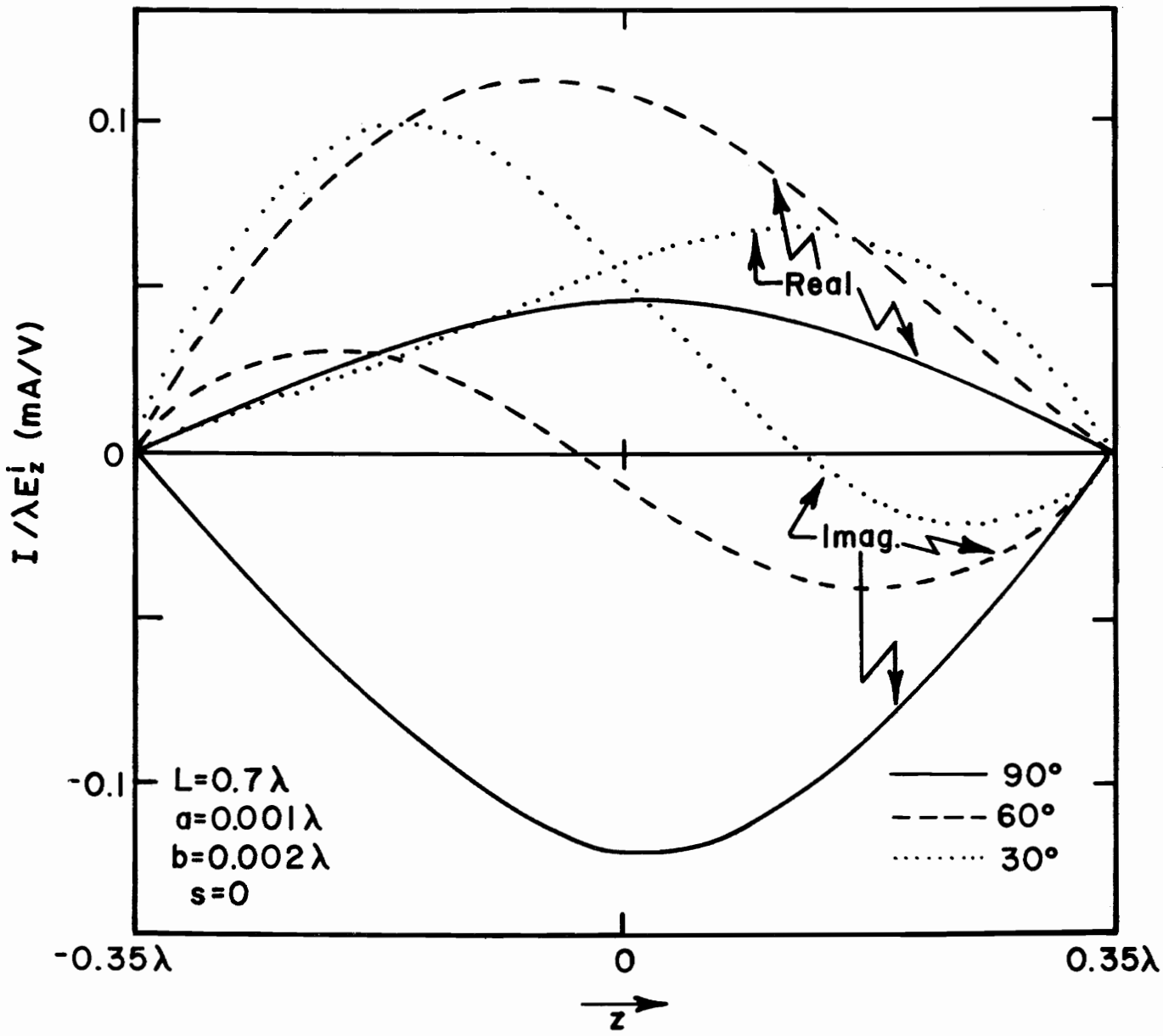

Figure 17. Current Induced on a 7λ/10 Stepped-Radius Scatterer by Obliquely Incident Plane Wave

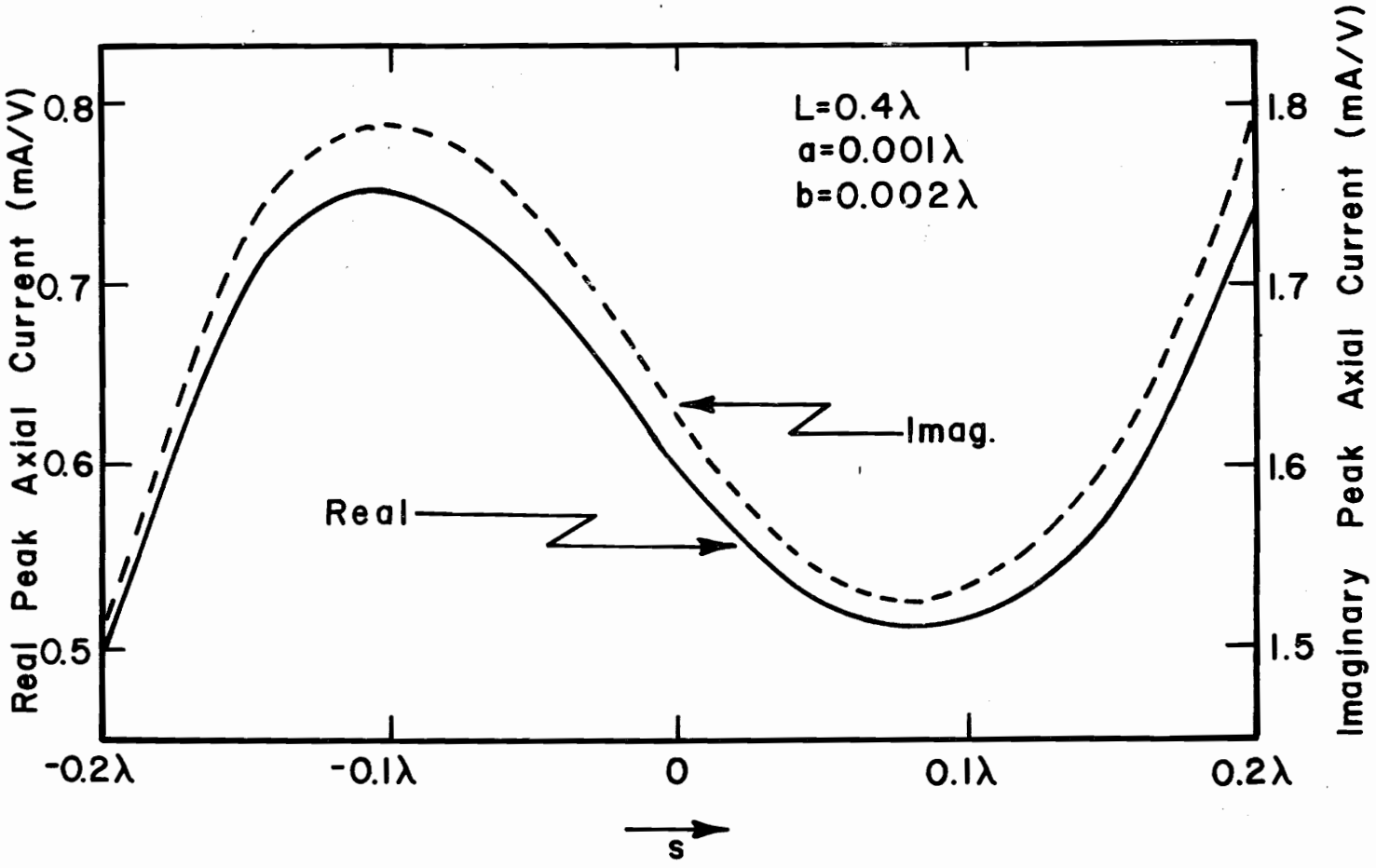

Figure 18. Variation with Step Location of Peak Current Induced on a 4λ/10 Stepped-Radius Scatterer by a Normally Incident Plane Wave

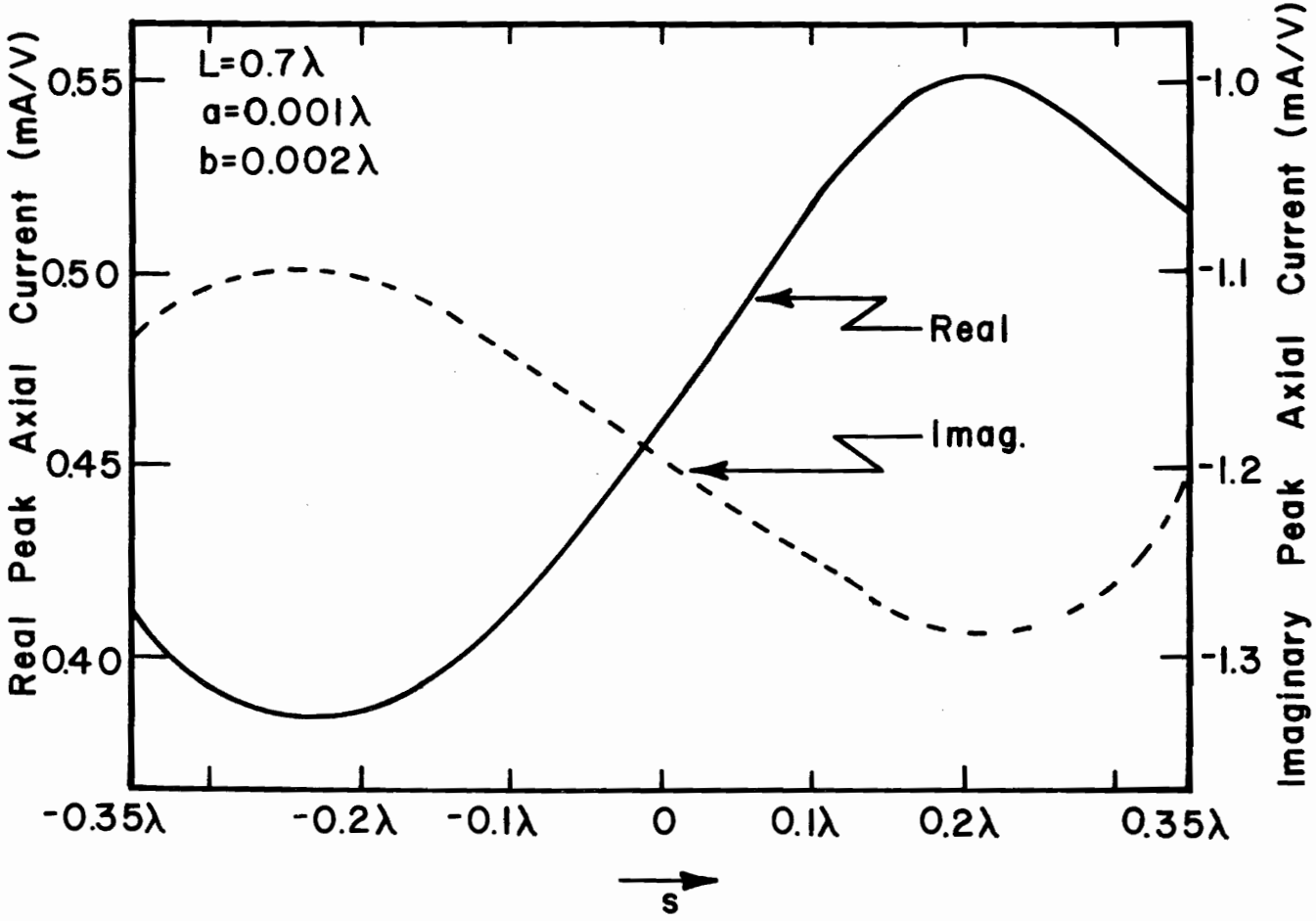

Figure 19. Variation with step location of Peak Current Induced on a 7λ/10 Stepped-Radius Scatterer by a Normally Incident Plane Wave

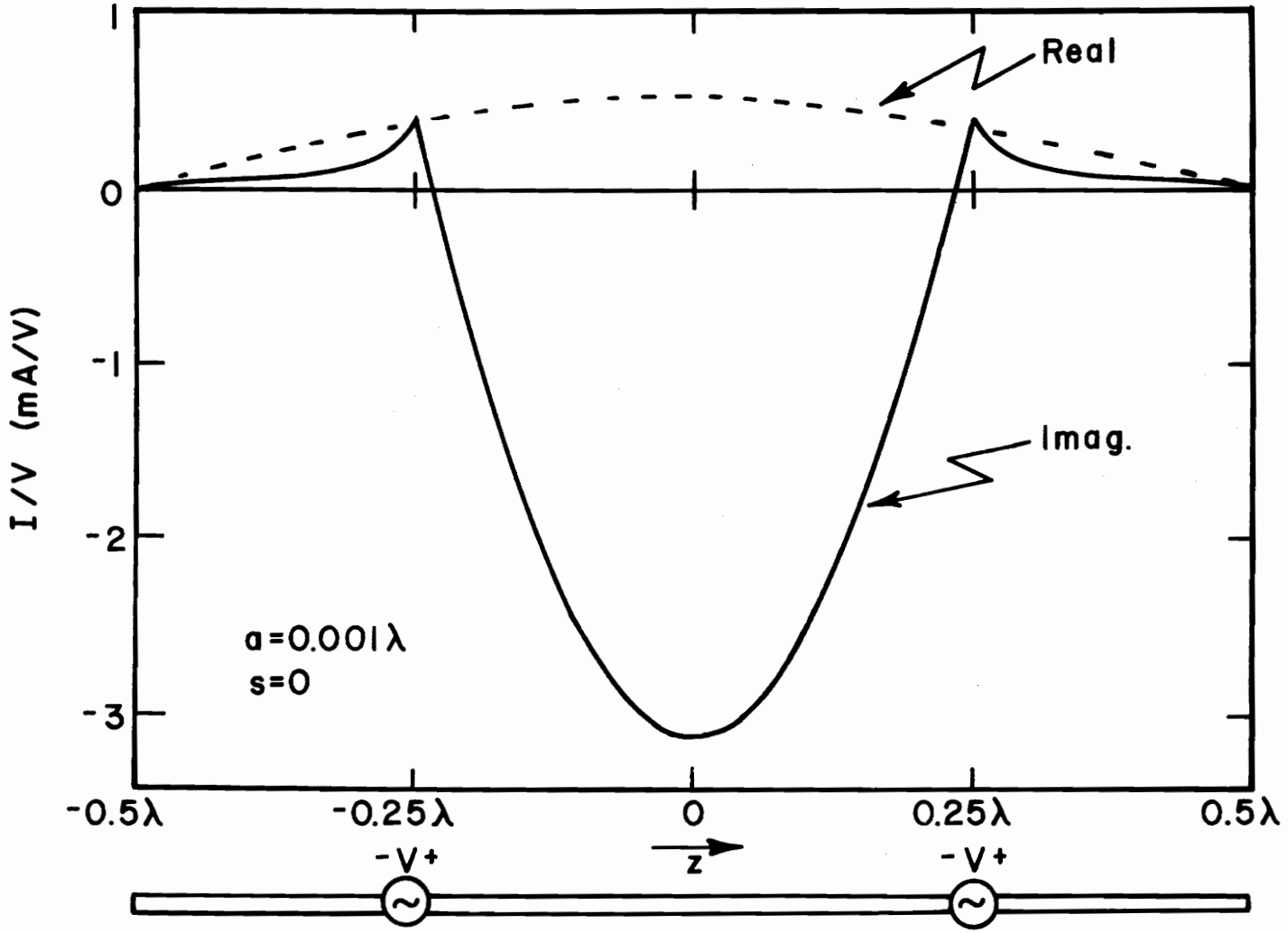

Figure 20. Current on Symmetrically Excited, One-Wavelength Uniform-Radius Antenna

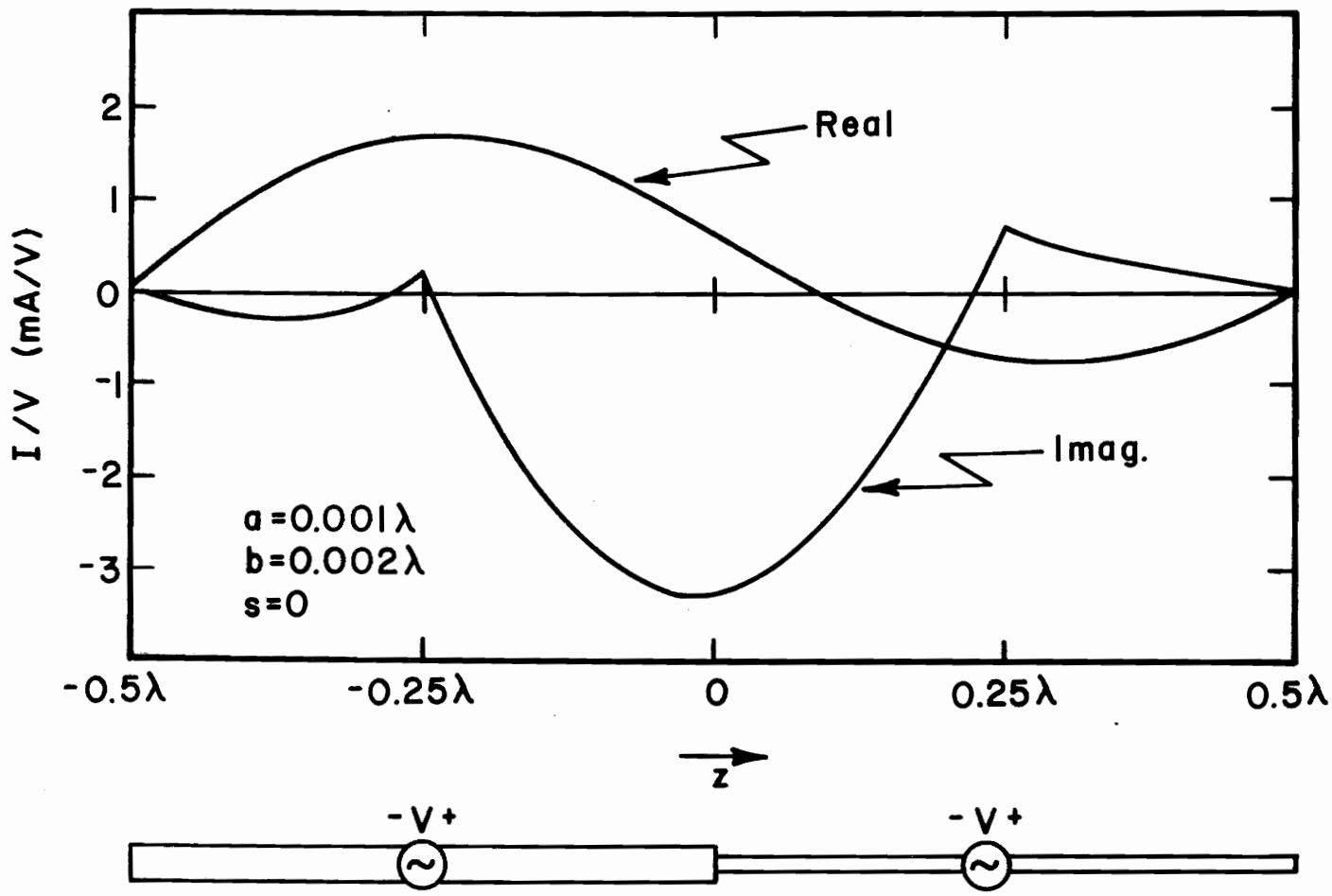

Figure 21. Current on Symmetrically Excited, One-Wavelength, Stepped-Radius Antenna

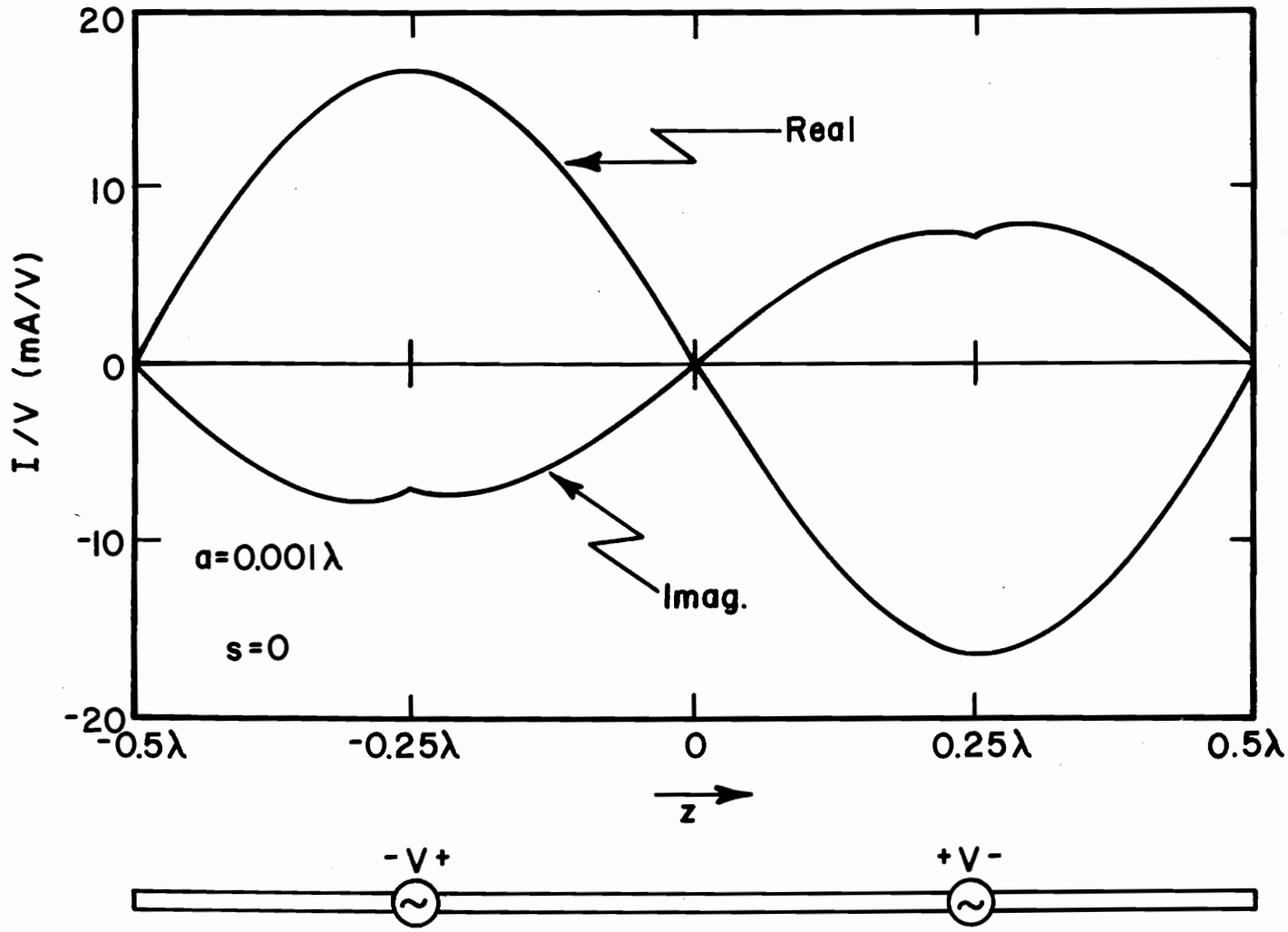

Figure 22. Current on Anti-Symmetrically Excited, One-Wavelength, Uniform Radius Antenna

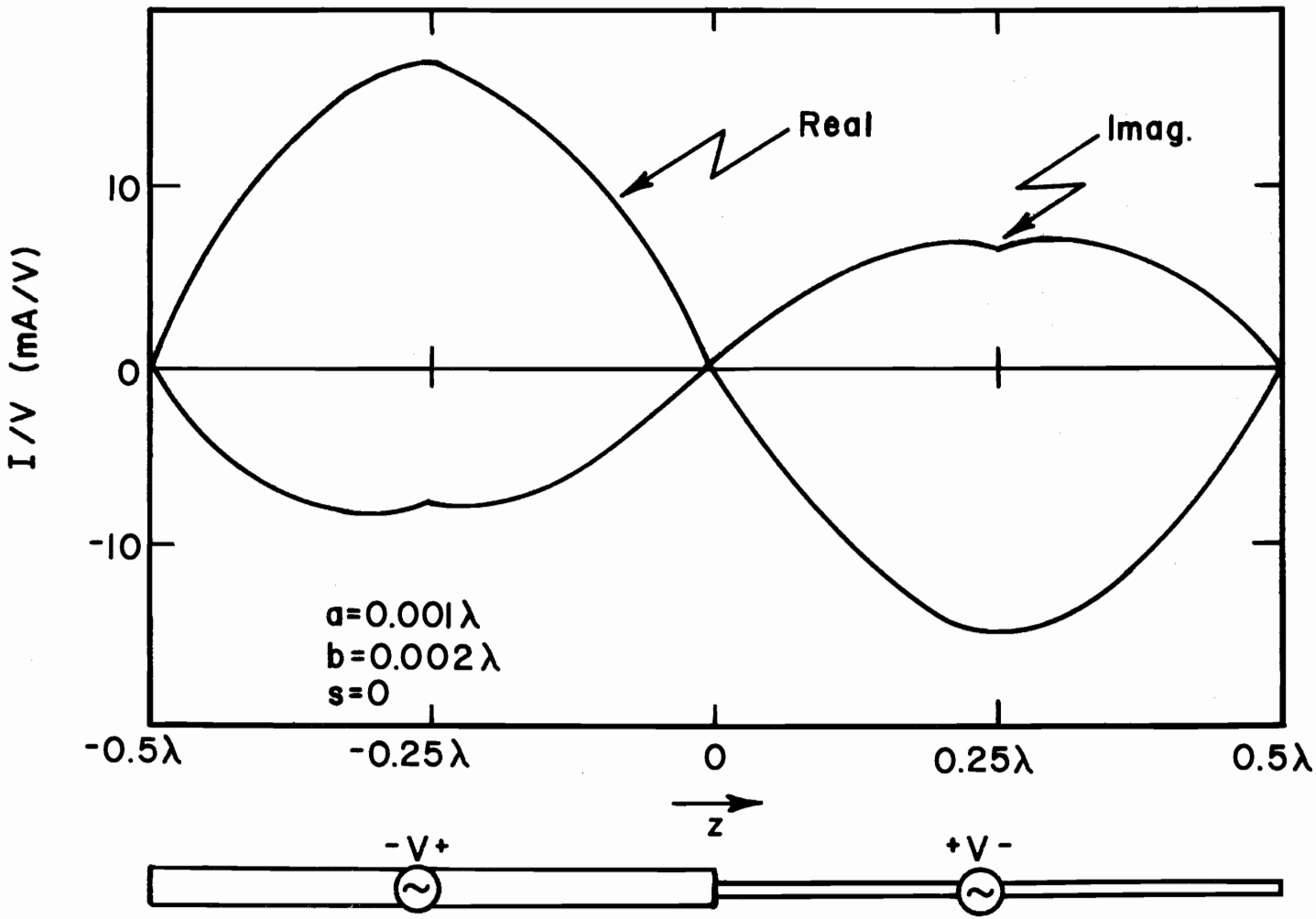

Figure 23. Current on Anti-Symmetrically Excited, One-Wavelength, Stepped-Radius Antenna

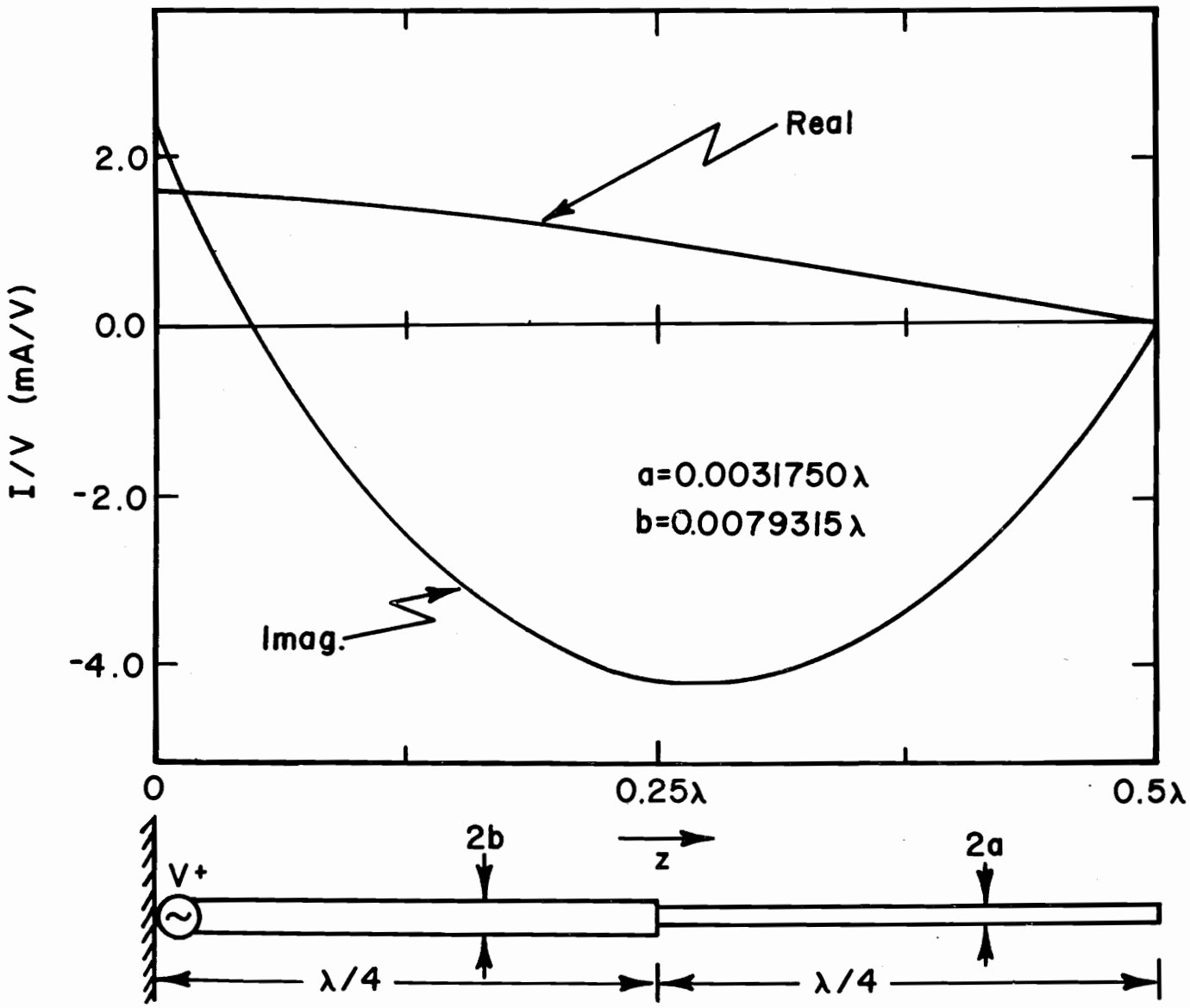

Figure 24. Current on Half-Wavelength Stepped-Radius Monopole above Ground

SECTION IV

AN ITERATIVE-SOLUTION ANALYSIS OF THE BENT-WIRE SCATTERER

1. INTRODUCTION

In this Section, a theory is developed by means by which one may determine the current induced on a bent-wire scatterer illuminated by a specified incident electromagnetic field $(\bar{E}^i, \bar{H}^i)$. The solution procedure is of the iterative type and, in general, follows the principles set forth in recent work by King and Wu [8,14]. However there is a significant difference in the iterative procedure applied to the bent-wire problem compared with that applied to either a straight wire or perpendicular crossed wires. This analysis is applied to the problem of a bent-wire scatterer in free space, as depicted in Fig. 25, as well as that of a bent-wire scatterer above an ideal ground plane (Fig. 26). Calculated results are presented for several cases of interest.

The straight wire elements of the bent-wire structure are treated as perfect conductors and the usual simplifications of thin-wire theory are employed in the analysis. Principally, the element radii are assumed to be very small compared with the wavelength λ, and the current density is considered to be essentially uniform around the periphery of an element.

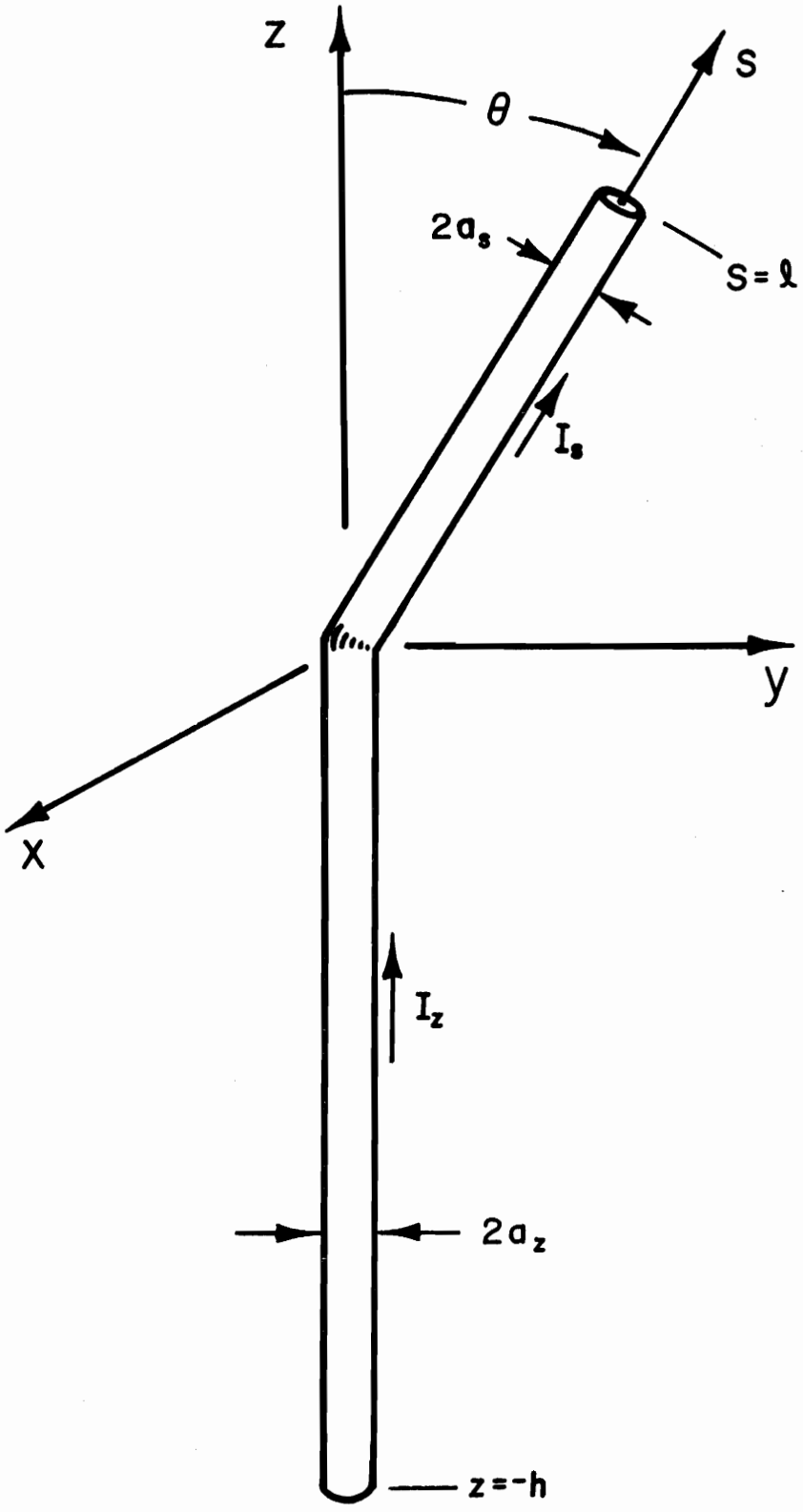

Figure 25. Bent Wire

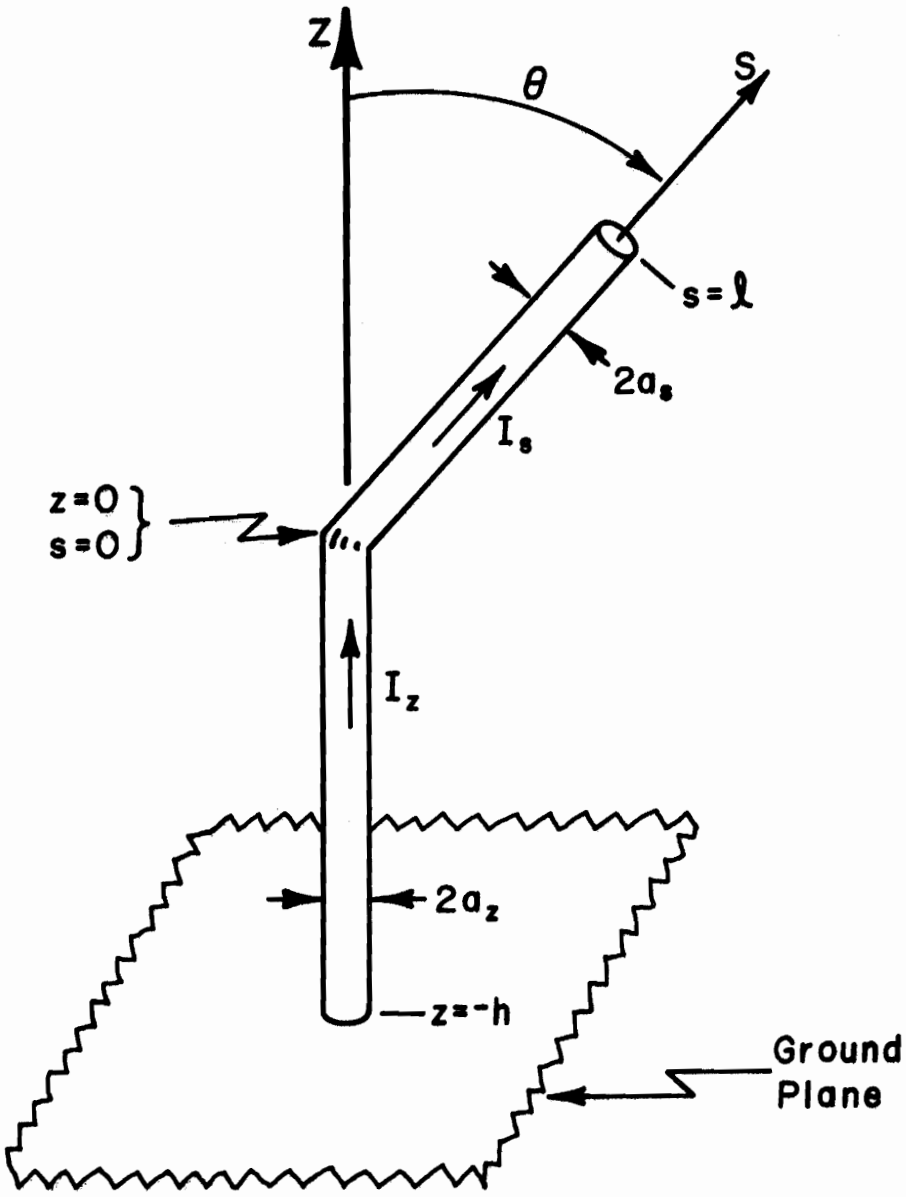

Figure 26. Bent Wire Above Ground

In the analytical solution procedure which follows, an expression, suitable for iteration, is derived for the total axial current on each element. In Fig. 25, one sees the bent wire located in a Cartesian coordinate system with the bend at the origin. One wire is coaxial with the z axis, and the other extends from the origin radially outward in the yz plane along a line which is declined from the z axis by an angle θ. The direction of the axis of the latter wire is designated the s direction. I_z is the total axial current on the z-directed wire, and I_s is that on the s-directed wire as shown in Fig. 25 which serves to define other geometric quantities of interest.

2. ANALYSIS

In the present analysis, expressions for I_z and I_s are formulated and are used to obtain zero and first order solutions by iteration. The above-mentioned expression for I_z is developed below from consideration of the magnetic vector potential $\bar{A}$ and the partial differential equation which this quantity satisfies.

Since the current on the bent wire is in the yz plane, one can readily show [5] that

$$\left[\frac{\partial^2}{\partial z^2} + k^2\right] A_z = j \frac{k^2}{\omega} E_z - \frac{\partial}{\partial z}\left(\frac{\partial}{\partial y} A_y\right) \tag{90}$$

where A_z and A_y are the z and y components of the vector

potential, E_z is the z component of the electric field resulting from currents induced on the scatterer, ω is the angular frequency of the suppressed harmonic variation in time, and k is $2\pi/\lambda$. Consider now that E_z, A_z, and A_y are evaluated on the surfaces of the z-directed wire in Fig. 25 along the line $(a_z,0,z)$ for $z\varepsilon(-h,0)$. In order to satisfy the boundary condition that total electric field tangential to, and evaluated on, the perfectly conducting wire surface, one requires $E_z(a_z,0,z)+E_z^i(a_z,0,z)=0$, $z\varepsilon(-h,0)$ where E_z^i is the z component of $\bar{E}^i$. Equation (90) is a well-known inhomogeneous differential equation, and one can demonstrate [5] that, on the z-directed wire,

$$A_z(a_z,0,z) = \frac{\mu}{4\pi}\left[C_z\cos kz + B_z\sin kz + V_z^i(z) + U_z(z)\right] \qquad (91)$$

where C_z and B_z are arbitrary constants of integration, where μ is the permeability of the medium, and where V_z^i and U_z are defined

$$V_z^i(z) = -j\frac{4\pi}{\eta}\int_{\zeta=0}^{z} E_z^i(a_z,0,\zeta)\sin k(z-\zeta)d\zeta \qquad (92a)$$

with η the intrinsic impedance of the medium and

$$U_z(z) = -\frac{4\pi}{\mu}\int_{\zeta=0}^{z}\left[\frac{\partial}{\partial y}A_y(a_z,y,\zeta)\right]_{y=0}\cdot\cos k(z-\zeta)d\zeta \qquad (92b)$$

The z-directed vector potential A_z in (91) is

$$A_z(a_z,0,z) = \frac{\mu}{4\pi} \int_{z'=-h}^{0} I_z(z')K(z-z',a_z)dz'$$

$$+ \cos\theta \frac{\mu}{4\pi} \int_{s'=0}^{\ell} I_s(s')G(z,s',a_z)ds' \qquad (93)$$

where

$$K(\xi,a) = \frac{e^{-jk[\xi^2+a^2]^{\frac{1}{2}}}}{[\xi^2+a^2]^{\frac{1}{2}}} \qquad (94a)$$

and

$$G(\xi,\xi',a) = \frac{e^{-jk[a^2 + \xi'^2\sin^2\theta +(\xi-\xi'\cos\theta)^2]^{\frac{1}{2}}}}{[a^2 + \xi'^2\sin^2\theta +(\xi-\xi'\cos\theta)^2]^{\frac{1}{2}}} \qquad (94b)$$

At a point in space (a_z,y,z), A_y is

$$A_y(x,y,z) = \frac{\mu}{4\pi} \sin\theta \int_{s'=0}^{\ell} I_s(s') \frac{e^{-jkR_y}}{R_y} ds' \qquad (95)$$

where

$$R_y = [a_z^2 + (y-s' \sin\theta)^2 + (z-s' \cos\theta)^2]^{\frac{1}{2}} \tag{96}$$

The derivative of A_y appearing in (92b) is seen to be

$$\frac{\partial}{\partial y} A_y(a_z,y,z)\Big|_{y=0} =$$

$$\frac{\mu}{4\pi} \sin^2\theta \int_{s'=0}^{\ell} s' I_s(s') \left\{ \left[\frac{1}{R_y^3} + j \frac{k}{R_y^2} \right] e^{-jkR_y} \right\}_{y=0} ds' \tag{97}$$

Hence, subject to interchange in order of integration in (97), U_z of (92b) becomes

$$-\sin^2\theta \int_{s'=0}^{\ell} s' I_s(s') \int_{\zeta=0}^{z} \left[\frac{1}{R_{\zeta s}^3} + j \frac{k}{R_{\zeta s}^2} \right] e^{-jkR_{\zeta s}} \cos k(z-\zeta) d\zeta ds' \tag{98}$$

with

$$R_{\zeta s} = \left[a_z^2 + s'^2 \sin^2\theta + (\zeta - s' \cos\theta)^2 \right]^{\frac{1}{2}} \tag{99}$$

The double integral of (98) can be reduced [15] to the single integral,

$$-\sin^2\theta \int_{s'=0}^{\ell} s' I_s(s') \left\{ \frac{e^{-jkR_{\zeta s}}}{R_{\zeta s}[a_z^2 + s'^2\sin^2\theta]} \left[(\zeta - s'\cos\theta)\cos k(z-\zeta) \right.\right.$$

$$\left.\left. -jR_{\zeta s}\sin k(z-\zeta) \right] \right\}_{\zeta=0}^{z} ds' \qquad (100)$$

which enables one to express U_z in the form of (101), which is

$$U_z(z) = -\sin^2\theta \int_{s'=0}^{\ell} I_s(s') \left(\frac{s'}{[a_z^2 + s'^2\sin^2\theta]} \right) \left\{ (z - s'\cos\theta)G(z,s',a_z) \right.$$

$$\left. + s'\cos\theta K(s',a_z)\cos kz + j\, e^{-jk[a_z^2 + s'^2]^{\frac{1}{2}}} \sin kz \right\} ds' \qquad (101)$$

computationally much more manageable than is (92b). At $z=0$, U_z is seen from (92b) to be zero and, for z less than zero by a few radii (a_z), the integrands of (101) are quite easy to integrate.

With the kernel K defined in (94a) partitioned into real and imaginary parts,

$$K(\xi,a) = K_r(\xi,a) + jK_i(\xi,a) \qquad (102)$$

where

$$K_r(\xi,a) = \frac{\cos k\sqrt{\xi^2 + a^2}}{\sqrt{\xi^2 + a^2}} \tag{103a}$$

and

$$K_i(\xi,a) = -\frac{\sin k\sqrt{\xi^2 + a^2}}{\sqrt{\xi^2 + a^2}} \tag{103b}$$

Equation (91) can be rearranged:

$$\int_{z'=-h}^{0} I_z(z')K_r(z-z',a_z)dz' = C_z\cos kz + B_z\sin kz + V_z^i(z) + U_z(z) + U_{zs}(z) + U_{zi}(z) \tag{104}$$

where

$$U_{zs}(z) = -\cos\theta \int_{s'=0}^{\ell} I_s(s')G(z,s',a_z)ds' \tag{105a}$$

and

$$U_{zi}(z) = -j \int_{z'=-h}^{0} I_z(z')K_i(z-z',a_z)dz' \tag{105b}$$

Now, without approximation, (104) yields

$$\Psi_z(z)I_z(z) = C_z\cos kz + B_z\sin kz + V_z^i(z)$$

$$+ U_z(z) + U_{zs}(z) + U_{zi}(z) \qquad (106)$$

subject to the definition,

$$\Psi_z(z) = \frac{1}{I_z(z)} \int_{z'=-h}^{0} I_z(z')K_r(z-z',a_z)dz' \qquad (107)$$

A procedure parallel to that leading to (104) for the z-directed wire can be applied to the s-directed wire to obtain

$$\Psi_s(s)I_s(s) = C_s\cos ks + B_s\sin ks + V_s^i(s) + U_s(s)$$

$$+ U_{sz}(s) + U_{si}(s) \qquad (108)$$

where C_s and B_s are arbitrary constants peculiar to the s-directed wire and where the remaining terms in (108) are defined below.

$$\Psi_s(s) = \frac{1}{I_s(s)} \int_{s'=0}^{\ell} I_s(s') K_r(s-s', a_s) ds' \tag{109a}$$

$$V_s^i(s) = -j \frac{4\pi}{\eta} \int_{\xi=0}^{s} E_s^i(a_s, 0, \xi) \sin k(s-\xi) d\xi \tag{109b}$$

$$U_{sz}(s) = -\cos\theta \int_{z'=-h}^{0} I_z(z') G(s, z', a_s) dz' \tag{109c}$$

$$U_{si}(s) = -j \int_{s'=0}^{\ell} I_s(s') K_i(s-s', a_s) ds' \tag{109d}$$

$$U_s(s) = -\sin^2\theta \int_{z'=-h}^{0} I_z(z') \left(\frac{z'}{[a_s^2 + z'^2 \sin^2\theta]} \right) \left\{ (s - z'\cos\theta) G(s, z', a_s) \right.$$

$$\left. + z'\cos\theta K(z', a_s) \cos ks + j e^{-jk[a_s^2 + z'^2]^{\frac{1}{2}}} \sin ks \right\} dz' \tag{109e}$$

a. Ψ-Functions

When $a<<\lambda$, which is true for thin wires, the real part of the kernel of (94a) is highly peaked for small ξ/λ and decays very rapidly for $\xi>>a$. These properties are evident from the approximations below:

$$K_r(\xi,a) = \frac{\cos k\sqrt{\xi^2 + a^2}}{\sqrt{\xi^2 + a^2}} = \frac{\cos 2\pi\sqrt{(\xi/\lambda)^2 + (a/\lambda)^2}}{\lambda\sqrt{(\xi/\lambda)^2 + (a/\lambda)^2}}$$

$$K_r(\xi,a) \doteq \frac{1}{\lambda\sqrt{(\xi/\lambda)^2 + (a/\lambda)^2}} - \frac{2}{\lambda}\pi^2\sqrt{(\xi/\lambda)^2 + (a/\lambda)^2} \quad ,$$

$$\xi/\lambda << 1 \text{ and } a/\lambda << 1 \qquad (110)$$

and

$$K_r(\xi,a) \doteq \frac{\cos k\xi}{\xi} \quad , \quad a/\lambda << 1 \text{ and } \xi >> a \qquad (111)$$

Due to the sharply peaked behavior of K_r near $\xi=0$ and the fast decay for $\xi>>a$, K_r exhibits the selecting property of a delta function. The Ψ-functions defined in (107) and (109a) may be represented by

$$\Psi(w) = \frac{1}{f(w)} \int_{w'=w_1}^{w_2} f(w') K_r(w-w', a)\, dw'$$

which, for $a \ll \lambda$, is reasonably well approximated by

$$\Psi(w) \doteq \int_{w'=w_1}^{w_2} \frac{1}{\sqrt{(w-w')^2 + a^2}}\, dw' \quad , \quad w \varepsilon (w_1, w_2)$$

$$\Psi(w) \doteq \ell n \left\{ \frac{(w-w_1) + \sqrt{(w-w_1)^2 + a^2}}{(w-w_2) + \sqrt{(w-w_2)^2 + a^2}} \right\} \tag{112}$$

The Ψ-function is almost constant for w remote, in terms of numbers of a, from end points w_1 and w_2 but varies quite rapidly within a few radii of either end; its value at w_1 and w_2 is approximately one-half its value at $(w_1+w_2)/2$ for $(w_2-w_1) \gg a$. One may obtain a good approximation of $\Psi'(w)$ at w_1 and w_2:

$$\Psi'(w) = \frac{1}{f(w)} \int_{w'=w_1}^{w_2} f(w') \frac{\partial}{\partial w} K_r(w-w',a)\,dw'$$

$$- \frac{f'(w)}{[f(w)]^2} \int_{w'=w_1}^{w_2} f(w') K_r(w-w',a)\,dw'$$

$$= \frac{1}{f(w)} \int_{w'=w_1}^{w_2} f(w') \frac{\partial}{\partial w} K_r(w-w',a)\,dw' - f'(w)\Psi(w)/f(w) \qquad (113)$$

At $w=w_1$, the first term in (113) can be well approximated by

$$- \frac{1}{f(w_1)} \int_{w'=w_1}^{w_2} f(w') \frac{(w_1-w')}{[(w_1-w')^2 + a^2]^{3/2}}\,dw'$$

$$\doteq - \int_{w'=w_1}^{w_2} \frac{(w_1-w')}{[(w_1-w')^2 + a^2]^{3/2}}\,dw'$$

which reduces to

$$\frac{1}{a} - \frac{1}{w_2-w_1} \qquad \text{at } w=w_1$$

and

$$-\frac{1}{a} + \frac{1}{w_2-w_1} \qquad \text{at } w=w_2$$

For reasonable values of $(w_2-w_1)>>a$ but not exceeding roughly 100, $\Psi(w)$ is not significantly greater than $2\,\ell n\,(\frac{2}{a})$. Hence, for $f'(w)$ typical of the derivative of current on a thin wire--not at a <u>free</u> end--the second term in (113) is very small compared with the first at w_1 or w_2, and one has a simple but good approximation of Ψ' at w_1 and w_2:

$$\Psi'(w_1) \doteq \frac{1}{a} \tag{114a}$$

$$\Psi'(w_2) \doteq -\frac{1}{a} \tag{114b}$$

It is worth noting that the value of Ψ or Ψ' at either w_1 or w_2 is highly sensitive to a but is insensitive to (w_2-w_1) so long as $(w_2-w_1)>>a$.

In view of the properties of the Ψ-function given above, $\Psi_z(z)$ and $\Psi_s(s)$ are seen to be almost constant except near the upper and lower ends of the individual wires. The values of Ψ_z and Ψ_s may be obtained from (112) with appropriate interpretation of w_1,w_2, and a, and the derivatives of these

Ψ-functions at the wire junction (bend) are, from (114),

$$\Psi_z'(0) = -\frac{1}{a_z} \tag{115a}$$

$$\Psi_s'(0) = \frac{1}{a_s} \tag{115b}$$

b. Outline of Iterative Procedure

The large value of the Ψ-functions for thin wires and the observation that some terms in (106) and (108) are far more significant than others suggest that these expressions may be amenable to an iterative solution procedure for determining I_z and I_s. In such a procedure, one identifies a so-called zero-order solution which comprises only terms that themselves are not direct functions of the currents.

The zero-order currents, I_z^o and I_s^o, from (106) and (108) are

$$I_z^o(z) = \frac{1}{\Psi_z}\left[C_z^o \cos kz + B_z^o \sin kz + V_z^i(z)\right] \tag{116a}$$

$$I_s^o(s) = \frac{1}{\Psi_s}\left[C_s^o \cos ks + B_s^o \sin ks + V_s^i(s)\right] \tag{116b}$$

where the Ψ-functions, defined in (107) and (109a), are approximated by (112). One observes that in (106) and (108) the U-functions, each of which depends upon current on the bent wire as is seen explicitly in (101), (105), and (109), are

ignored in the zero-order solutions. Expressions (116) are subjected to boundary conditons and the zero-order coefficients, C_z^o, B_z^o, C_s^o, and B_s^o, are thereby determined.

Finally, returning to (106) and (108) and using the zero-order currents as approximations to the exact currents in the integrands of the U-functions, one forces I_z and I_s to satisfy boundary conditions and thereby calculates C_z, B_z, C_s, and B_s. With these coefficients in (106) and (108), one has what are called first-order solutions for I_z and I_s.

In a procedure like that described above, the influence of the zero-order currents upon the first-order is proportional to the factor $1/\Psi$; hence, the importance of a large Ψ-function is clearly evident.

The boundary conditions which one enforces are (1) that the current vanish at the two free ends of the bent wire and (2) that both the current and its first derivative be continuous at the bend. In summary, these boundary conditions are

$$I_z(-h) = 0 \tag{117a}$$

$$I_s(\ell) = 0 \tag{117b}$$

$$I_z(0) = I_s(0) \tag{117c}$$

$$\left[\frac{d}{dz} I_z(z)\right]_{z=0} = I_z'(0) = \left[\frac{d}{ds} I_s(s)\right]_{s=0} = I_s'(0) \qquad (117d)$$

c. Current and its Derivative at the Bend

If the structure under study here were a straight wire (bent wire with $\theta=0^o$) or even the complex structure comprising two wires which cross at 90^o [8,14], it would be found that an iterative solution could be formulated in such a way that the Ψ-functions would be essentially constant even at the confluence of wires. However, in sharp contrast to analyses of the structures above, the iterative solution method for the bent wire must fully account for effects of the large derivative of the Ψ-functions at the bend. In addition, and of paramount bearing on the present analysis, one cannot relegate to a secondary role the contributions from one wire to the value of current on the other when the point of evaluation is at the bend--a point common to both wires. In other words, the determination of I_z and its derivative at $z=0$ cannot be made without cognizance of I_s at $s=0$. Hence, before the first order coefficients are calculated from boundary conditions (117), a thorough investigation of current and its derivative is in order.

From (106) $\Psi_z(0)I_z(0)$ is

$$\Psi_z(0)I_z(0) = C_z + U_{zs}(0) + U_{zi}(0) \qquad (118)$$

since $U_z(0)$ is seen from (92b) to be zero. Notice from (105a),

(94b), and (94a) that $U_{zs}(0)$ is

$$U_{zs}(0) = -\cos\theta \int_{s'=0}^{\ell} I_s(s')K(s',a_z)ds'$$

and, even though the integration above is over the s-directed wire, it reduces to

$$U_{zs}(0) = -\cos\theta\ \Psi_z(0)I_s(0) - j\ \cos\theta \int_{s'=0}^{\ell} I_s(s')K_i(s',a_z)ds' \quad (119)$$

Since $I_z(0)=I_s(0)$ as required by (117c), (119) and (118) yield

$$\Psi_z(0)[1 + \cos\theta]I_z(0) = C_z - j\ \cos\theta \int_{s'=0}^{\ell} I_s(s')K_i(s',a_z)ds'$$

$$-j \int_{z'=-h}^{0} I_z(z')K_i(z',a_z)dz' \quad (120)$$

By a similar procedure, one obtains the following for $\Psi_s(0)I_s(0)$:

$$\Psi_s(0)[1 + \cos\theta]I_s(0) = C_s - j\cos\theta \int_{z'=-h}^{0} I_z(z')K_i(z',a_s)dz'$$

$$-j \int_{s'=0}^{\ell} I_s(s')K_i(s',a_s)ds' \qquad (121)$$

Subject to the definitions of the constants,

$$P_z = -j\cos\theta \int_{s'=0}^{\ell} I_s(s')K_i(s',a_z)ds' + U_{zi}(0) \qquad (122a)$$

and

$$P_s = -j\cos\theta \int_{z'=-h}^{0} I_z(z')K_i(z',a_s)dz' + U_{si}(0) \quad , \qquad (122b)$$

which are clearly not zero-order contributors, (120) and (121) lead to

$$I_z(0) = \frac{C_z + P_z}{\Psi_z(0)[1 + \cos\theta]} \qquad (123a)$$

and

$$I_s(0) = \frac{C_s + P_s}{\Psi_s(0)[1 + \cos\theta]} \qquad (123b)$$

Next, in order that boundary condition (117d) may be enforced, it is necessary to investigate the derivatives of each term on the right-hand sides of (106) and (108). Only U_z and U_{zs} of (106) and U_s and U_{sz} of (108) require special attention; hence the derivative of $U_z(z)+U_{zs}(z)$ at $z=0$ is investigated in detail.

From the definition of $U_z(z)$ in (92b), the desired derivative of this function is seen to be

$$U_z'(0) = \left[\frac{d}{dz}\, U_z(z)\right]_{z=0} = -\frac{4\pi}{\mu}\left[\frac{\partial}{\partial y}\, A_y(a_z,y,0)\right]_{y=0}$$

or

$$U_z'(0) = -\sin\theta \int_{s'=0}^{\ell} I_s(s')\left\{\frac{\partial}{\partial y}\left(\frac{e^{-jkR_y}}{R_y}\right)\right\}_{\substack{y=0\\z=0}} ds'$$

Since

$$\left\{\frac{\partial}{\partial y}\left(\frac{e^{-jkR_y}}{R_y}\right)\right\}_{\substack{y=0\\z=0}} = -\sin\theta\left\{\frac{\partial}{\partial s'}\left(\frac{e^{-jkR_y}}{R_y}\right)\right\}_{\substack{y=0\\z=0}}$$

$$= -\sin\theta\ \frac{\partial}{\partial s'}\, K(s',a_z) \quad ,$$

$U_z'(0)$ becomes

$$U_z'(0) = \sin^2\theta \int_{s'=0}^{\ell} I_s(s') \frac{\partial}{\partial s'} K(s',a_z)ds' \quad . \tag{124}$$

At this point, attention is turned to the derivative of $U_{zs}(z)$, which can be written

$$U_{zs}'(0) = \left[\frac{d}{dz} U_{zs}(z)\right]_{z=0} = -\cos\theta \int_{s'=0}^{\ell} I_s(s') \left[\frac{\partial}{\partial z} G(z,s',a_z)\right]_{z=0} ds'$$

One can show that

$$\left[\frac{\partial}{\partial z} G(z,s',a_z)\right]_{z=0} = -\cos\theta \left[\frac{\partial}{\partial s'} G(z,s',a_z)\right]_{z=0}$$

which leads to

$$U_{zs}'(0) = \cos^2\theta \int_{s'=0}^{\ell} I_s(s') \frac{\partial}{\partial s'} G(0,s',a_z)ds'$$

Recognizing that $G(0,s',a_z)=K(s',a_z)$, one obtains

$$U_{zs}'(0) = \cos^2\theta \int_{s'=0}^{\ell} I_s(s') \frac{\partial}{\partial s'} K(s',a_z)ds' \tag{125}$$

Now, the sum of (124) and (125) is simply

$$U'_z(0) + U'_{zs}(0) = \int_{s'=0}^{\ell} I_s(s') \frac{\partial}{\partial s'} K(s', a_z) ds' \qquad (126)$$

The portion of the integrand of (126) involving K_r, the real part of K, can be integrated by parts and (126) can thereby be converted to

$$U'_z(0) + U'_{zs}(0) = I_s(\ell) \frac{\cos k\ell}{\ell} - I_s(0) \frac{\cos ka_z}{a_z}$$

$$- \int_{s'=0}^{\ell} \frac{d}{ds'} I_s(s') K_r(s', a_z) ds'$$

$$+ j \int_{s'=0}^{\ell} I_s(s') \frac{\partial}{\partial s'} K_i(s', a_z) ds'$$

in which the excellent approximation $K_r(\ell, a_z) \doteq \frac{\cos k\ell}{\ell}$ is utilized. Now, in view of the selecting property of the Ψ-function and since $\frac{\cos ka_z}{a_z} \doteq \frac{1}{a_z} \doteq -\Psi'_z(0)$ as indicated in (114), one arrives at

$$U'_z(0) + U'_{zs}(0) \doteq I_s(\ell)\,\frac{\cos k\ell}{\ell} + I_s(0)\Psi'_z(0) - I'_s(0)\Psi_z(0)$$

$$+j\int_{s'=0}^{\ell} I_s(s')\,\frac{\partial}{\partial s'}\,K_i(s',a_z)ds' \qquad (127)$$

With (127) available, the derivative of (106) is readily seen to be

$$\left[\frac{d}{dz}\left(\Psi_z(z)I_z(z)\right)\right]_{z=0} = \left[\Psi_z(z)I'_z(z) + \Psi'_z(z)I_z(z)\right]_{z=0}$$

or

$$\Psi_z(0)I'_z(0) + \Psi'_z(0)I_z(0) = kB_z + U'_z(0) + U'_{zs}(0) + U'_{zi}(0)$$

$$\doteq kB_z + I_s(\ell)\,\frac{\cos k\ell}{\ell} + I_s(0)\Psi'_z(0) - I'_s(0)\Psi_z(0)$$

$$+j\int_{s'=0}^{\ell} I_s(s')\,\frac{\partial}{\partial s'}\,K_i(s',a_z)ds' + j\int_{z'=-h}^{0} I_z(z')\,\frac{\partial}{\partial z'}\,K_i(z',a_z)dz' \qquad (128)$$

Since $I_s(0)=I_z(0)$ and $I'_s(0)=I'_z(0)$, the above reduces to

$$2\Psi_z(0)I_z'(0) = kB_z + I_s(\ell)\frac{\cos k\ell}{\ell} + W_z \tag{129}$$

where

$$W_z = j\int_{z'=-h}^{0} I_z(z')\frac{\partial}{\partial z'}K_i(z',a_z)dz' + j\int_{s'=0}^{\ell} I_s(s')\frac{\partial}{\partial s'}K_i(s'a_z)ds' \tag{130}$$

Similarly,

$$2\Psi_s(0)I_s'(0) = kB_s - I_z(-h)\frac{\cos kh}{h} + W_s \tag{131}$$

where

$$W_s = j\int_{z'=-h}^{0} I_z(z')\frac{\partial}{\partial z'}K_i(z',a_s)dz' + j\int_{s'=0}^{\ell} I_s(s')\frac{\partial}{\partial s'}K_i(s',a_s)ds' \tag{132}$$

From (123) the requirement that current be continuous at the bend (117c) is equivalent to the following relationship between C_s and C_z:

$$C_s = \frac{\Psi_s(0)}{\Psi_z(0)}\left[C_z + P_z\right] - P_s \tag{133}$$

Similarly, continuity of derivative (117d) requires

$$B_s = \frac{\Psi_s(0)}{\Psi_z(0)} \left[B_z + \frac{1}{k} I_s(\ell) \frac{\cos k\ell}{\ell} + \frac{1}{k} W_z \right]$$

$$+ \frac{1}{k} I_z(-h) \frac{\cos kh}{h} - \frac{1}{k} W_s \qquad (134)$$

Now the need to consider the derivative of the Ψ-functions is evident. If, for example, $\Psi_z'(0)$ were ignored, and, hence, did not exist on the left-hand side of (128), the term $I_s(0)\Psi_z'(0)$ on the right-hand side of (128) would have remained and would appear in (134). Similarly, a term involving $I_z(0)\Psi_s'(0)$ would appear in (134), and the two together would contribute a term proportional to

$$I_z(0) \left[\Psi_z'(0) - \Psi_s'(0) \right] = -I_z(0) \left[\frac{1}{a_z} + \frac{1}{a_s} \right] .$$

Clearly, a very large term like the above would incorrectly "uncouple" the coefficients B_z and B_s and would cause B_s to be prohibitively large in magnitude.

d. Zero-Order Currents

The zero-order coefficients are determined from the application of the boundary conditions (117) to Eqs. (116) which, since V_z^i, V_s^i, $\frac{d}{dz} V_z^i$, and $\frac{d}{ds} V_s^i$ are zero at the bend, results in

$$c_z^o \cos kh - B_z^o \sin kh = -V_z^i(-h) \qquad (135a)$$

$$C_s^o \cos k\ell + B_s^o \sin k\ell = -V_s^i(\ell) \tag{135b}$$

$$\frac{1}{\Psi_z} C_z^o = \frac{1}{\Psi_s} C_s^o \tag{135c}$$

$$\frac{1}{\Psi_z} B_z^o = \frac{1}{\Psi_s} B_s^o \tag{135d}$$

where the Ψ-functions are treated as constants calculated from the approximations (112) evaluated at the midpoint of the appropriate wire. Equations (135) can be solved for the zero-order coefficients:

$$C_z^o = - \frac{\frac{\Psi_z}{\Psi_s} V_s^i(\ell)\sin kh + V_z^i(-h)\sin k\ell}{\sin k(h+\ell)} \tag{136a}$$

$$B_z^o = - \frac{\frac{\Psi_z}{\Psi_s} V_s^i(\ell)\cos kh - V_z^i(-h)\cos k\ell}{\sin k(h+\ell)} \tag{136b}$$

where $(h+\ell) \neq n\lambda/2$, $n=1,2,\ldots,$. When C_z^o and B_z^o are determined, C_s^o and B_s^o follow from (135c) and (135d) or

$$C_s^o = \frac{\Psi_s}{\Psi_z} C_z^o \tag{136c}$$

$$B_s^o = \frac{\Psi_s}{\Psi_z} B_z^o \tag{136d}$$

Equation (135d) follows from boundary condition (117d) which equates the derivatives of the currents at the bend. In the computation of these derivatives for determination of the zero-order coefficients, the Ψ-functions are treated as constants even though this is clearly not the case near the bend. However, Eq. (135) is exact within thin-wire approximations and supports the treatment of Ψ as a constant even at the bend.

e. First-Order Currents

Returning to (106) and (108) and using I_z^o and I_s^o of the zero-order solution in the U-functions where I_z and I_s appear, respectively, one has first-order currents. These first-order solutions are improvements based upon the zero-order approximations. The first-order coefficients C_z, B_z, C_s, and B_s are determined from requiring (106) and (108) to satisfy the boundary conditions (117). To fully account for the fact that the Ψ-functions possess appreciable derivatives at the bend, the enforcement of (117c) and (117d) is achieved through (133) and (134). Equating $I_s(\ell)$ and $I_z(-h)$ of (106) and (108) to zero and eliminating C_s and B_s by means of (133) and (134), one finds that C_z and B_z satisfy

$$C_z \cos kh - B_z \sin kh = -F_z(-h) \tag{137a}$$

$$C_z \cos k\ell + B_z \sin k\ell = T \tag{137b}$$

where

$$T = \frac{\Psi_z(0)}{\Psi_s(0)} \left[P_s \cos k\ell + \frac{1}{k} W_s \sin k\ell - F_s(\ell) \right]$$

$$-P_z \cos k\ell - \frac{1}{k} \sin k\ell \qquad (138a)$$

$$F_z(z) = V_z^i(z) + U_z(z) + U_{zs}(z) + U_{zi}(z) \qquad (138b)$$

$$F_s(s) = V_s^i(s) + U_s(s) + U_{sz}(s) + U_{si}(s) \qquad (138c)$$

The solutions of (137) are

$$C_z = \frac{-F_z(-h) \sin k\ell + T \sin kh}{\sin k(h+\ell)} \qquad (139a)$$

$$B_z = \frac{T \cos kh + F_z(-h) \cos k\ell}{\sin k(h+\ell)} \qquad (139b)$$

Knowing C_z and B_z from (139) and, subsequently, C_s and B_s from (133) and (134), one can calculate I_z and I_s from (106) and (108).

3. ZERO-ORDER CURRENTS FOR BENT-WIRE SCATTERER ABOVE GROUND PLANE

The currents I_z and I_s on the bent-wire scatterer above a ground plane, depicted in Fig. 26, can be calculated in a way similar to that described in IV-(1d). The single difference is that the boundary condition (117a) is replaced by

$$I_z'(-h) = 0 \tag{140}$$

Subject to (140) and (117b)-(117d), the coefficients C_z^o and B_z^o for the zero-order currents on the structure of Fig. 26 are found to be

$$C_z^o = \frac{-\frac{\Psi_z}{\Psi_s} V_s^i(\ell) \cos kh + \frac{1}{k} V_z^{i'}(-h) \sin k\ell}{\cos k(h+\ell)} \tag{141a}$$

$$B_z^o = \frac{-\frac{1}{k} V_z^{i'}(-h) \cos k\ell + \frac{\Psi_z}{\Psi_s} V_s^i(\ell) \sin kh}{\cos k(h+\ell)} \tag{141b}$$

The coefficients C_s^o and B_s^o follow from (141) in (136) and, with the four coefficients known, one may calculate the zero-order currents for the bent wire above a ground plane from (116).

4. RESULTS

a. Bent Wire in Free Space

Shown in Fig. 27 are curves of zero-order current on the bent wire of Fig. 25 for various values of bend angle θ. The radii are equal as are the lengths of the two wires ($a_z=a_s=0.001\lambda$, $\ell=h=\lambda/8$). The plane-wave incident field is z-directed, the direction of propagation is parallel to the x axis, and the magnitude of the incident electric field is adjusted so that $E_z^i\lambda=1$ volt. In Fig. 28 is displayed current calculated for the same structure and illumination by means of an accurate numerical technique. Attention is called to the good agreement even though the data of Fig. 27 are only zero-order solutions.

b. Bent-Wire above a Ground Plane

In Figs. 29 and 30 are shown zero-order current distributions on the bent-wire scatterer of Fig. 26. The radii and lengths are equal ($a_z=a_s=0.00635\lambda$ and $\ell=h=\lambda/2$), and the incident field is that described above. Numerical technique solutions for the current on this scatterer are provided in Fig. 31, where again one observes very good agreement. The flatness of the current for $\theta=60^o$ is remarkable as is its sensitivity to small changes in θ about 60^o (Figs. 30 and 31). Notice also in Figs. 30 and 31, for the $\theta=90^o$ case, that the top-loading element (s-directed wire) bears very little current--zero zero-order current (Fig. 29)--and, hence, is an ineffective top load.

The zero-order solutions presented here are good approximations to actual currents and such would be true for numerous cases. However, the goodness of the zero-order solution is highly dependent upon wire lengths. One should not expect the zero-order results for the bent wire in free space to be acceptable for $\ell+h$ fairly near odd multiples of $\lambda/2$ or near odd multiples of $\lambda/4$ in the case of the bent wire above ground. Of course, the first-order solutions should provide accurate results except at odd multiples of $\lambda/2$ in the free space case and at odd multiples of $\lambda/4$ for the structure above ground.

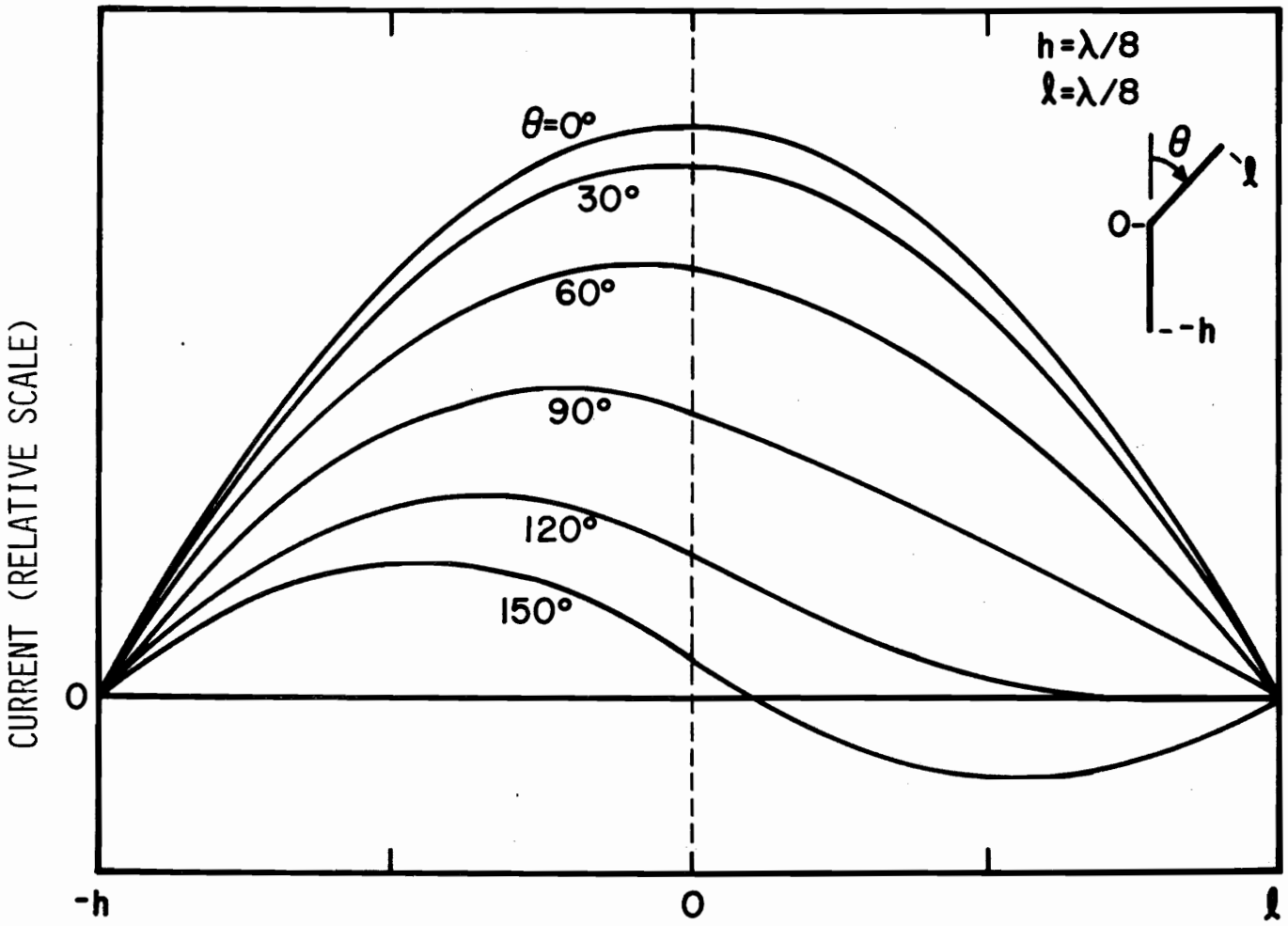

Figure 27. Zero-Order Current on Bent-Wire Scatterer Illuminated by Normally Incident Plane Wave

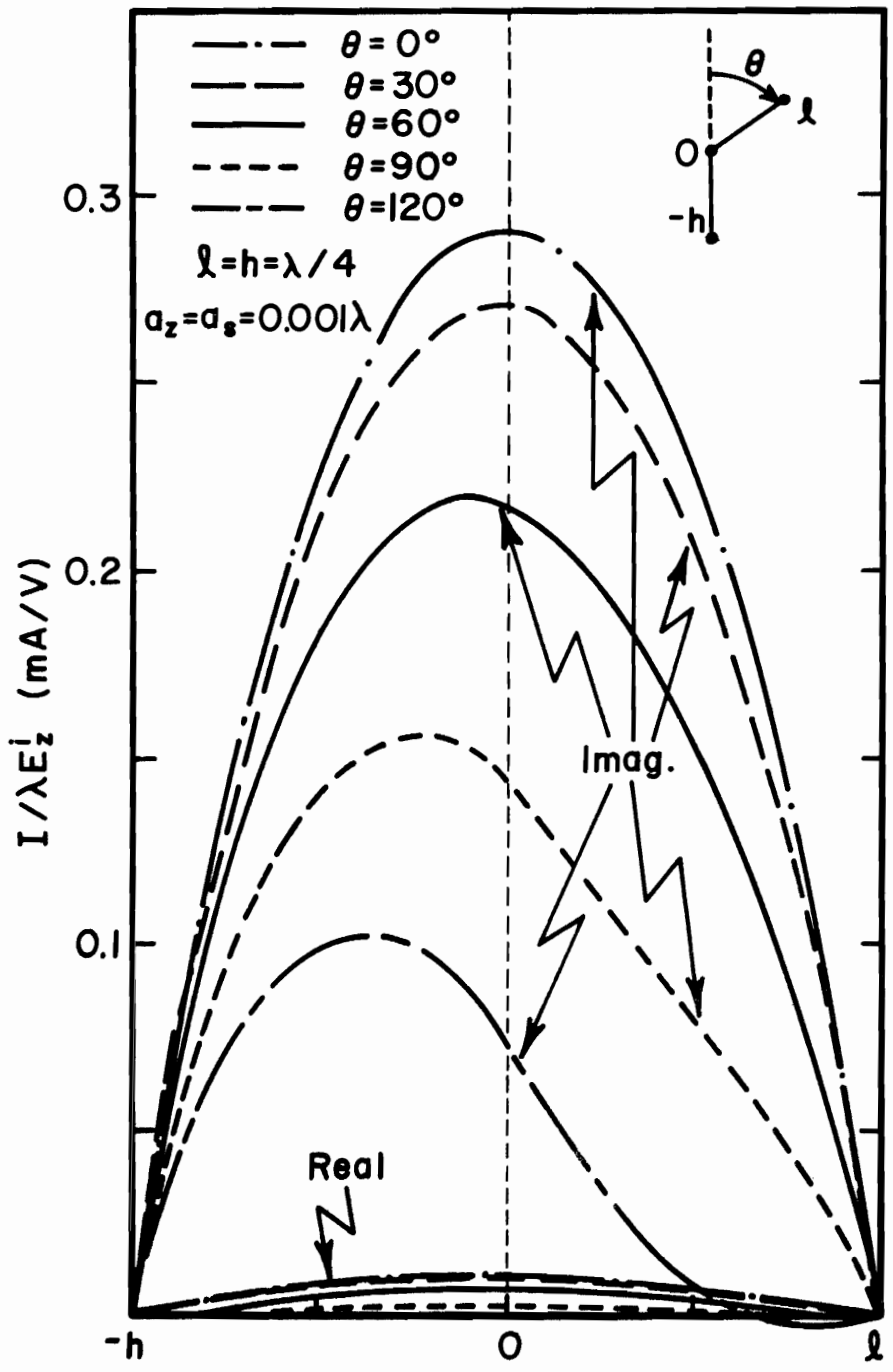

Figure 28. Current on Bent-Wire Scatterer Illuminated by Normally Incident Plane Wave

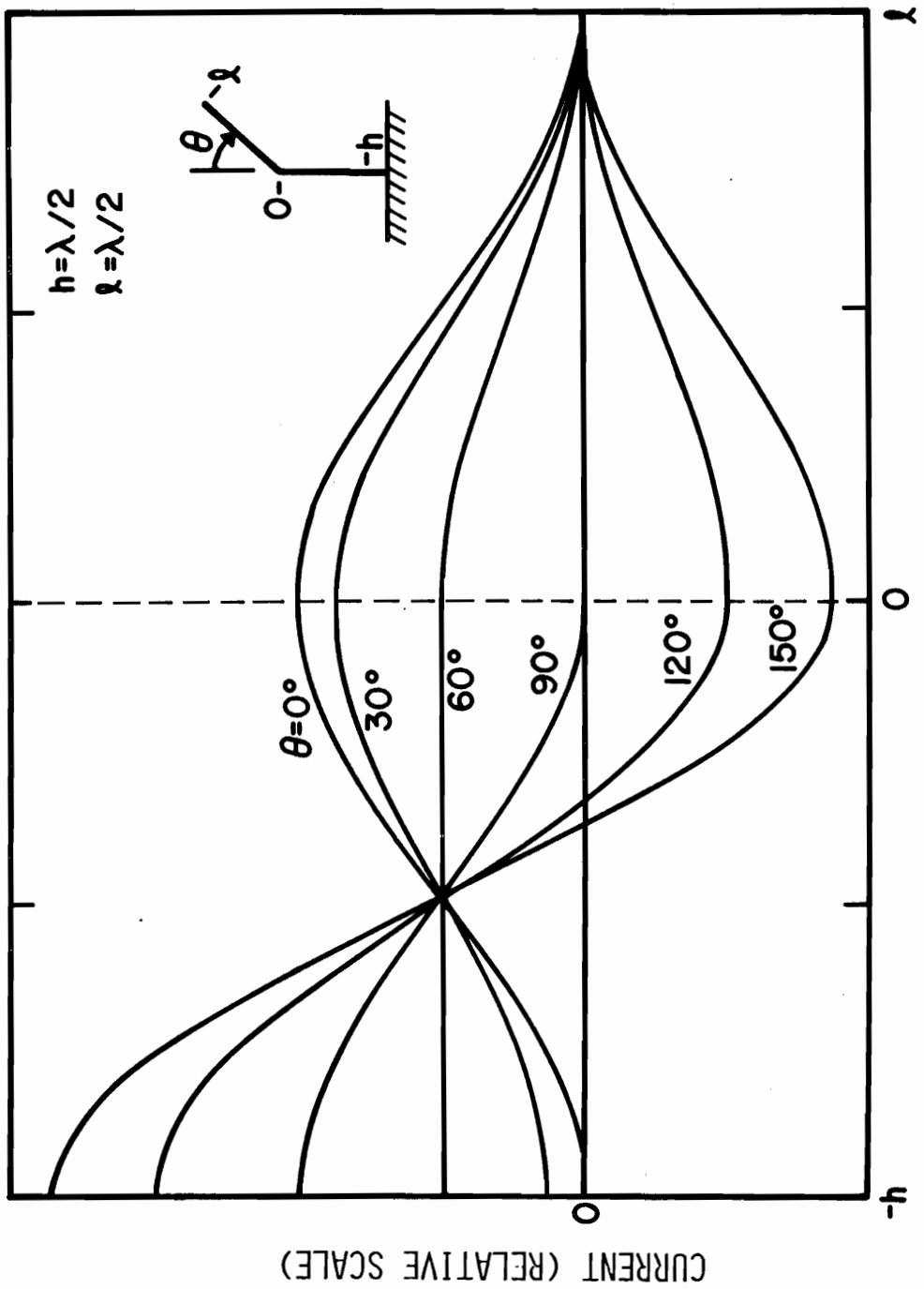

Figure 29. Zero-Order Current on Bent-Wire Scatterer above Ground Plane Illuminated by Normally Incident Plane Wave

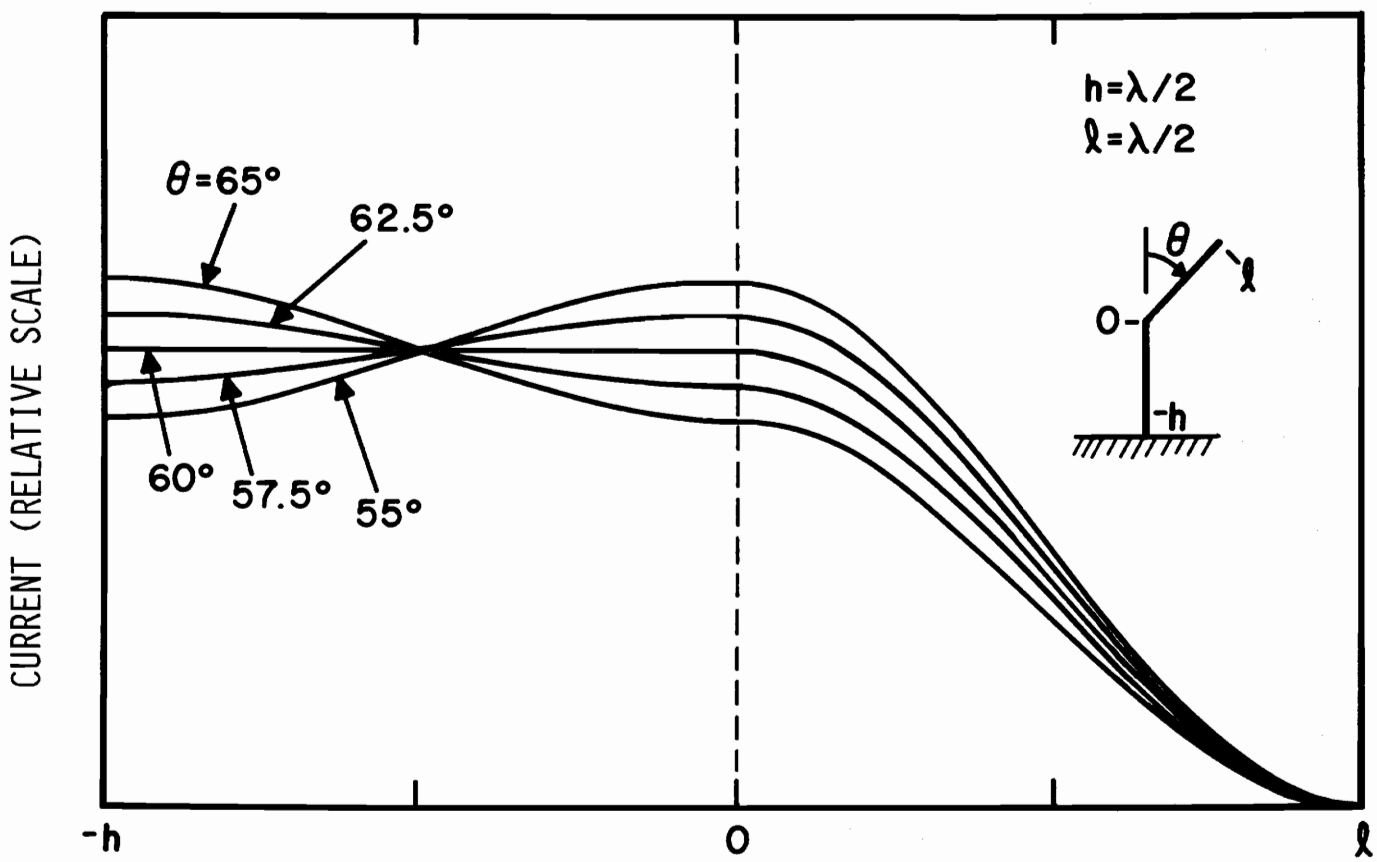

Figure 30. Zero-Order Current on Bent-Wire Above Ground for Small Bend Angles about $\theta = 60^{o}$

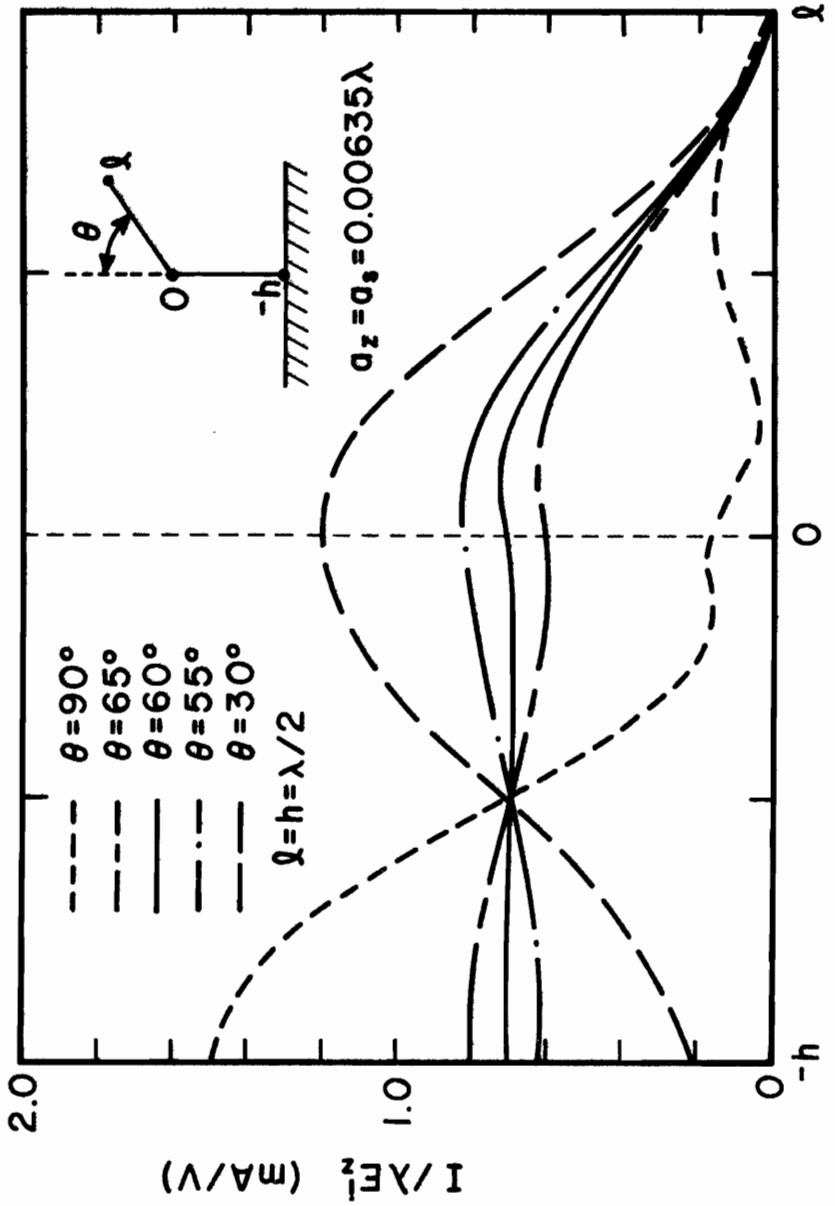

Figure 31. Current on Bent-Wire Scatterer above Ground Plane Illuminated by Normally Incident Plane Wave

SECTION V

MEASUREMENT FACILITIES AND APPARATUS

The experimental measurements reported here consist of current and charge distributions on thin wire structures. The first set of measurements were made on scattering elements, the second on a driven antenna. Both types of structure utilize an image plane geometry, since this geometry allows complete separation of the test structure and the instrumentation. The facilities and apparatus used for the measurements are described in this Section.

The frequency at which the measurements were made was determined by three factors: (1) the size of the image plane, (2) the requirement that the test structures be compatible with thin wire theory, and (3) the physical size of probes and associated apparatus which could be accurately constructed.

Requirements 2 and 3 above indicated that a frequency range from 300MHz to 600MHz was desirable. However, the then existing 12 ft. x 13 ft. image plane was too small for measurements in this frequency range and an enlargement of this facility was necessary.

An 18 ft. x 28 ft. image plane was constructed by extending the original plane to the fullest extent possible

in the antenna laboratory building. The new portion was constructed of 4 ft. x 12 ft. x 0.032 in. aluminum sheets cemented to 5/8 in. thick particle board backing. The joints between the aluminum sheets are backed by aluminum strips and 10/32 flat head aluminum bolts are counter sunk along the edges at a spacing of about 6 in. The joints and bolt heads are covered with 0.002 in. thick silver backed tape. The final structure deviates from a plane by less than 0.02λ overall at 600MHz and less than 0.007λ over short distances at the same frequency. Mounting for the test antennas is provided at a point 8.2 ft. from the lower edge and 10 ft. from one side. A cross sectional view of the antenna laboratory showing the position of the image plane is provided in Fig. 32. Panels of 24 in. high pyramidal absorber can be placed around the image plane to reduce reflections.

b. Instrumentation

The technique used for measurement of current and charge distributions was basically the same as that used by many researchers (see for example Mack [16]). Charge density was measured by a very short monopole perpendicular to the surface of the test structure. The accuracy to which the response of this probe corresponds to charge density depends primarily on the constancy of the normal component of electric field over the length of the probe. Errors may therefore be expected very near changes in the surface of the test structure such

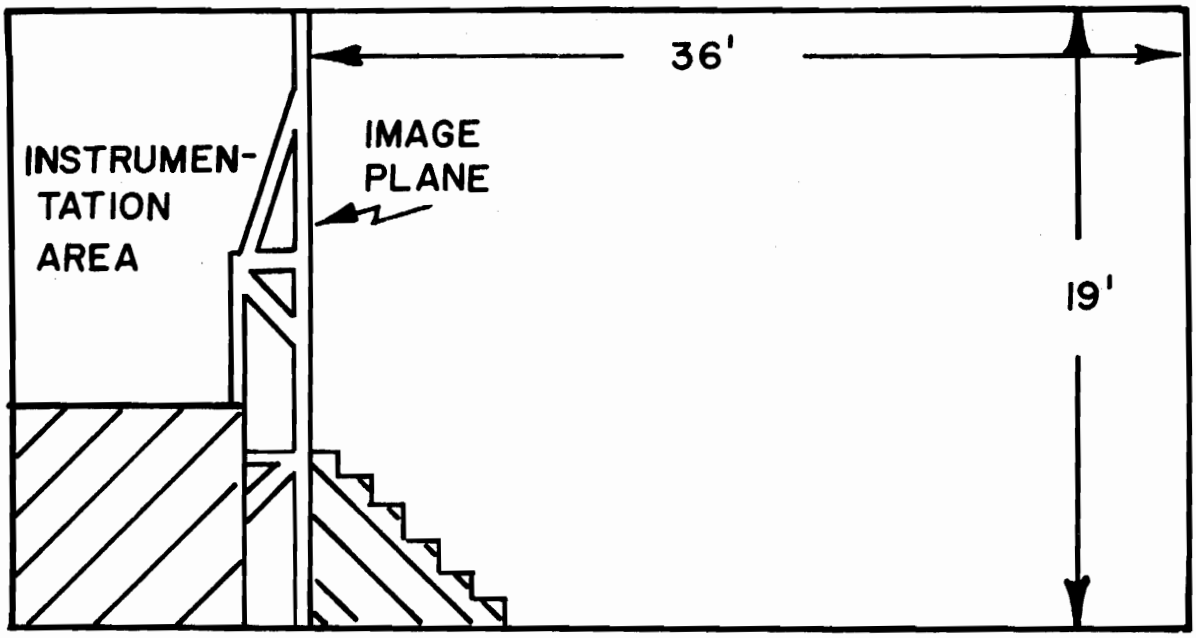

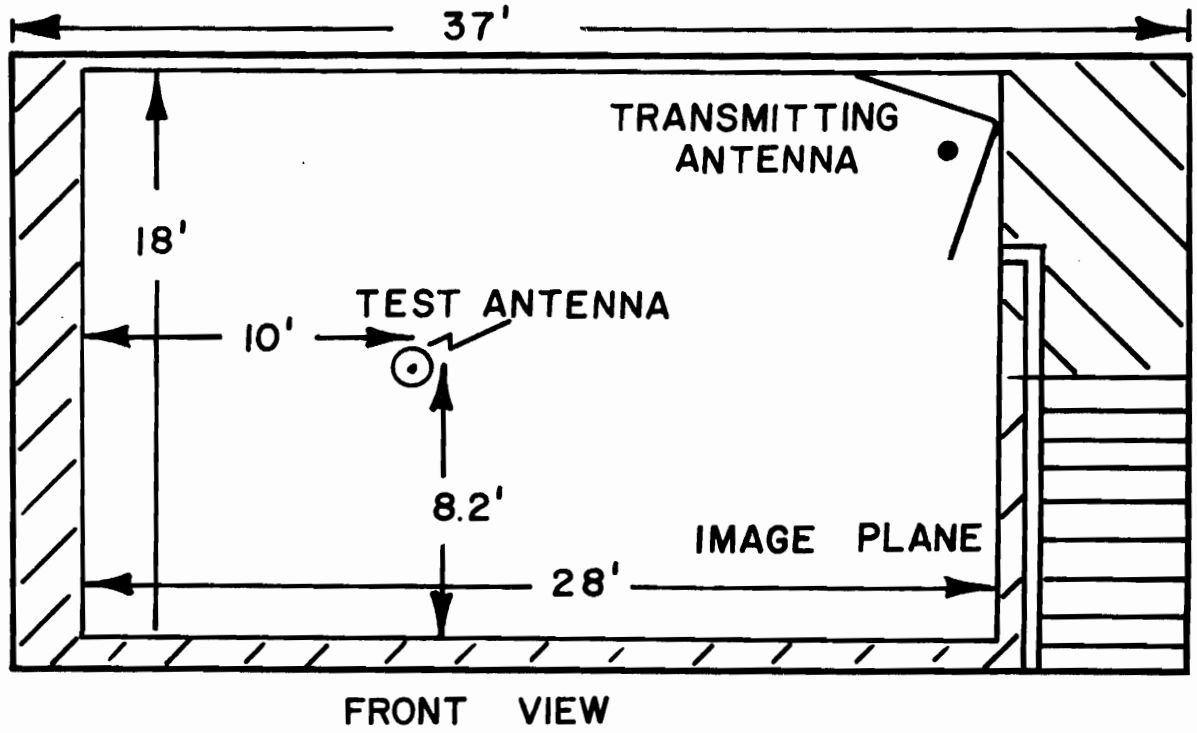

Figure 32. Antenna Laboratory and Image Plane

as bends, junctions, or ends of the tubular structures. The current distributions were measured by a small, center-loaded, image plane loop. The probe is mounted with its plane in an axial plane of the tubular antenna. The loop thus responds to the H_ϕ component of magnetic field. The accuracy to which the response of this probe corresponds to current density depends on several factors. Since the electric field is essentially perpendicular to the surface, the amount of electric field, or dipole mode, response which is added to the magnetic field response, is dependent on the accuracy to which the load is centered at the top of the loop. This location of the load, however, cannot discriminate against response to tangential components of electric field and, hence, errors similar to those of the charge probe may be expected near changes in the surface of the test structure. Finally, the finite size of the loop results in errors at points where the current is changing rapidly with distance along the surface, or where the tangential magnetic field changes rapidly in a direction perpendicular to the surface. Probes of the type used here have been analyzed by Whiteside [17]. The design of the probes and probe carriages are shown in Fig. 33.

The test structures, both scatterers and driven antennas, were constructed of cylindrical brass tubing. A slot 1/16 in. wide was cut axially in this tubing to allow movement of the probes along the structure. The probe carriage was designed to slide inside of the tubes and extend through the slot to the surface of the tube. The charge probe was constructed

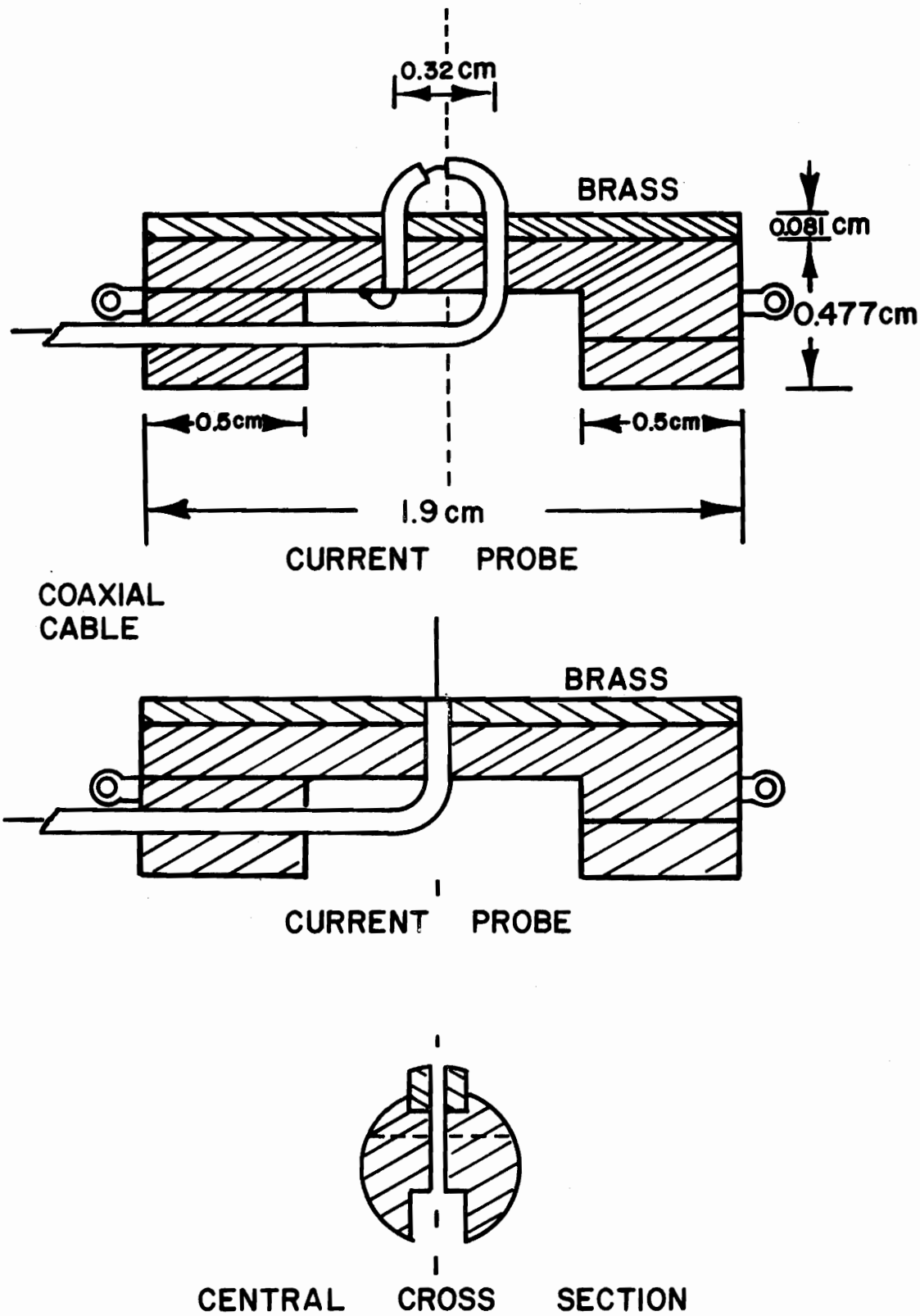

Figure 33. Probe and Probe Carriage

on the probe carriage from 0.034" O.D. semi-rigid coaxial cable. The outer conductor of the cable is soldered to the probe carriage and cut at the surface. The inner conductor continues beyond the surface to form the monopole antenna. The current probe was constructed from 0.02 in. semi-rigid coaxial cable. The cable was first formed into a semi circle, and then the center conductor was removed for a distance of about 0.020 in. starting from a point exactly at the top of the loop. The cable on one side of the loop is short circuited, the other side is joined to the signal cable. The load for the loop antenna is thus the input impedance of the coaxial cable.

Signals from the probes are carried by coaxial cables passing inside of the tubular test structures to the measuring instruments located behind the image plane. A block diagram of the system is shown in Fig. 34. Preliminary to actual measurements, the entire system including probes was tested in a coaxial line having a slotted tubular inner conductor. The commerical instruments used in the system are listed below:

Power Source - General Radio Model 1209 B Oscillator
Hughes Model 1401 H ----- Amplifier
Boonton Model 230 A ----- Amplifier

Measurement - Hewlett Packard Model 8405A Vector Voltmeter
Hewlett Packard Model 5345A Counter

Recording, Processing and Plotting of Data- Hewlett Packard Model 9820 Calculator with Model 9862A Plotter

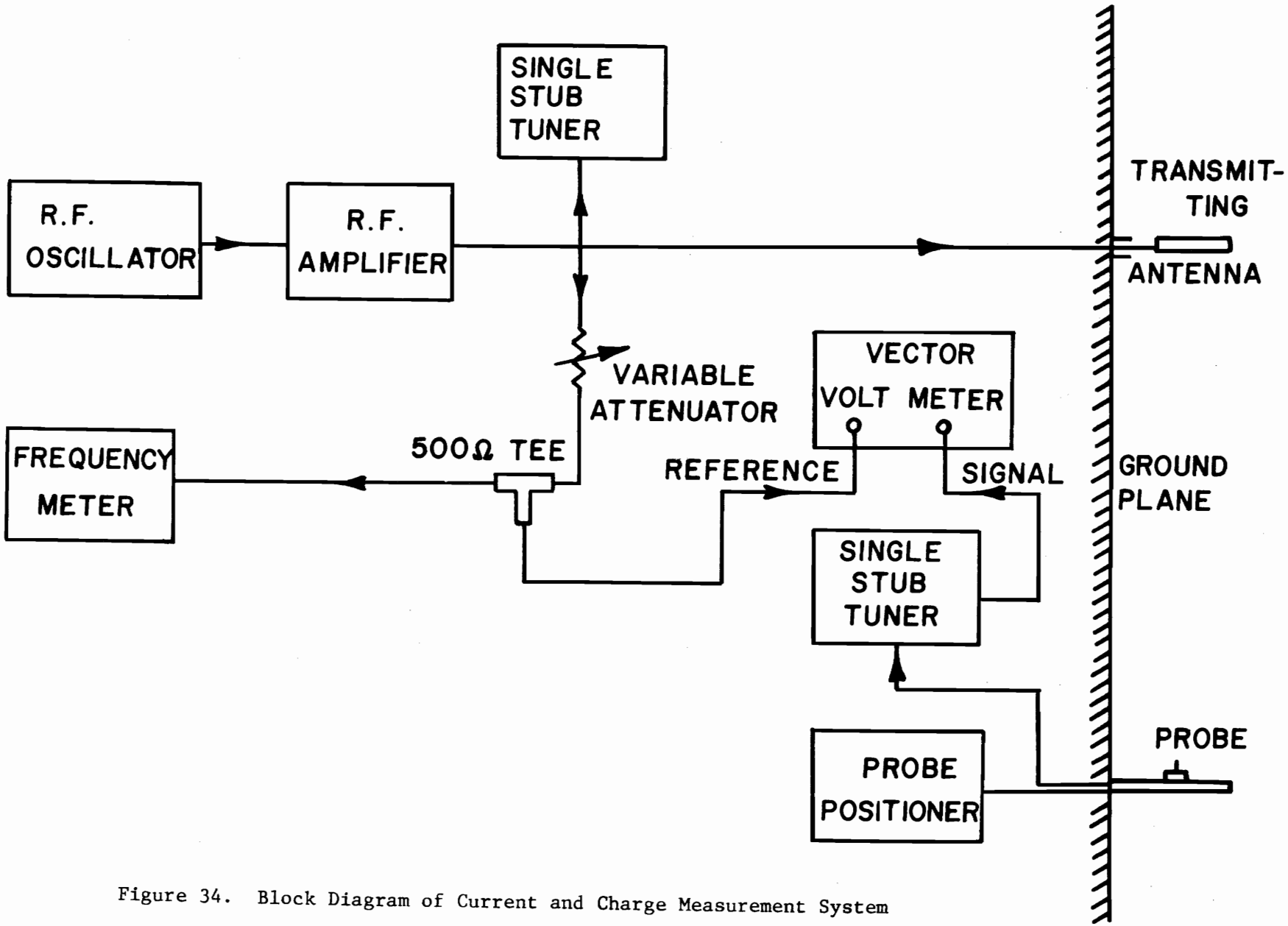

Figure 34. Block Diagram of Current and Charge Measurement System

The primary purpose of this measurement program is to obtain data for comparison with theoretical solutions of wire models (idealized) of aircraft. In the cases of the scattering measurements, it is therefore very desirable for the illumination to correspond as near as possible to that of a plane wave. For the structures studied here, this requirement reduces to having the component of electric field, which lies in the plane of the scatterer, perpendicular to the image plane and constant in both magnitude and phase over the area of the scatterer. In the actual experimental system the transmitting antenna was only 12 wavelengths away from the test structure at 600MHz. The spherical wave front produced by a short dipole at this distance creates a 15^{o} phase change along a 1 wavelength long scatterer. Calculations show that a collinear array formed by mounting a one-wavelength element above the image plane and driving it at its center should produce a phase deviation of only 5^{o} over a one wavelength long test scatterer. The transmitting antenna actually used consisted of this collinear type element mounted in a 90^{o} corner reflector. In addition to the direct wavefront of the transmitting antenna, additional distortion of the illuminating field may be caused by reflections from the edges of the image plane and surrounding objects. As a test of the illuminating field two monopole scatterers were measured, one of length $h = \lambda$ and the other of length $h = 1.5\lambda$. The

comparison of the current and charge distributions measured with theoretical results of Burton and King [18] are shown in Fig. 35. The agreement is seen to be reasonably good for the h = λ case, but significant deviation is seen for h = 1.5λ. This may be taken as evidence of near plane wave illumination to a distance of one wavelength from the image plane. For scattering elements greater than one wavelength long, errors due to non-plane wave illumination may be expected.

Two types of scatterers were measured, the bent wire and V cross shown in Fig. 36. Each of the structures was constructed from brass tubing 0.25 in. in diameter with a wall thickness of 1/32 in. The bends and junctions were formed by soldering the tubes together with a miter joint. Since the current and charge distributions were measured at all points except near the joints, it was necessary to design a system to control the probe position past the joints as shown in Fig. 37. A small Teflon pulley was mounted inside of the tube at the end. A pre-stretched and treated nylon dial cord was attached to each end of the probe, the portion attached to the forward end of the probe passed around the pulley and back through the tube to a control mechanism behind the ground plane. The coaxial cable carrying the signal from the probe was a 0.023 in. O.D. semi-rigid cable capable of bending around the joint inside of the tube. Initially, a small Teflon piece was inserted at the bend to protect the coaxial cable. Later it was found that a small build-up of solder at this

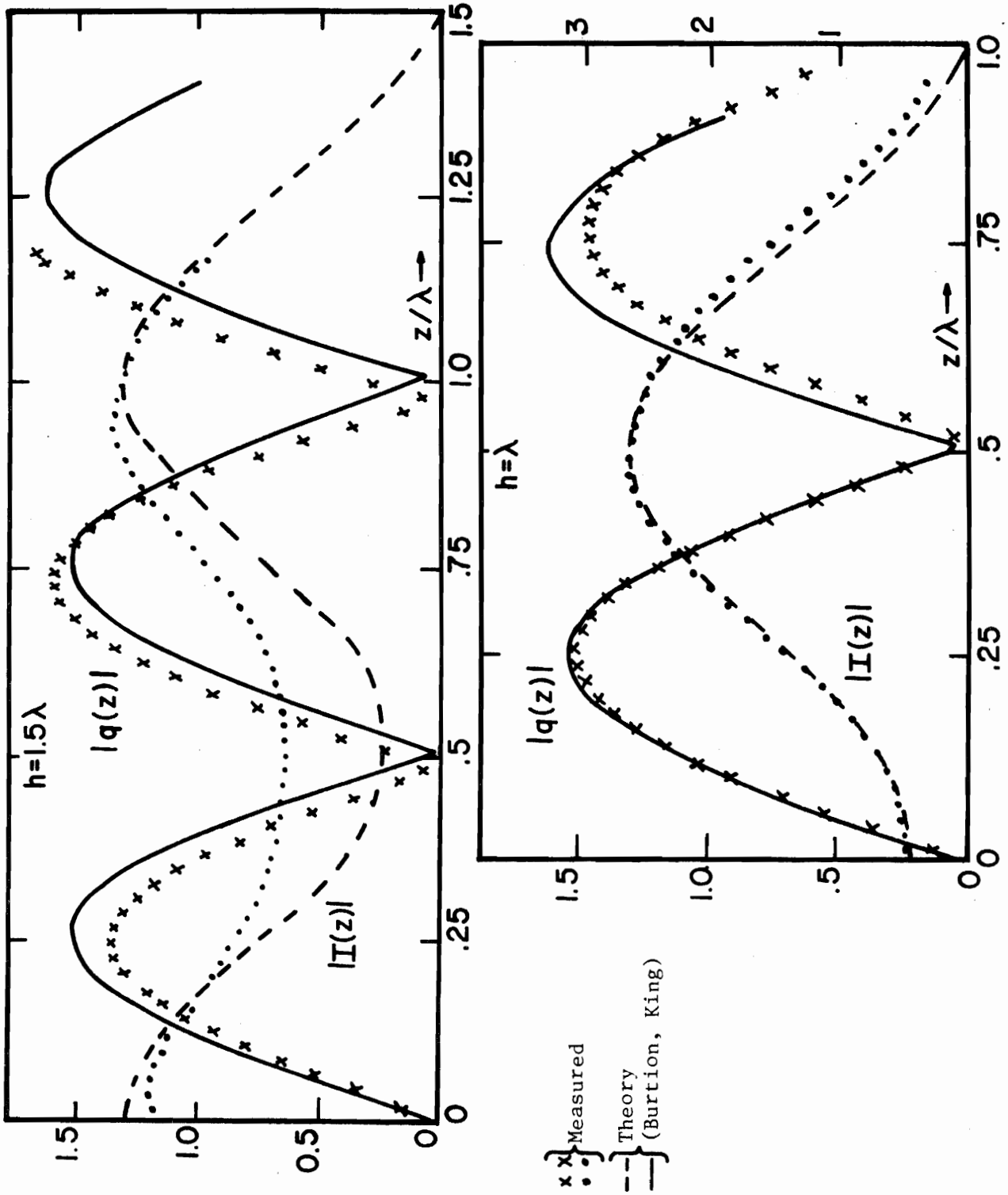

Figure 35. Current and Charge on Straight Scatterers, h=λ, h= 1.5λ Theoretical and Experimental Data

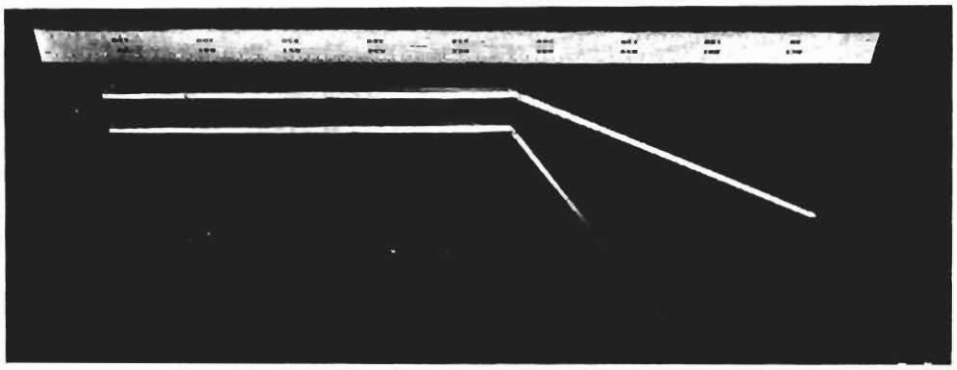

a. Bent Wire - $\theta = 30^{o}$ and $\theta = 62^{o}$

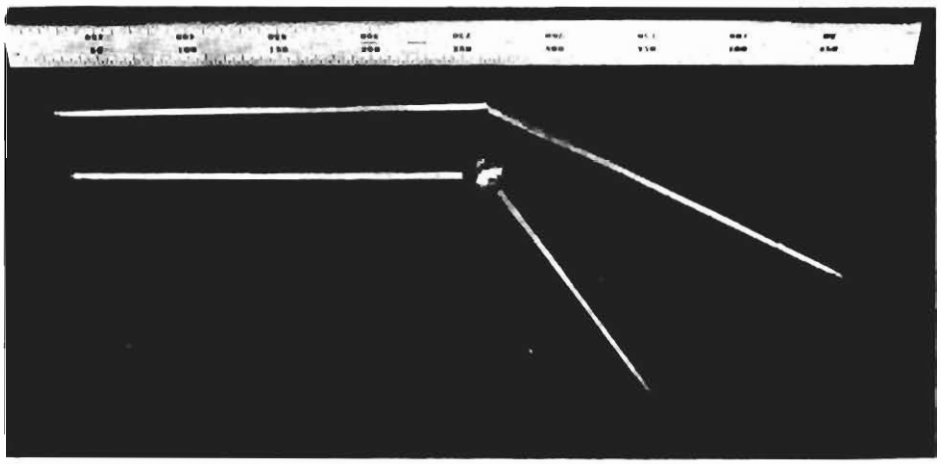

b. Bent Wire - With Sphere at Junction

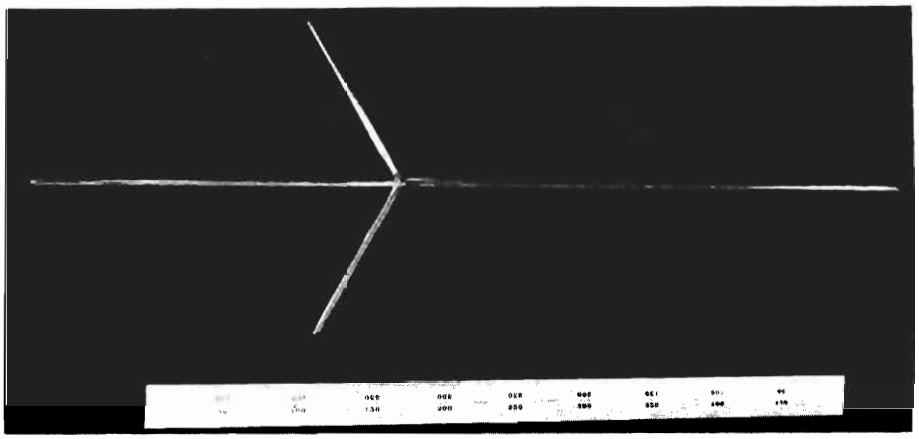

c. V Cross

Figure 36. Bent Wire and V Cross Scatterers

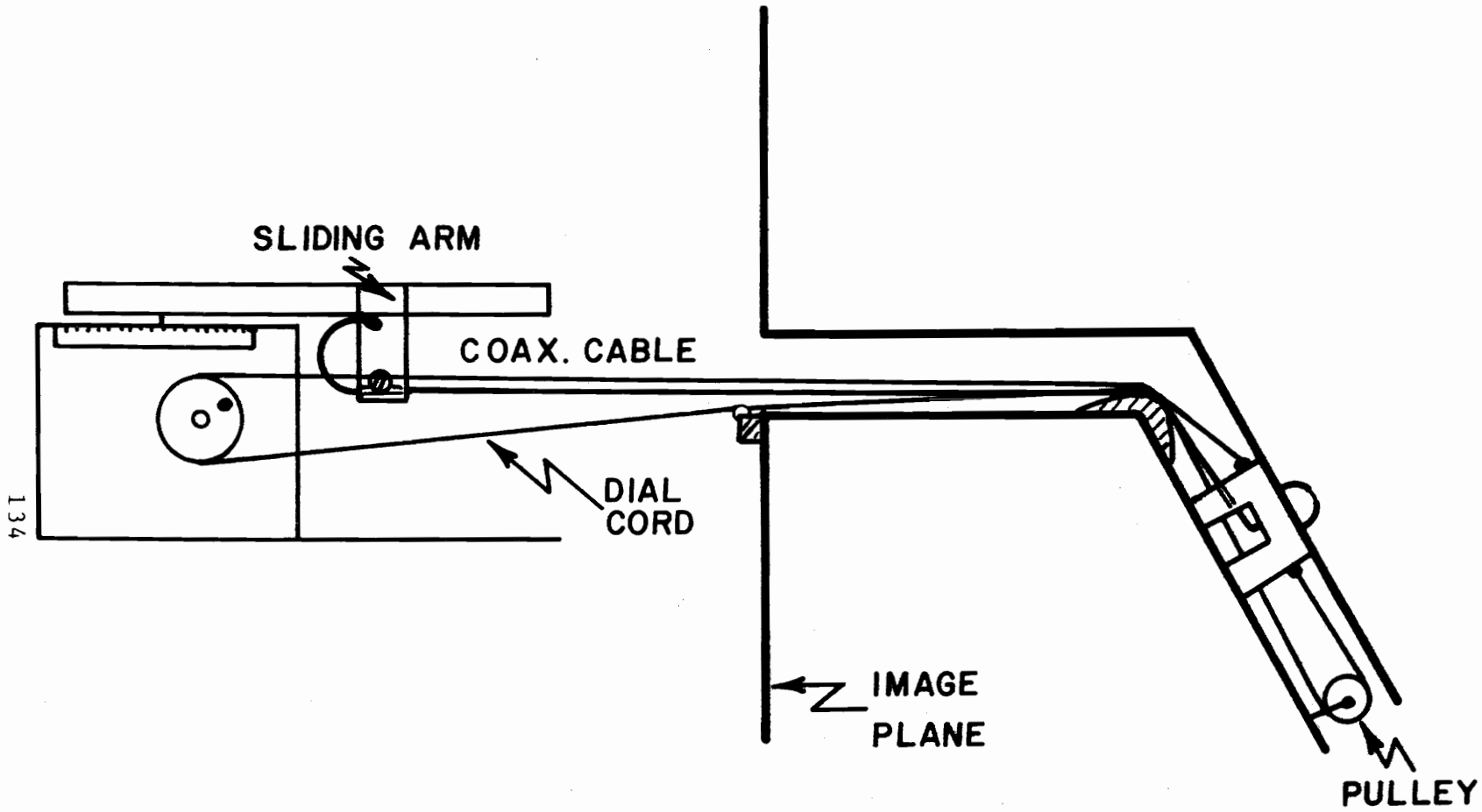

Figure 37. Probe Positioning Mechanism

point provided satisfactory protection for the cable. The probe carriage could not pass through the junction; therefore it was necessary to insert the probe from the image plane end and measure up to the junction. The probe was then removed and inserted in the outer end of the antenna, cables and control lines being inserted through the slot, after which measurements were made from the end back toward the junction. This measurement procedure was somewhat time consuming and it was necessary to insure that the system remained constant during each set of measurements. Although frequency drifts were observed, they were less than 4 parts in 10^5.

Measurements of the current and charge distributions were made on a thin cylindrical monopole antenna containing a step in radius. The ratio of radii of the two parts of the antenna was originally intended to be about 2 to 1. The diameter of the smaller portion was restricted by probe size to be at least 0.25 in., thus the larger portion was required to be at least 0.5 in. in diameter. Availability of materials governed the final choice of 0.625 in. for the larger diameter and 0.25 in. for the smaller diameter. In order for the larger radius to be compatible with thin-wire theory, it was necessary to make measurements at a frequency of 300MHz. Scattering measurements were not considered to be reliable at this frequency with the image plane size available. A coaxially driven monopole was therefore used for these measurements.

The construction details of the coaxial line antenna system are shown in Fig. 38. Current and charge measurements were desired along both sides of the step in radius. For correlation of the data, it is essential that the same probe system be used throughout. The larger-radius portion of the antenna was therefore placed at the image plane so that the probe could be withdrawn from this portion and inserted into the smaller-radius tube from behind the image plane. The 0.625 in. tube forms both the larger-radius part of the monopole and the inner conductor of the coaxial line. The tube is slotted axially over its entire length. Measurements can, therefore, be made inside of the coaxial line for determination of antenna apparent impedance and normalization factors needed for determination of absolute values of current and charge on the antenna. The 0.25 in. diameter tube is mounted coaxially through the larger tube and extends beyond it a distance of 25 cm. to form the smaller-radius portion of the antenna. Provisions were made for adding unslotted sections of 0.25 in tube to extend the length of the smaller-radius portion of the antenna. The outer conductor of the coaxial line has an inside diameter of 1.020 in., and the space between the two conductors is filled with a high density styrofoam, $\varepsilon_r = 1.12$. The characteristic impedance of this line is, therefore, 27.8 ohms. The coaxial line has an overall length of 1 meter (1λ at 300MHz) and is short circuited at the end opposite the antenna. Signal is applied to the

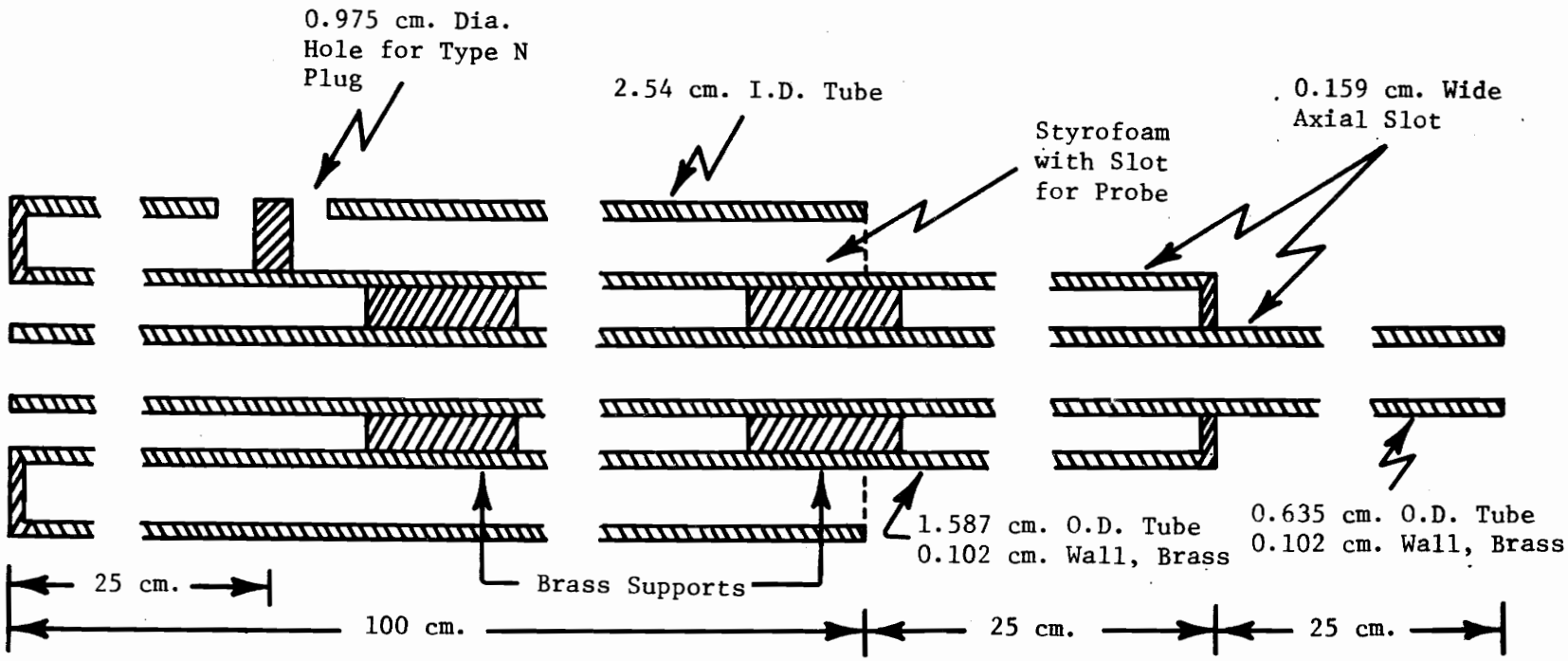

Figure 38. Stepped-Radius Coaxial-Line/Antenna System Diagram

line by a T connection at a distance of 25 cm. from the short circuit. The system before and after assembly is shown in Fig. 39.

The probes used for these antenna measurements are identical to those described in the previous section. The probe carriage differs however, since only straight line movement of the probe is necessary. A 0.125 in. diameter brass tube is attached to the rear of the probe carriage and extends beyond the rear of the coaxial line. A pointer attached to this tube provides for measurement of probe location. The 0.020 in O.D. semi-rigid coaxial line from the probe passes through this 0.125 in. diameter tube.

The instrumentation for the antenna system was the same as that shown for the scatterer measurements.

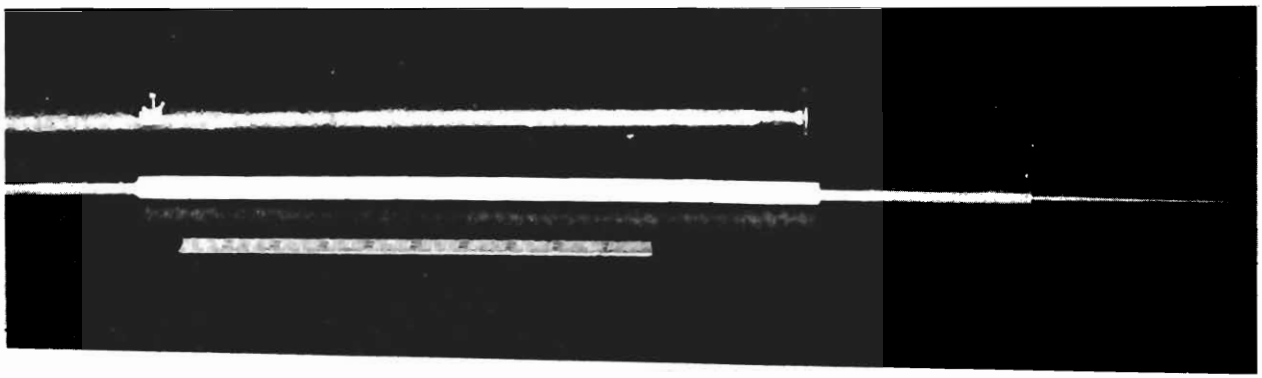

a. Before Assembly

b. After Assembly

Figure 39. Stepped-Radius System

SECTION VI

EXPERIMENTAL MEASUREMENTS--STEPPED-RADIUS

The apparatus described in Section V was used to obtain current and charge distributions on a thin stepped-radius monopole. The measured data is presented in this Section. For interpretation of the data the calibration and normalization factors which were used are of considerable importance and these will be discussed first.

The coaxial line/antenna system provides for continuous movement of the probes into the coaxial line portion. Measurements within the coaxial line make possible an absolute calibration of the probe measurement relative to the voltage across the line at the image plane.

A calibration factor, N_q, for the charge probe is determined to satisfy the equation.

$$N_q Q_m(z) = q(z) \text{ coulombs/meter-volt} \qquad (142)$$

where $Q_m(z)$ is the meter reading of the charge probe signal, and $q(z)$ is the linear density of charge on the antenna. Within the coaxial line the charge density is related to the voltage by

$$q(z) = V(z)C_o \qquad (143)$$

where

$$C_o = \frac{\varepsilon_o \varepsilon_r 2\pi}{\ell n(b_2/b_1)} \text{ farads/meter} \tag{144}$$

is the capacitance per length of the coaxial line. The most convenient location for determining q(z) is z = $-\lambda/2$ where

$$V(-\lambda/2) = V(0)e^{j\pi} \tag{145}$$

From Eqs. (142) and (143) we then have

$$N_q = \frac{e^{j\pi} C_0}{Q_m(-\lambda/2)} \tag{146}$$

where V(0) = 1 volt has been assumed. The capacitance of the coaxial line in this system is $C_o = 1.272 \times 10^{-10}$ farad/meter. The calibration factor was applied to all measurements on the antenna.

The calibration factor N_I for the current probe measurements was obtained in a manner similar to N_q. At any point within the line

$$I(z) = V(z)Y(z) \tag{147}$$

The most convenient point for computing N_I is z=$-\lambda/4$, where $y(-\lambda/4) = z(0)$, and

$$N_I = \frac{V(-\lambda/4)Z(0)}{I_m(-\lambda/4)(Z_c)^2} \tag{148}$$

where $I_m(-\lambda/4)$ is the meter reading of the current probe signal. The voltage $V(-\lambda/4)$ may be related to $V(0)$ by

$$V(-\lambda/4) = \frac{Z_c}{Z(0)} V(0) e^{j\pi/2} \tag{149}$$

where Z_c is the characteristic impedance of the coaxial line. Combining 148 and 149

$$N_I = \frac{e^{j\pi/2}}{I_m(-\lambda/4)Z_c} \tag{150}$$

where $V(0) = 1$ volt is assumed. The calibration factor determined by eq. 150 depends only on knowledge of Z_c. The factor could be computed from measurements at any point within the line, but knowledge of the antenna impedance would then be necessary. The disadvantage of eq. 150 is that when the antenna impedance is high, as occurs for one of the test antennas, the measurement of I_m must be made near a current minimum.

The probe calibration factors discussed above provide for absolute normalization of measurements on that portion of the antenna which is a smooth continuation of the coaxial line. Measurements on the smaller radius portion of the antenna require additional correction factor. If it were assumed that the probes respond to the fields at the surface of the antenna, the signal from the probes would then be

proportional to the surface density of current or charge. The calibration factors N_I and N_q convert the measurements to total current and linear density of charge respectively. Hence, the assumption that a probe signal is proportional to surface density leads to a correction factor which is simply the ratio of the two radii, a/b_1. Unfortunately, the situation is not this simple. The probes being of finite dimensions respond to fields away from the surface of the antenna, and this must be considered in the correction factor.

The charge probe, being a very short monopole, responds to the integral of the E_r over its length. At points along the antenna which are not too near the step or end, the E_r field varies 1/r near the surface of the antenna. Hence, the charge probe response is proportional to

$$\int_R^{R+h} \frac{1}{r}\, dr = \ell n[(R + h)/R] \tag{151}$$

where R = b, or a, the radius of the antenna, and h = the length of the charge probe. The correction factor, M_q, to be applied to measurements of charge on the small radius portion of the antenna is therefore

$$M_q = \ell n\left(\frac{a+h}{a}\right) / \ell n\left(\frac{b+h}{b}\right) \tag{152}$$

For the two radii used $M_q = 0.469$ with a probe height h = 0.1 in.

The correction factor M_I for the current probe is obtained in a similar manner. The probe response in this case is proportional to the integral of H_ϕ over the area of the loop probe. As for E_r we may assume that H_ϕ varies as 1/r near the surface of the antenna except near the step and end. Thus the signal from the probe is proportional to

$$F = \iint_A \frac{1}{r}\, ds \tag{153}$$

For evaluation of this integral the coordinate system of Fig. 40 is used and eq. 153 becomes

$$F = 2 \int_{y=R}^{R+h} \frac{1}{y} \int_{x=0}^{\sqrt{h^2-(y-a)^2}} dx\,dy \tag{154}$$

Integrating with respect to x and introducing the change of variable, y = z + R, we obtain

$$F = 2 \int_{z=0}^{h} \frac{1}{Z+R} \sqrt{h^2 + z^2}\; dz \tag{155}$$

Expanding the factor 1/(z+R) in a power series, and integrating term by term a series solution is obtained.

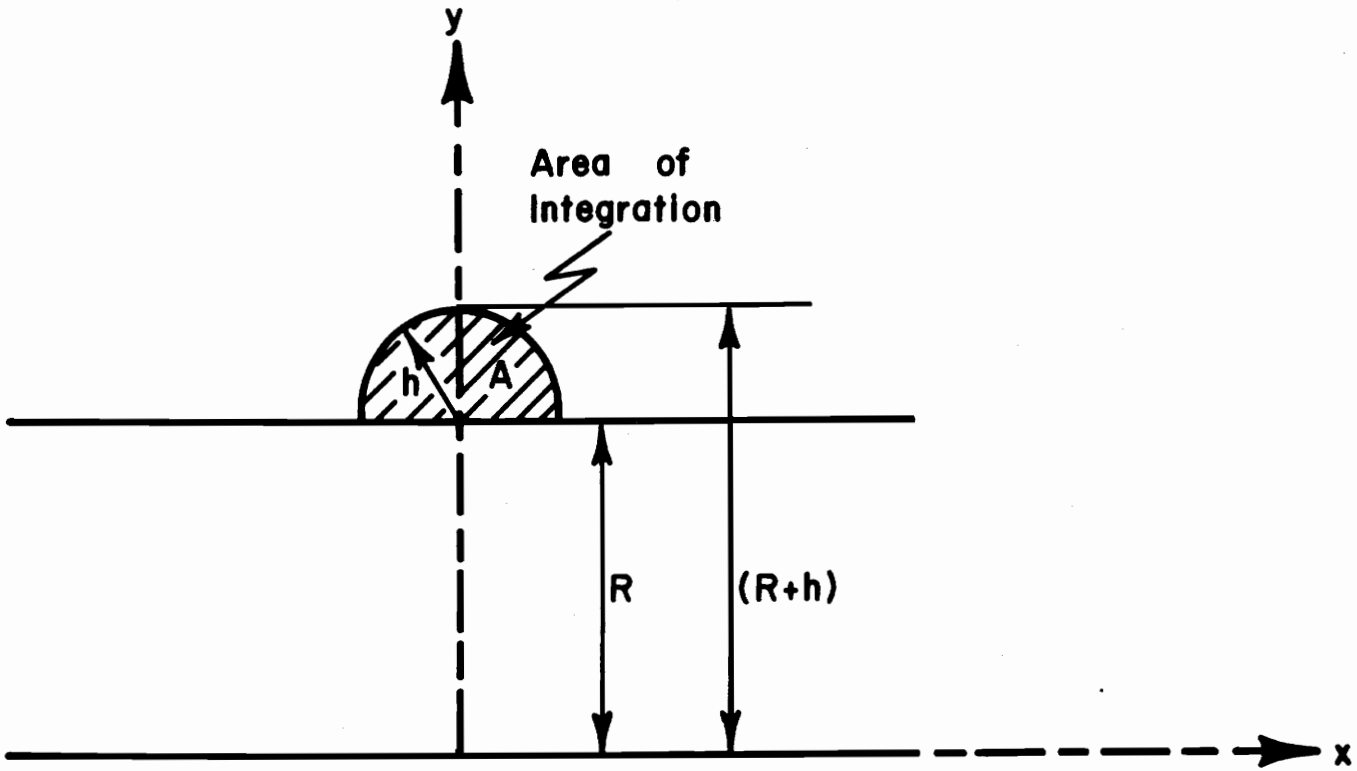

Figure 40. Coordinate System for Loop Probe Corrections

$$F = 2h\left[\frac{\pi}{4}\left(\frac{h}{R}\right)\left(1 + \left(\frac{h}{2R}\right)^2\right) = \frac{1}{3}\left(\frac{h}{R}\right)^2 - \frac{2}{15}\left(\frac{h}{R}\right)^4 + \ldots\right] \quad (156)$$

Taking the ratio of F(R=b) to R(R=a) and using a probe radius h = .0625 in. the correction factor is found to be, $R_I = 0.446$.

c. Measured Data

The current and charge distributions for two stepped-radius monopoles have been measured. The measurements were conducted at a frequency of 300MHz, and the electrical radii at this frequency are $kb_1 = 0.05$ and $ka = 0.02$. Fig. 41 gives the data for $h_1 = \lambda/4$, $h_2 = \lambda/4$. Fig. 42 gives the data for $h_1 = \lambda/4$, $h_2 = \lambda/2$. These two cases were choosen to illustrate the behavior for charge minimum and charge maximum at the position of the step. Some irregularities in the data, particularly the charge distribution of Fig. 42 are related to equipment problems which had not been over come at the time of this report. The behavior of the charge data near the step shows the expected edge behavior of exterior and interior 90^o corners.

Probe errors are significant near the step where the fields depart from the simple behavior assumed in computing the probe response. The departure of the current distributions from a smooth curve near the step is believed to be entirely caused by probe error. It is difficult to determine at this time the degree to which the observed charge behavior near the step is influenced by probe error. The

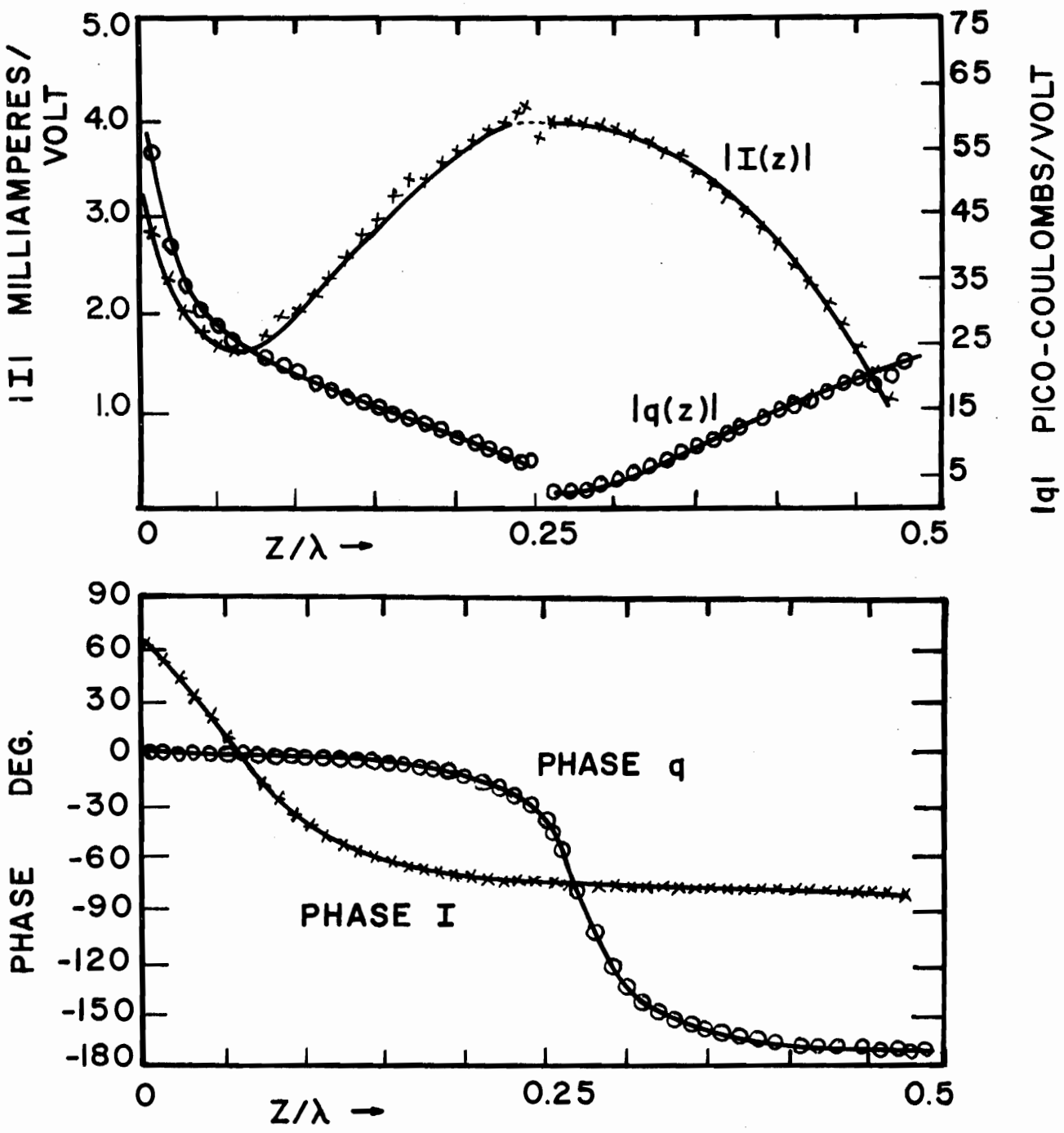

Figure 41. Stepped-Radius Antenna, $h_1=\lambda/4$, $h_2=\lambda/4$
Current and Charge

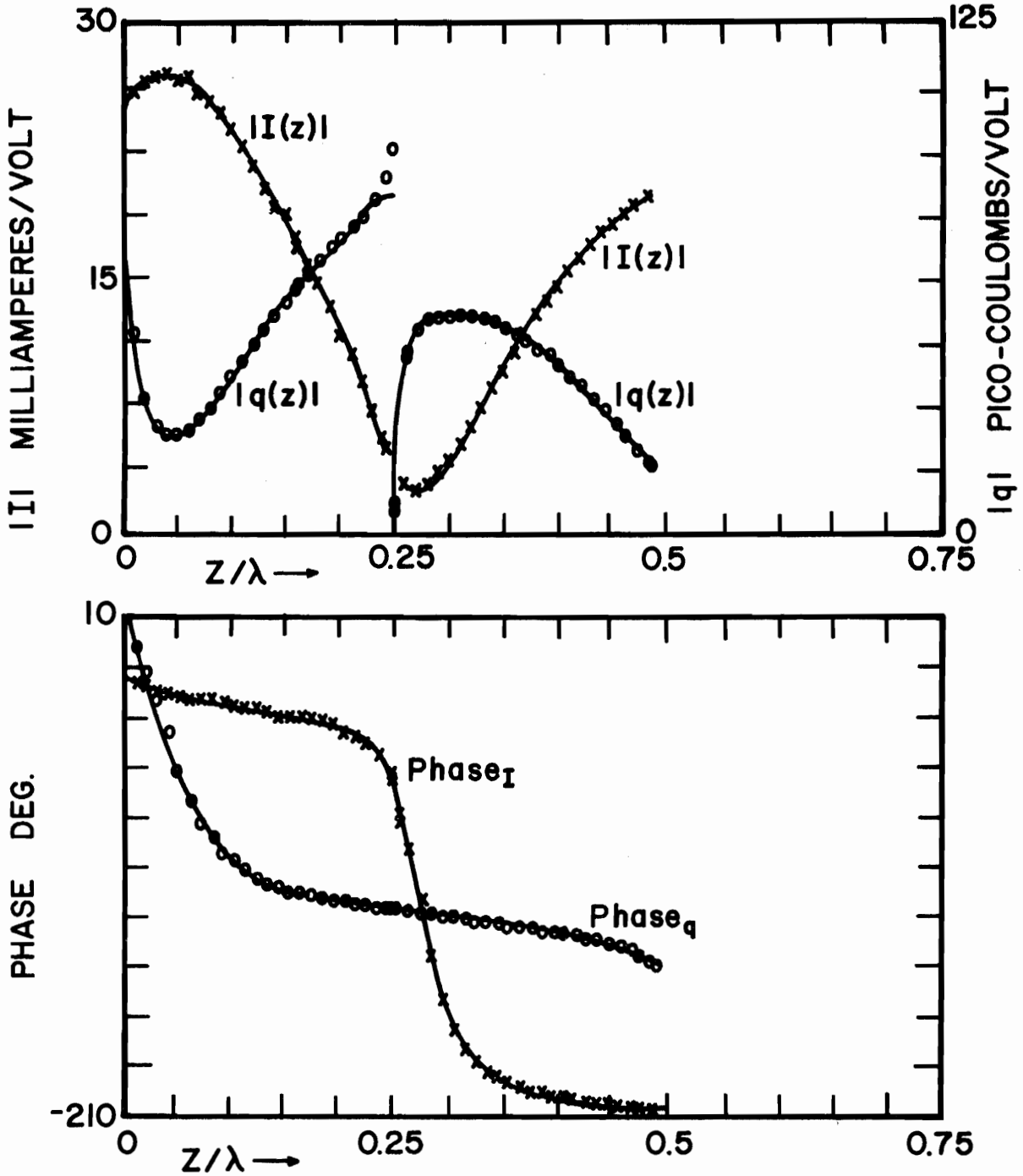

Figure 42. Stepped-Radius Antenna, $h_1=\lambda/4$, $h_2=\lambda/2$ Current and Charge

measured data demonstrates continuity of current across the step. However, until the probe errors can be determined no definite conclusion can be reached concerning continuity of charge per unit length at the step.

Figs. 43 and 44 show a comparison between the measured current and the numerical solution for the case $h_1 = h_2 = \lambda/4$. The agreement is seen to be very good except for a small difference which may be the result of errors in the probe calibration.

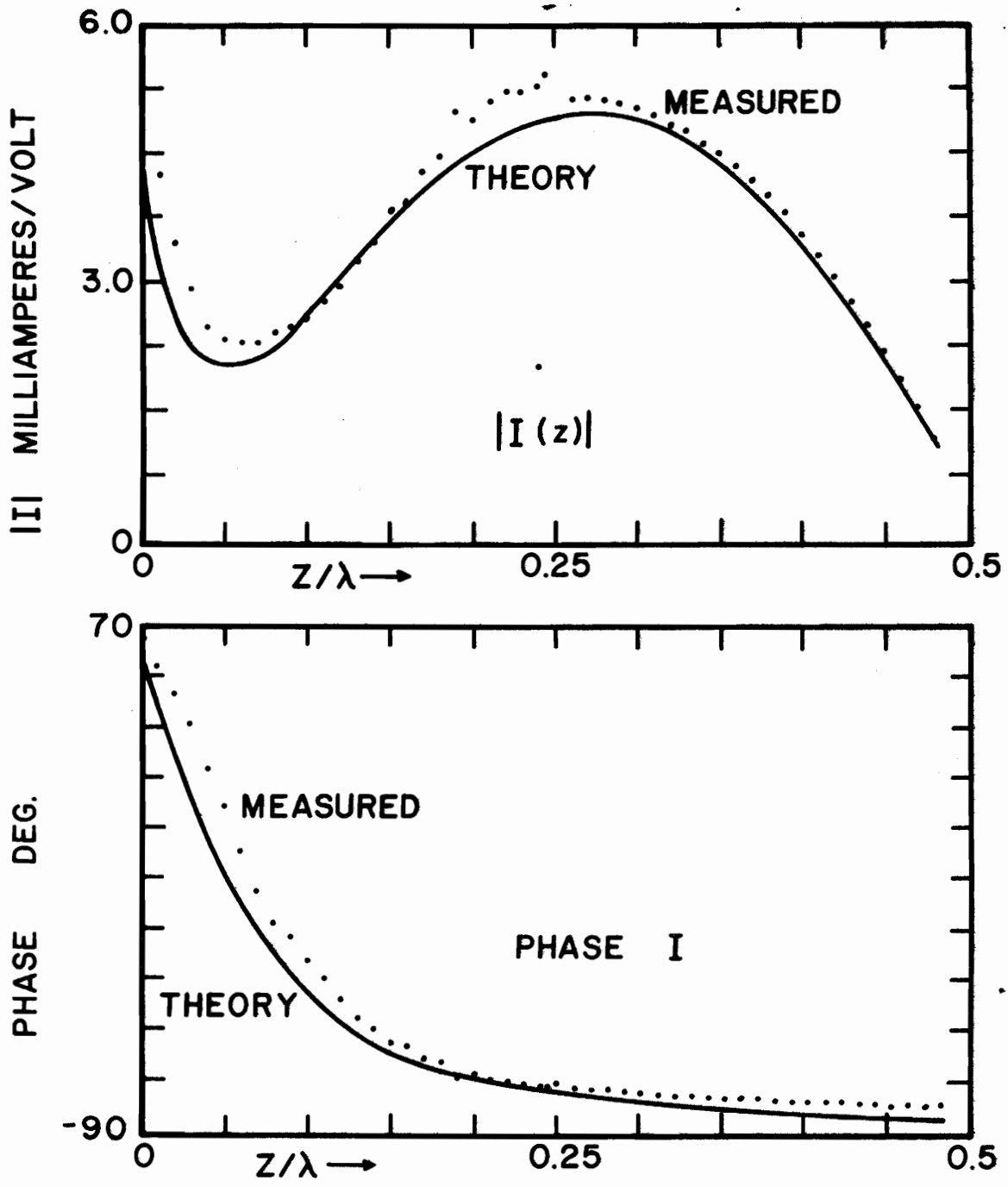

Figure 43. Stepped-Radius Antenna, $h_1=\lambda/4$, $h_2=\lambda/4$
$|I|$, Phase I Theory vs. Experiment

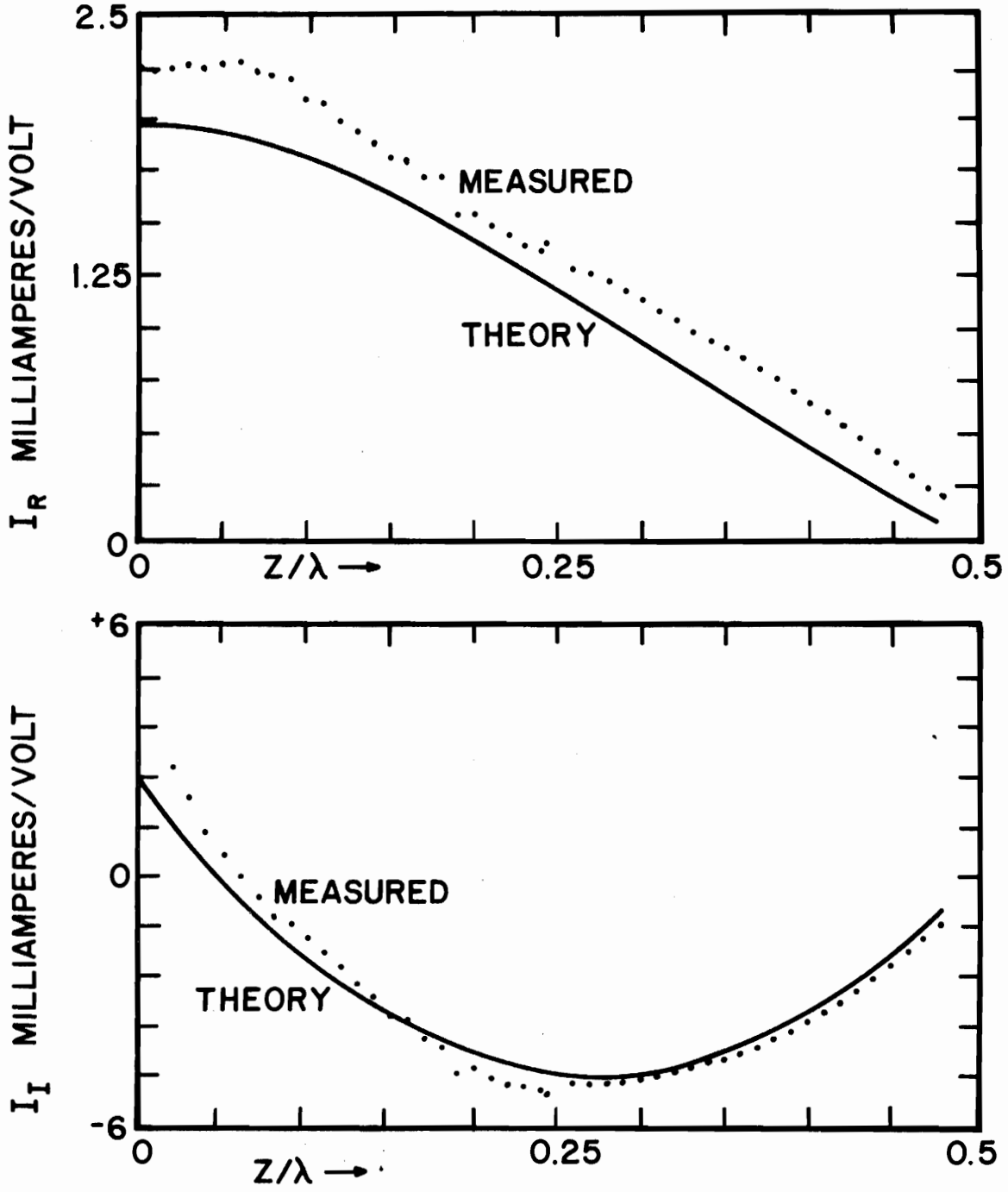

Figure 44. Stepped-Radius Antenna, $h_1=\lambda/4$, $h_2=\lambda/4$
I_R, I_I Theory vs. Experiment

SECTION VII

EXPERIMENTAL DATA-BENT WIRE AND V-CROSS

The experimental data obtained on the scattering elements described in Section V are presented in this Section. The principal use of these data is expected to be comparison with theoretical solutions. For this purpose the shape of the distribution curves is the most important information. No attempt has been made to obtain absolute normalization factors for the amplitude or phase of the measured data. It is, therefore, suggested that, in any future use of these data, normalization can be made at any appropriate point on the curves.

The geometries and coordinate systems used for presentation of the data are those shown in Fig. 26 and Fig. 45. The actual structures upon which measurements were made are shown in Fig. 36.

The measured current and charge distributions for bent wire scatterers are given in Figs. 46, 47, 48, 49. The current distributions for the case $h_1 = h_2 = \lambda/2$ were measured using a frequency of 600MHz, at which the electrical radius, is ka = 0.04. These results are shown in Fig. 46, and it is seen that the current on the $\theta = 30^{\circ}$ case is very similar to the $\theta=0$, i.e. straight wire, case. The principal difference

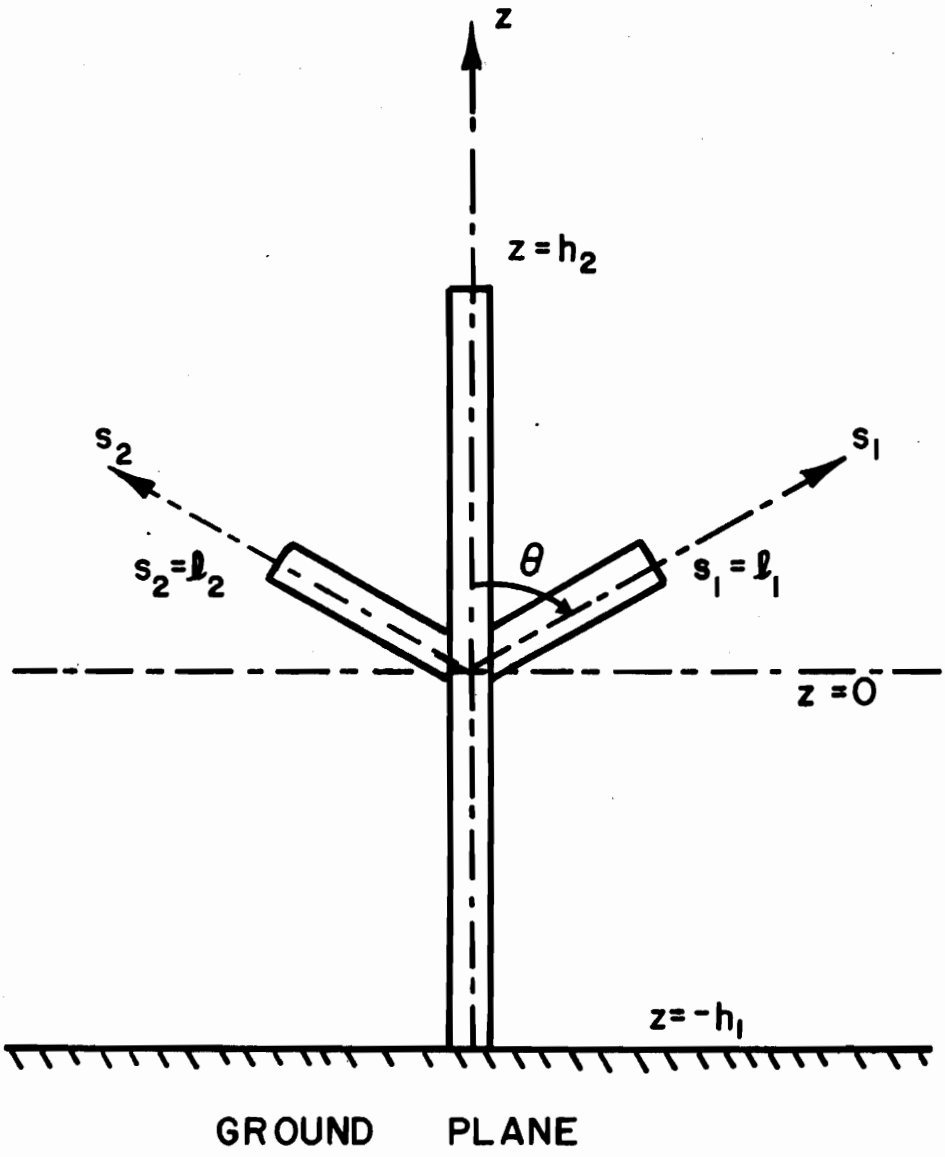

Figure 45. Coordinate System for V Cross Scatterer

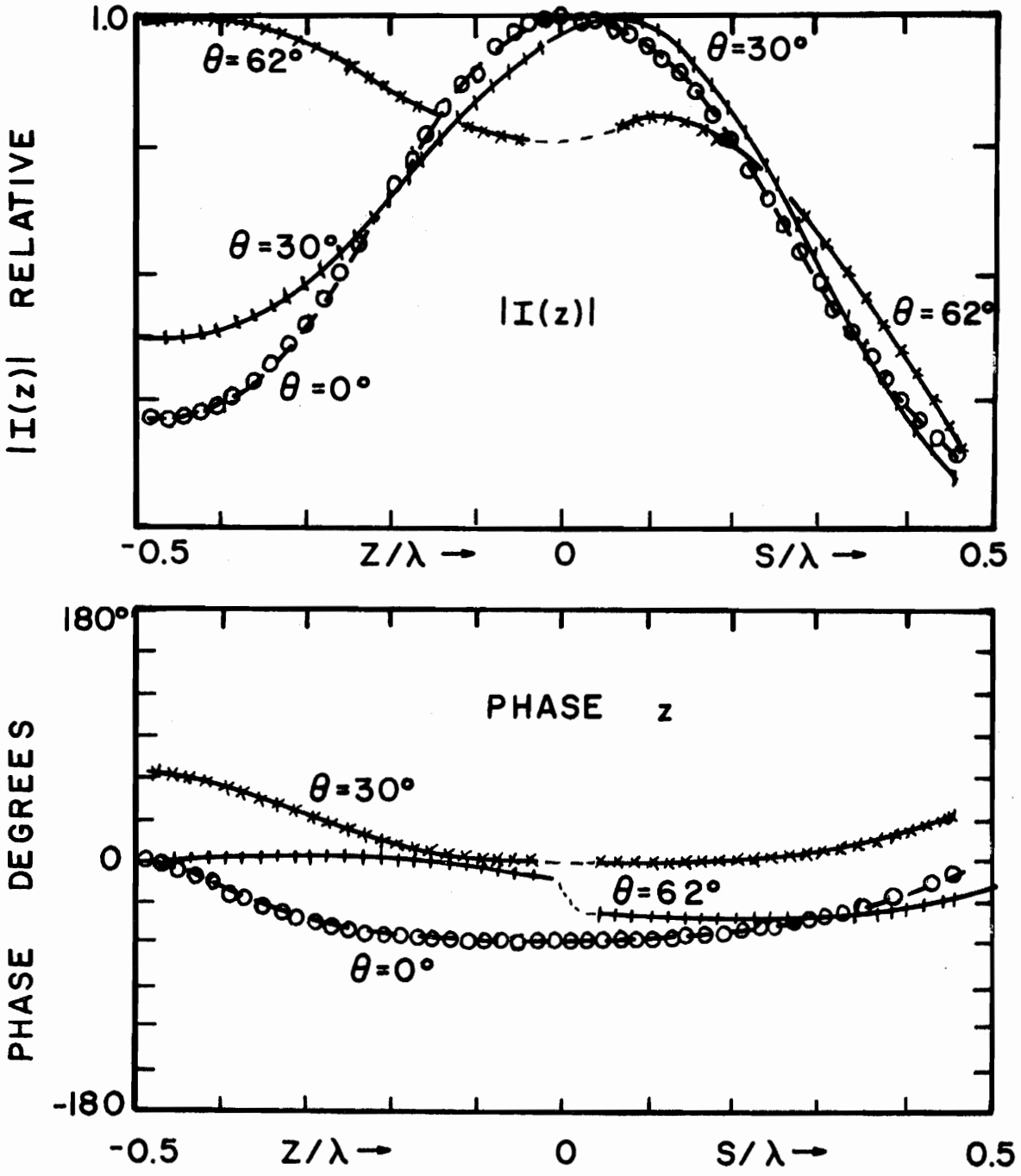

Figure 46. Bent Wire Scatterer Current, $h_1=h_2=\lambda/2$, ka=0.04

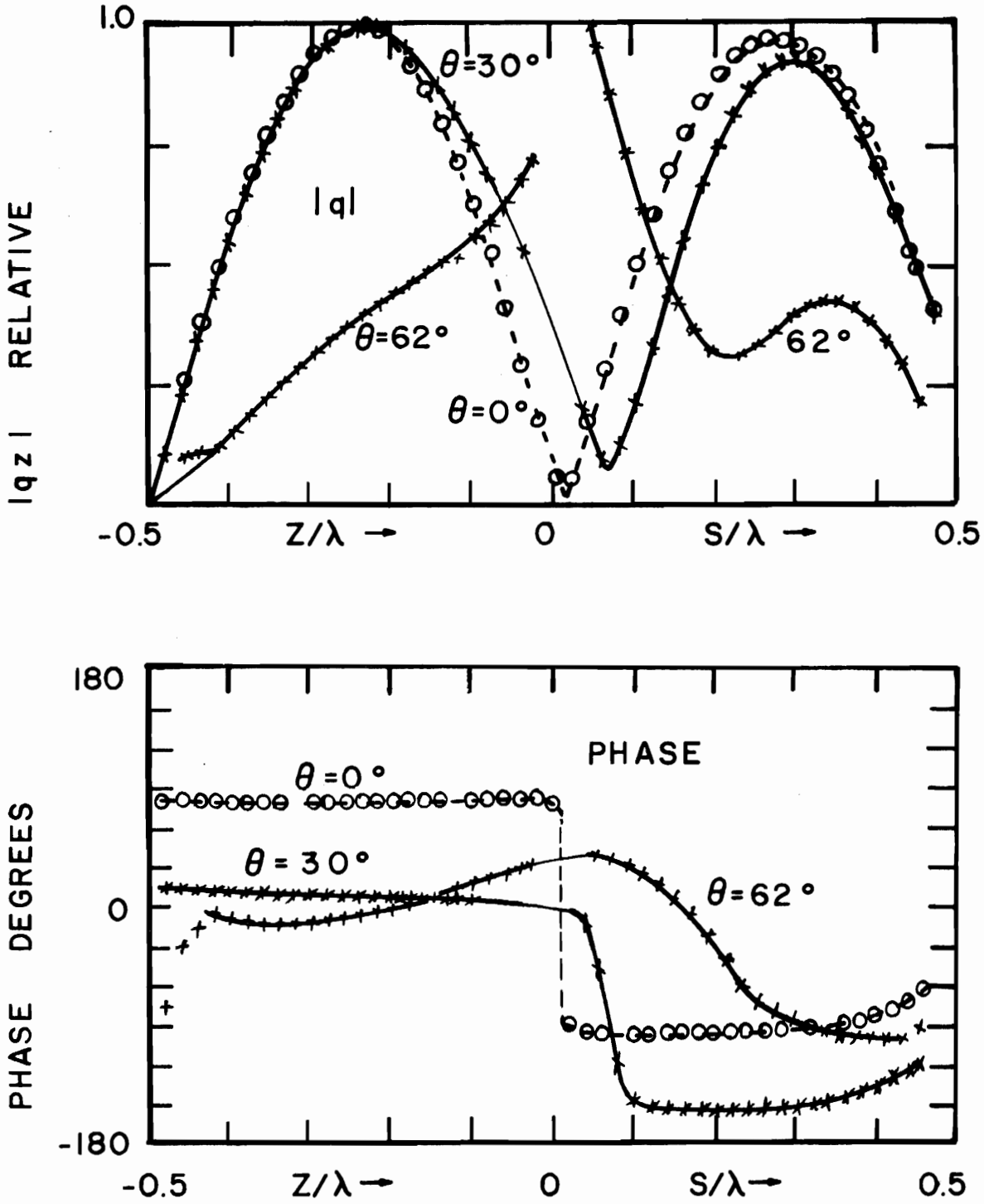

Figure 47. Bent Wire Scatterer Charge, $h_1 = h_2 = \lambda/2$, ka = 0.04

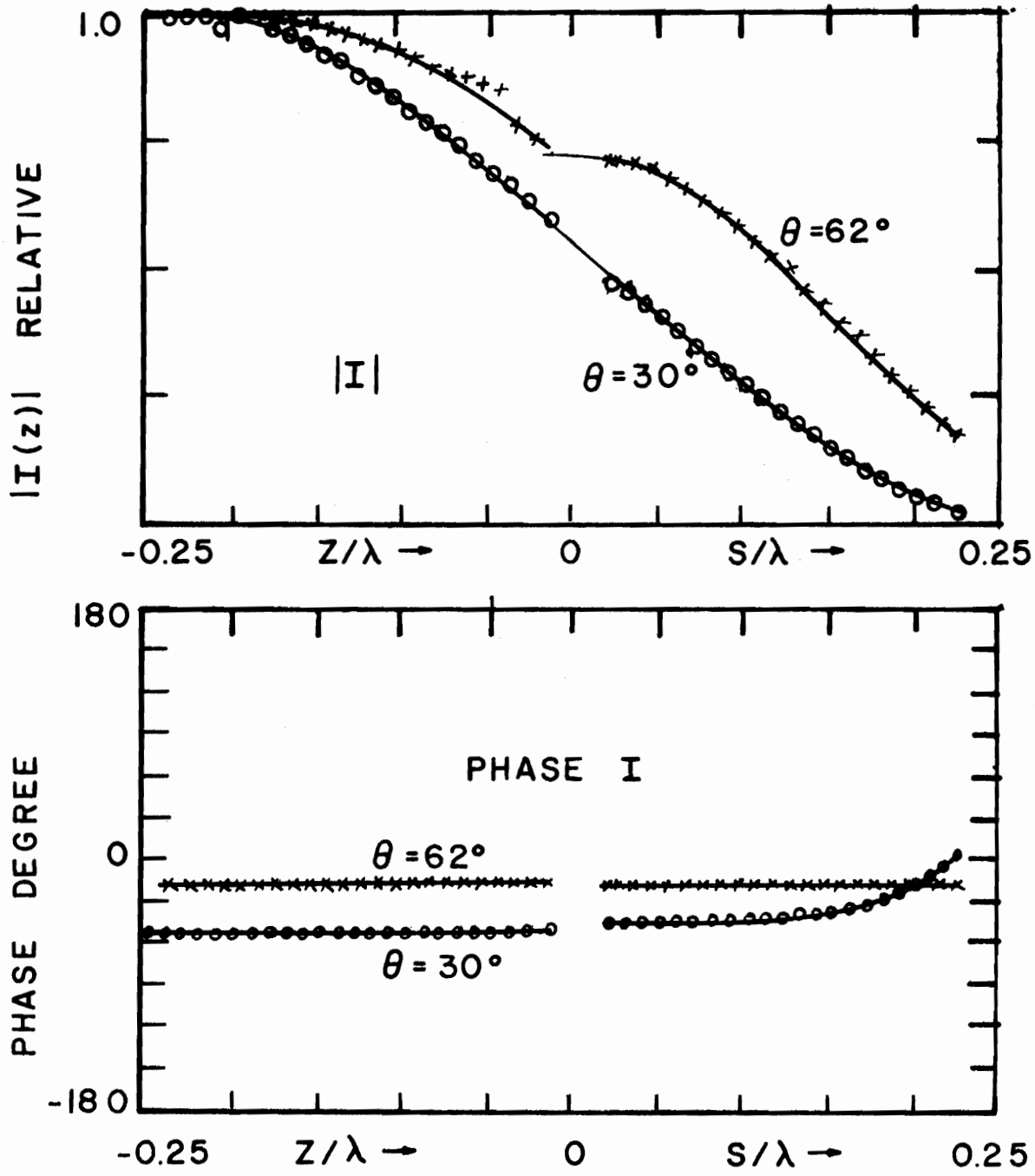

Figure 48. Bent Wire Scatterer Current, $h_1 = h_2 = \lambda/4$, ka = 0.02

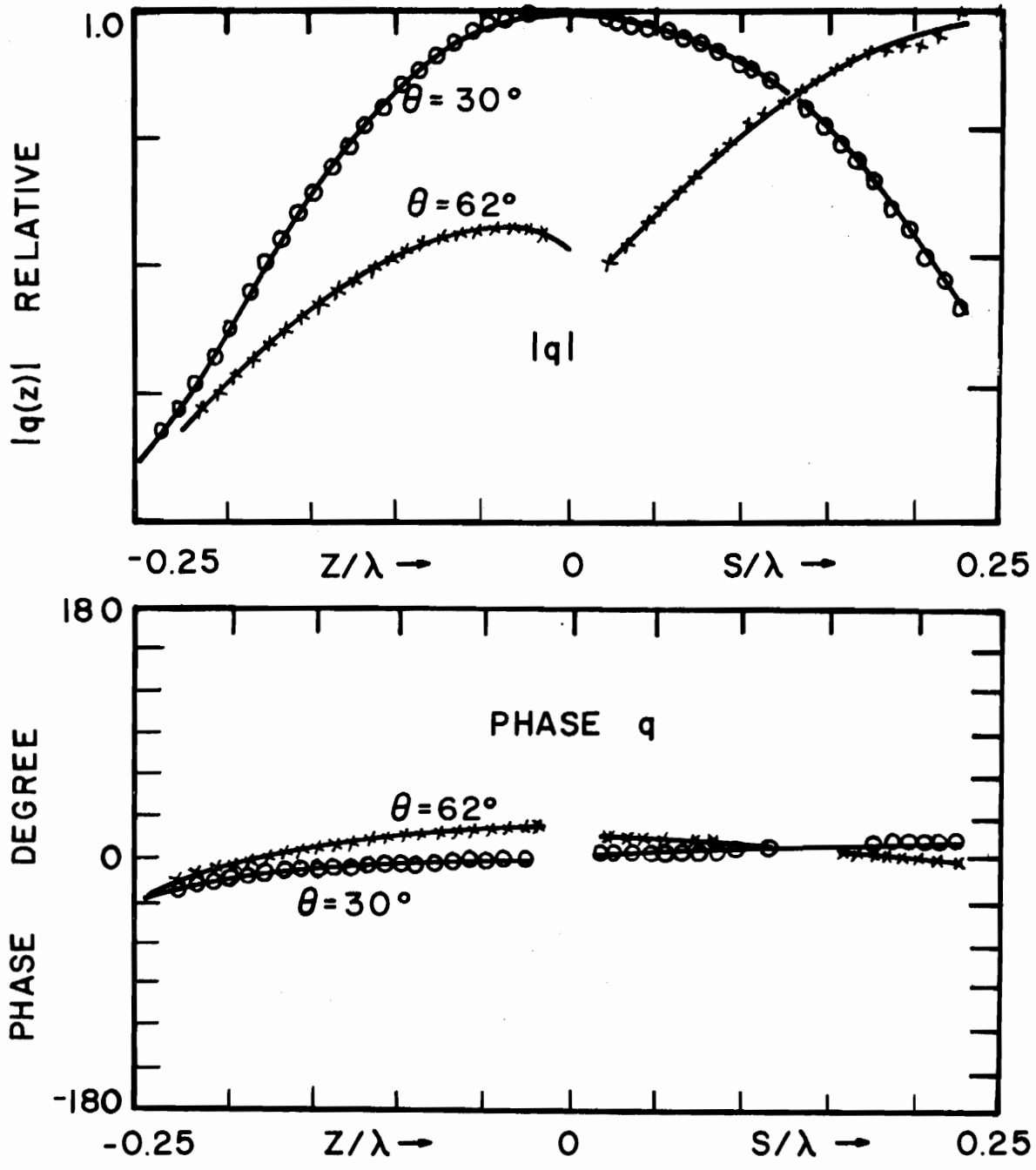

Figure 49. Bent Wire Scatterer Charge, $h_1 = h_2 = \lambda/4$, ka = 0.02

between these two distributions occurs near the image plane, together with a small shift in the position of the maximum. Increase of the bend angle to $\theta = 62^{o}$ results in a very significant change in the distribution of current on the z = 0 to $-h_1$, portion. It is somewhat surprising that the current distribution on the z=0 to $+ h_2$ portion retains essentially the same shape as for the $\theta = 0^{o}$ and 30^{o} cases. A comparison with Figs. 29 and 30 shows very good agreement with the predictions of the zeroth order solution as well as the numerically solutions given in Fig. 31. The curves shown across the junction region in Fig. 46 are of course only estimates of the behavior in this region. In addition to the mechanical problem of moving the probes into the junction region, measurement errors become significant near the junction where the fields are not slowly varying over the dimensions of the probe. These errors are evident in the $\theta = 62^{o}$ data of Fig. 46 where the two data points nearest the junction have been excluded from the estimated curve.

The charge distributions given in Fig. 47 show many of the same features as discussed above for the current. The $\theta = 0^{o}$ and $\theta = 30^{o}$ distributions are seen to be very similar with only a shift in the position of the minimum. The $\theta = 62^{o}$ data, however, shows even greater differences from $\theta = 0^{o}$, than were evident in the current distribution. In fact the entire nature of the charge distribution is changed, with the minimum which occurs at the junction for $\theta = 0^{o}$ and 30^{o} being replaced by a maximum.

Figs. 48 and 47 give the measured current and charge distributions for bent wires with $h_1 = h_2 = \lambda/4$. These measurements were made at a frequency of 300MHz and an electrical radius of ka = 0.02. Although not shown here it may be seen that the distributions for $\theta = 30^{\circ}$ are very similar to the known distributions for a straight wire, $\theta = 0^{\circ}$. As for the longer element the $\theta = 62^{\circ}$ distributions for this case show significant changes, particularly in the charge, a contrast between the $h = \lambda/2$ and $h = \lambda/4$ charge distributions for $\theta = 62^{\circ}$ is partiuclarly evident in the charge minimum which occurs at the bend for $h = \lambda/4$ whereas the $h = \lambda/2$ case shows a maximum of charge.

All of the bent wire structures discussed above were constructed with a sharp mitered junction. A different junction geometry was obtained by placing a brass sphere of 1 in. diameter around the junction. It must be pointed out that this is a rather large sphere and does not satisfy the conditions of thin wire theory at the frequencies used. The data are shown in Figs. 50 and 51 for distributions of current and charge with and without the sphere. Examination of these data shows that for the case of charge minor changes in the distributions occur. However, for the case which has a charge maximum at the junction very significant changes occur when the sphere is placed over the junction. For junction regions having an electrical size ka = 0.16, the geometry of the junction region is therefore of considerable importance. Further in-

vestigation will be necessary before conclusions can be reached concerning junctions of small electrical size.

The V cross structure is perhaps the most important in relation to theoretical studies of aircraft. The experimental data which has been obtained for current and charge distributions on this structure is given in Figs. 52, 53, 54, and 55. These measurements were made over an image plane as described in Section V. The two cases studied were intended to be examples of the behavior when a charge minimum occured at the junction, and when a charge maximum occured at the junction. As seen in Fig. 53 the $h_1 = h_2 = \lambda/2$, $\ell_1 = \ell_2 = \lambda/4$ case achieved a very deep charge minimum at the junction. However, as seen in Fig. 55 the $h_2 = \lambda/2$, $h_1 = 3\lambda/4$ case, while having a significant charge density at the junction, did not produce a real maximum desired. The two cases, however, do provide examples which show significantly different behavior.

Probe response errors exist near the junction, but do not appear to be significant factors in the measured data. A much more significant error is believed to be caused by the failure to achieve a planar wave front illumination. It is not possible at this time to evaluate the amount of error caused by the unknown incident field; however, the shape of the distribution on each arm is believed to be accurately represented in the measured data. Some changes may be expected in the relative magnitudes of these currents with changes in the incident field. Additional studies of these structures will be necessary before definite conclusions can be reached.

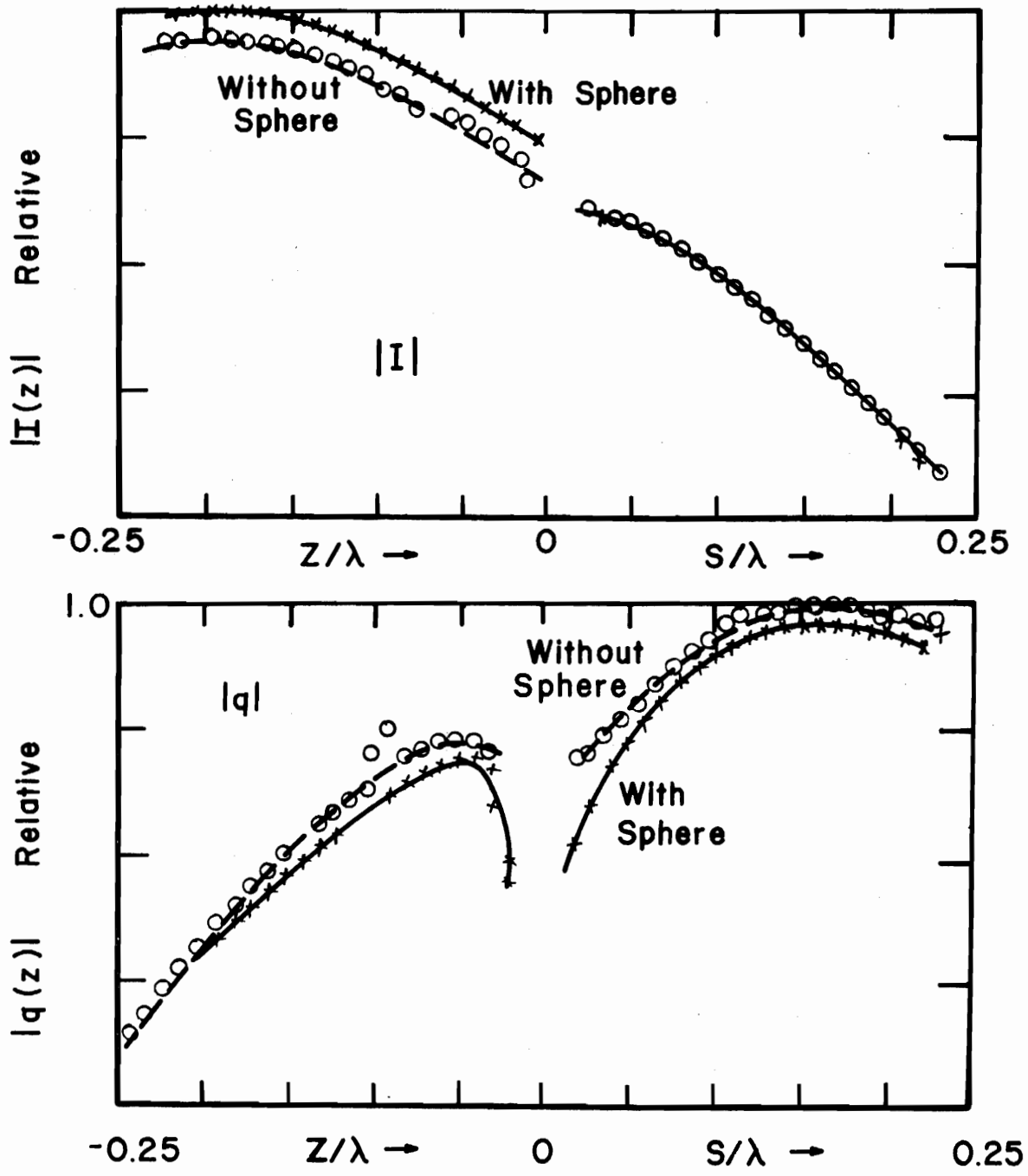

Figure 50. Bent Wire Scatterer Current and Charge $h_1 = h_2 = \lambda/4$, ka = 0.02, with and without Sphere at Junction

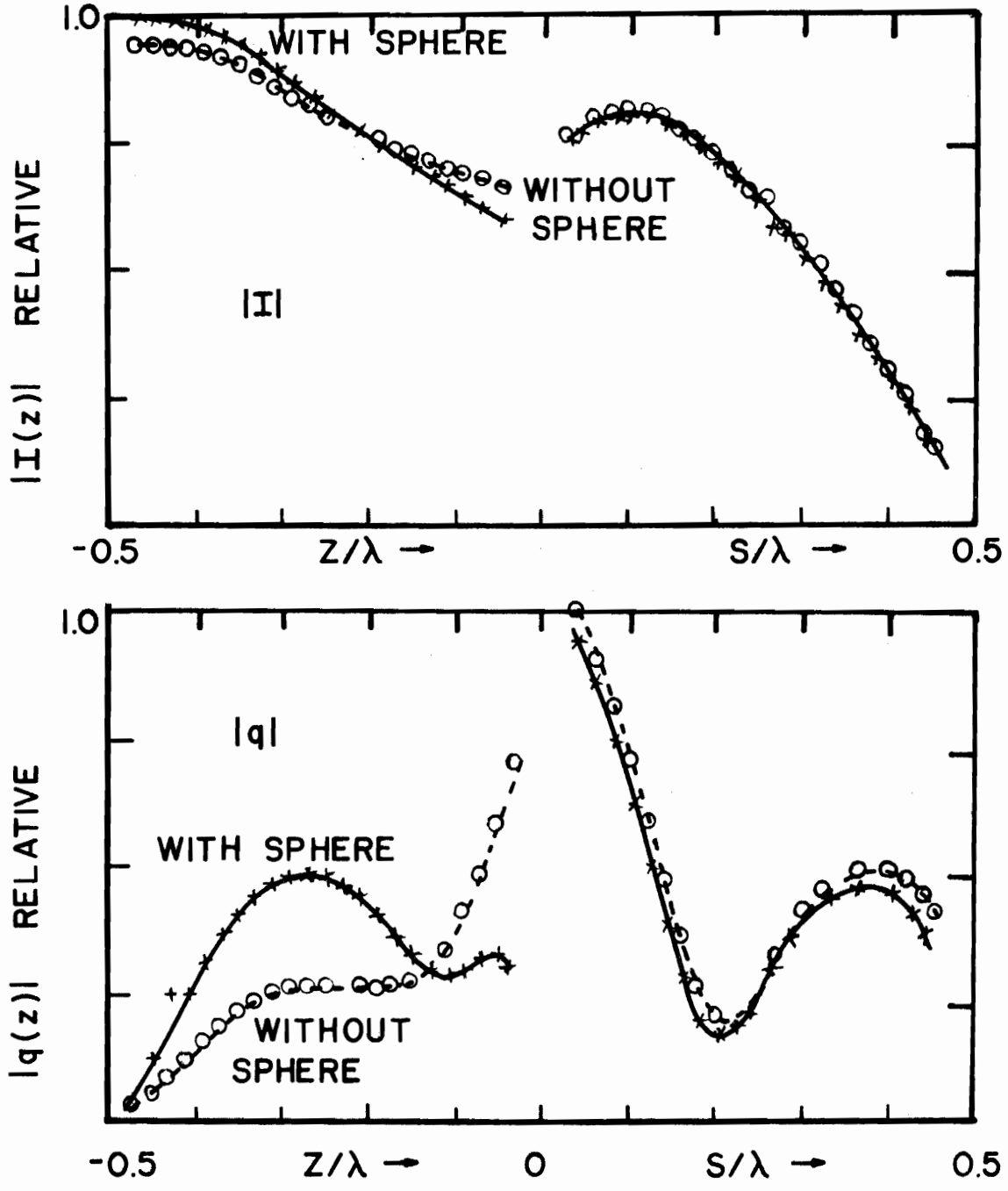

Figure 51. Bent Wire Scatterer Current and Charge $h_1 = h_2 = \lambda/2$, ka = 0.04 with and without Sphere at Junction

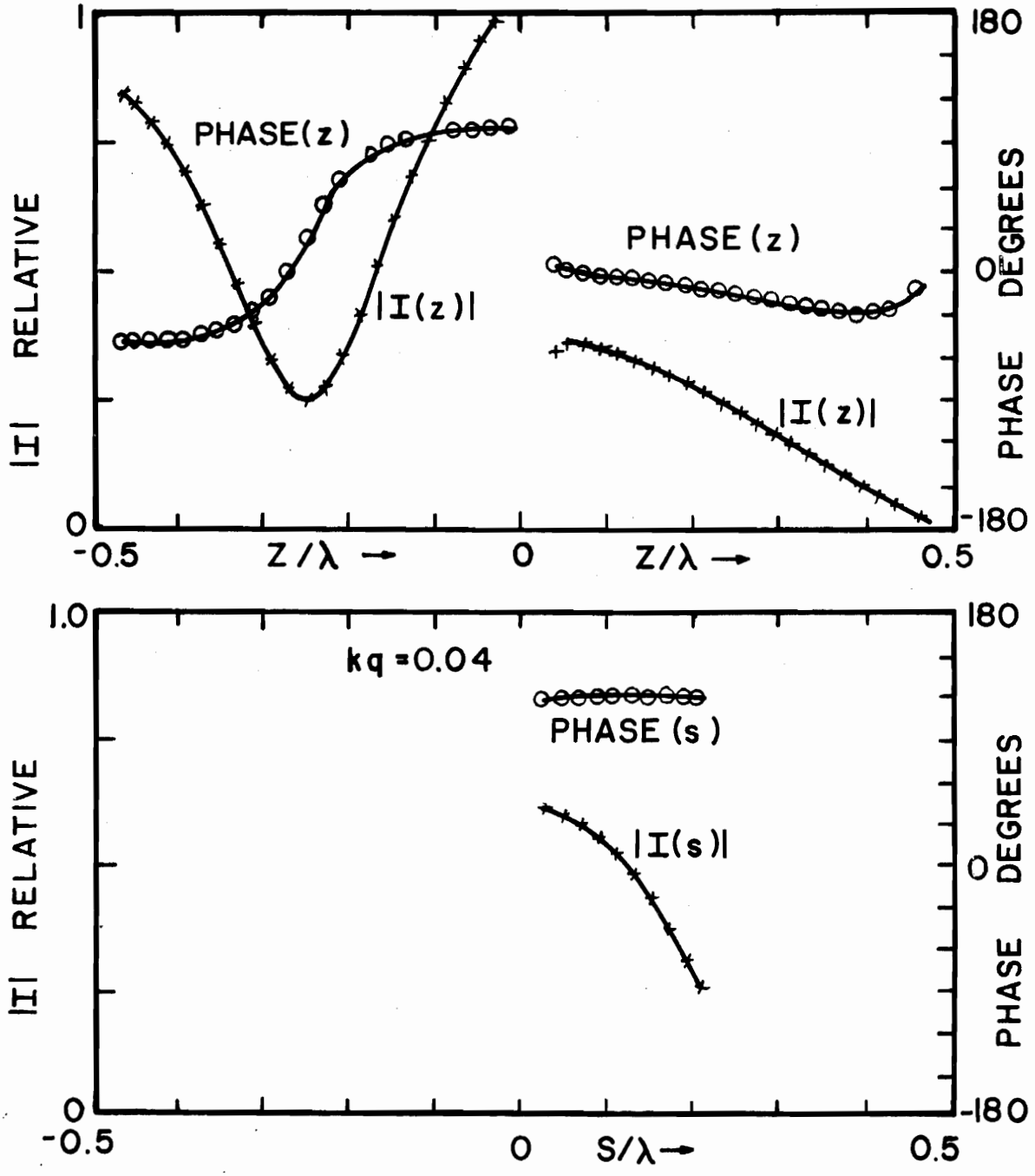

Figure 52. V Cross Current, $h_1 = h_2 = \lambda/2$, $\ell_1 = \ell_2 = \lambda/4$
$\theta = 60^\circ$

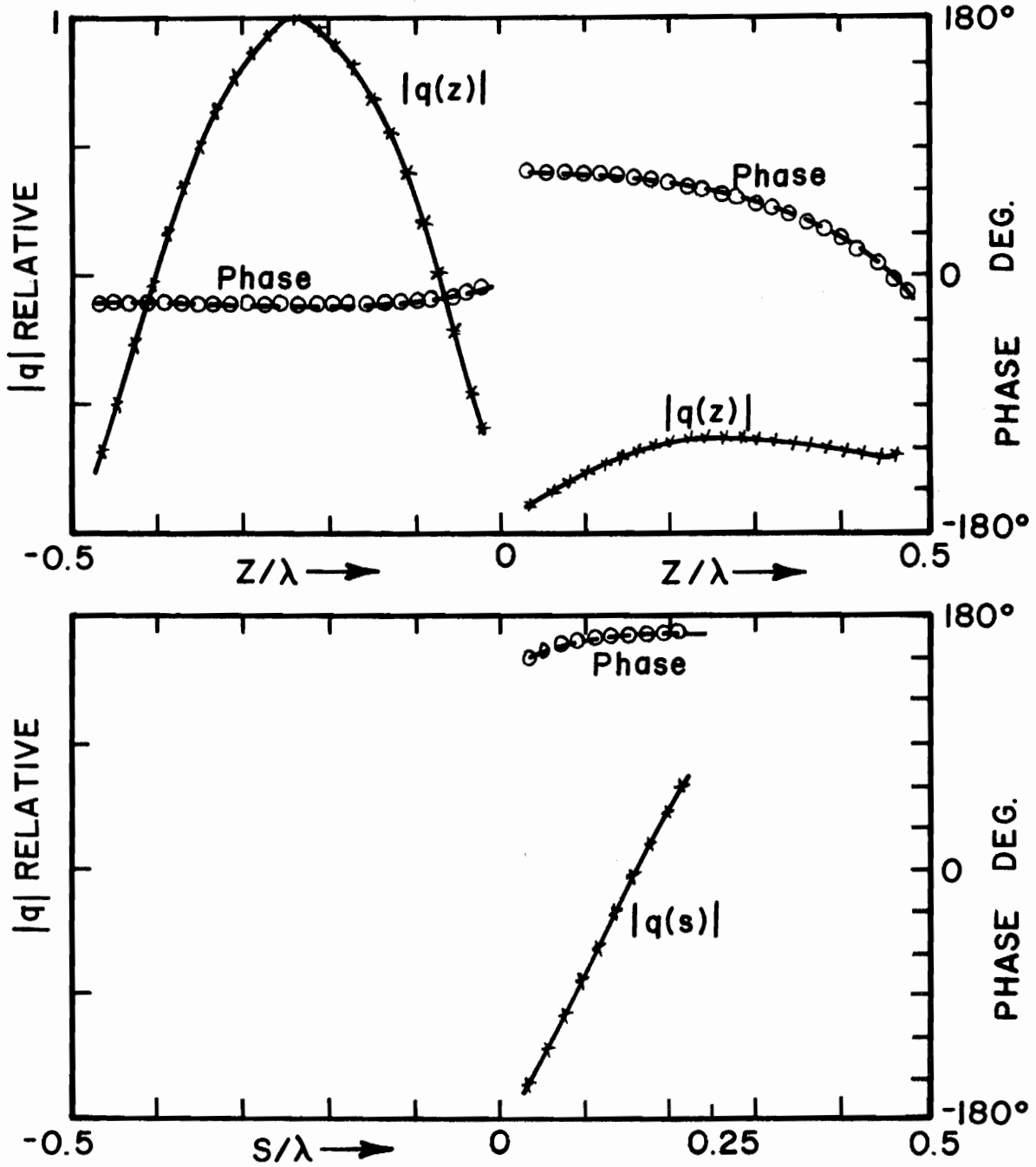

Figure 53. V Cross Charge $h_1 = h_2 = \lambda/2$, $\ell_1 = \ell_2 = \lambda/4$
$\theta = 60^\circ$

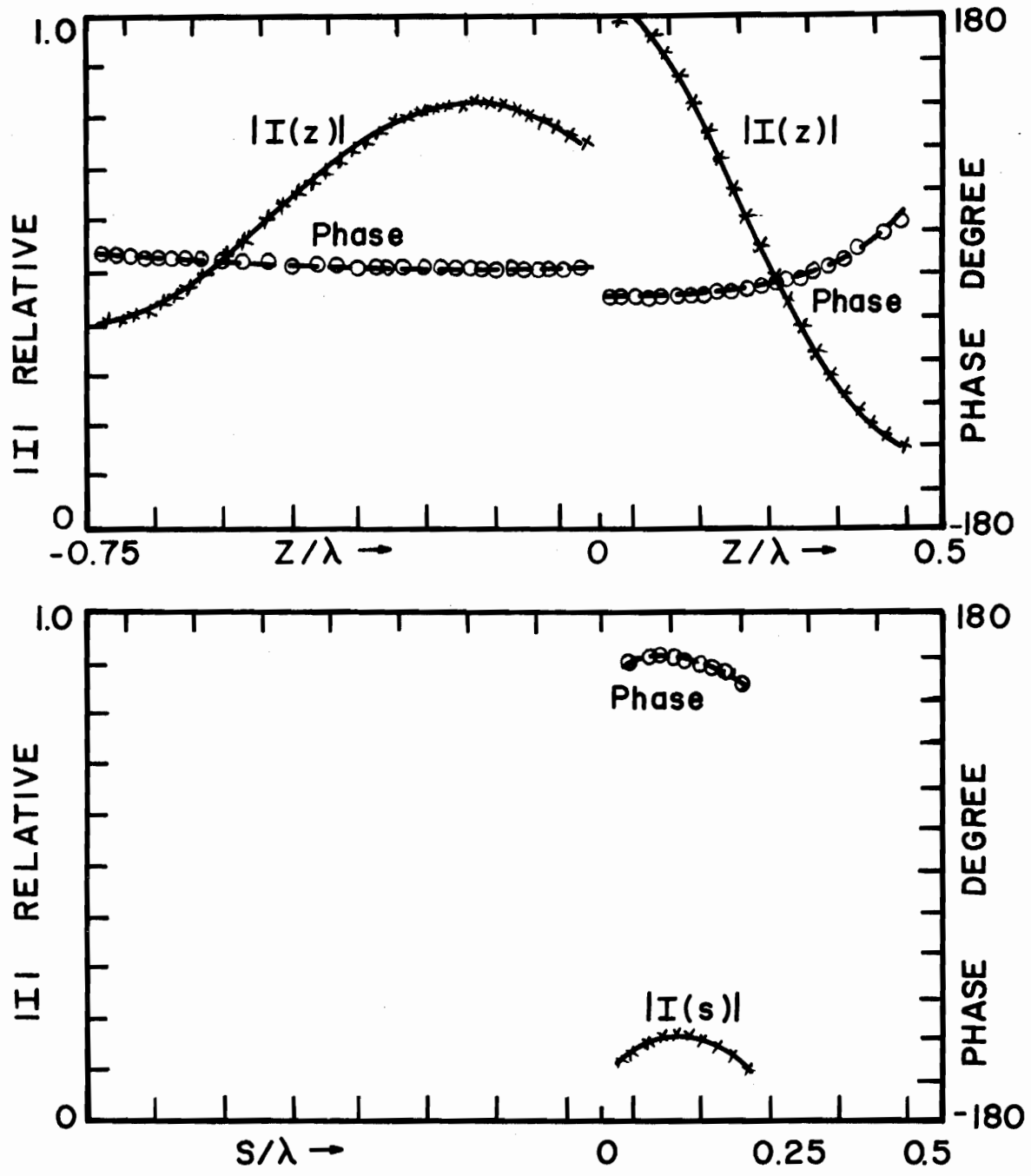

Figure 54. V Cross Current, $h_1 = 3\lambda/4$, $h_2 = \lambda/2$
$\ell_1 = \ell_2 = \lambda/4$, $\theta = 60^o$

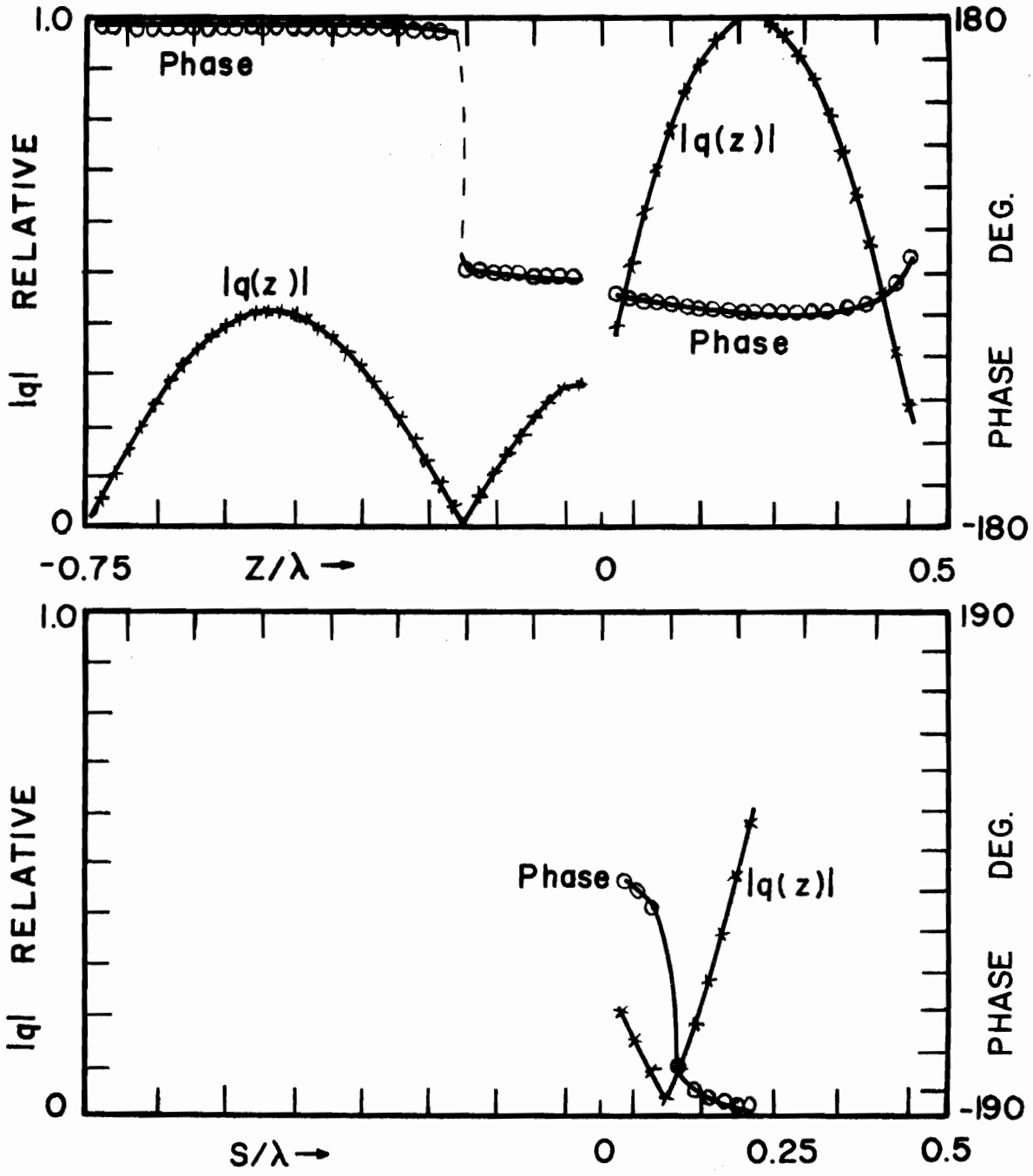

Figure 55. V Cross Charge, $h_1 = 3\lambda/4$, $h_2 = \lambda/2$
$\ell_1 = \ell_2 = \lambda/4$, $\theta = 60^{\circ}$

SECTION VIII

CONCLUSIONS

Results of the theoretical and experimental investigations are presented for current and charge distributions on thin-wire scatterers. Insofar as the investigators are aware, these are the first experimental data available for the structures studied in this project. The study of wire junctions is far from complete but this initial work, both theory and experiment, certainly addresses the major question of what the appropriate thin-wire junction conditions should be. The experimental investigation of structures with junctions is in its infancy and numerous facets deserve further refinement, yet, within limitations of accuracy and experimental error, the correlation between measured and theoretically predicted results is both gratifying and encouraging.

A careful study of the incident fields which illuminate the test scatterers will be necessary before a higher confidence level can be attributed to the measured data and before accurate quantitative differences between results of theory and experiment can be concretely established. Additional experimental work is needed to define the limits of thin-wire theory for structures having junctions.

Measurements on the monopole with a radius discontinuity, the most fundamental thin-wire junction, are of particular interest presently but, unfortunately, are not entirely conclusive. A set of boundary conditions, firmly founded on theory, are developed in this report for the stepped-radius wire, but the investigators do not judge the accuracy of their data to be sufficient to enable them to claim undeniable corroboration of the small discontinuity predicted in linear charge density.

The data collected and the experience gained by the investigators in refining their experimental techniques indicate that further data analysis would yield more conclusive results but that additional measurements are needed to complete the junction picture.

REFERENCES

1. E. K. Miller, R. M. Bevensee, A. J. Poggio, L. Adams, F. J. Deadrick and J. A. Landt, "An Evaluation of Computer Programs Using Integral Equations for the Electromagnetic Analysis of Thin Wire Structures," AFWL EMP Interaction Notes, Note 177, p. 104, March, 1974.

2. F. M. Tesche, "Numerical Considerations for the Calculation of Currents Induced on Intersecting Wires Using the Pocklington Integro-Differential Equation," AFWL EMP Interaction Notes, Note 150, p. 27, Eq. 27, January, 1974.

3. C. D. Taylor, "Electromagnetic Scattering from Arbitrary Configurations of Wires," Trans. IEEE, Vol. AP-17, pp. 662-663, September, 1969.

4. C. D. Taylor, S. M. Lin and H. V. McAdams, "Scattering from Crossed Wires," Trans. IEEE, Vol. AP-18, pp. 133-136, January, 1970.

5. C. M. Butler, "Currents Induced in a Pair of Skew-Crossed Wires," Trans. IEEE, Vol. AP-20, pp. 731-736, November, 1972.

6. H. H. Chao and B. J. Strait, "Radiation and Scattering by a Configuration of Bent Wires with Junctions," Trans. IEEE, Vol. AP-19, pp. 701-702, September, 1971.

7. J. C. Logan, A Comparison of Techniques for Treating Radiation and Scattering by Wire Configurations with Junctions, Technical Report TR-73-10, Department of Electrical and Computer Engineering, Syracuse University, Syracuse, New York, August, 1973.

8. R. W. P. King and T. T. Wu, "Analysis of Crossed Wires in a Plane-Wave Field," Interaction Note 216, July 1974.

9. R. W. Burton and R. W. P. King, Induced Currents on Single and Crossed Wires, presented at URSI-IEEE annual meeting, University of Colorado, Boulder, Colorado, October, 1974.

10. N. Marcuvitz, Waveguide Handbook, pp. 310-311, McGraw-Hill Book Co., New York, 1951.

11. R. W. P. King, Theory of Linear Antennas, p. 534, Harvard University Press, Cambridge, Massachusetts, 1956.

12. R. M. Ryder, "The Electrical Oscillations of a Perfectly Conducting Prolate Spheriod," Journal of Applied Physics, Vol. 13, pp. 327-343, May, 1942.

13. R. F. Harrington, Field Computation by Moment Methods, Macmillan, New York, 1968.

14. R. W. P. King and T. T. Wu, "Analysis of Crossed Wires in a Plane-Wave Field," presented at 1974 URSI Annual Meeting, Boulder, Colorado, October, 1974.

15. C. M. Butler, K. R. Umashankar, and C. E. Smith, Theoretical Analysis of the Wire Biconical Antenna, report submitted to U. S. Army STRATCOM, January, 1975.

16. R. B. Mack, A Study of Circular Arrays, Cruft Laboratory Report No. 384, Harvard University, Cambridge, Massachusetts, 1963.

17. H. Whiteside, Electromagnetic Field Probes, Cruft Laboratory Technical Report No. 377, Harvard University, Cambridge, Massachusetts, 1962.

18. R. W. Burton and R. W. P. King, Private Communication.